THREE-DIMENSIONAL COMPUTATIONAL MODELING OF PSEDUOPOD-DRIVEN AMOEBOID CELLS THROUGH EXTRACELLULAR MATRIX GEOMETRY

By

ERIC J. CAMPBELL

A dissertation submitted to the

School of Graduate Studies

Rutgers, The State University of New Jersey

In partial fulfillment of the requirements

For the degree of

Doctor of Philosophy

Graduate Program in Mechanical and Aerospace Engineering

Written under the direction of

Prosenjit Bagchi

And approved by

_____

_____

_____

_____

New Brunswick, New Jersey

May, 2019

ABSTRACT OF THE DISSERTATION

Three-Dimensional Computational Modeling of Pseudopod-

Driven Amoeboid Cells

Through Extracellular Matrix Geometry

By ERIC J. CAMPBELL

Dissertation Director:

Prosenjit Bagchi

Migration of amoeboid cells is characterized by the formation of pseudopods, or extensions of the cell membrane which protrude outwards, bifurcate, and retract in a dynamic fashion. The study of the amoeboid morphology is immeasurably important, as many cells and processes within the body depend on pseudopod-based migration, such as the phagocytosing of foreign pathogens by immune cells, the extension of nerve axons during neural development, the repair of damaged connective tissue and skin by fibroblasts and epithelial cells, the migration of key progenitor cells during embryonic development, and the invasive propensity of cancer cells during metastasis. Amoeboid motility is a complex, multiscale process which involves extreme cell deformation, internalized and surface-bound biochemistry, and both cytoplasmic and extracellular fluid interactions. Additionally, cells are often immersed within a confining and complex heterogenous

environment known as the Extracellular Matrix (ECM). The ECM and cell are fundamentally coupled to one another, where membrane deformability, surface protein diffusivity, fluid viscosity, matrix porosity, pore size, and alignment can alter the behavior and dynamics of a cell.

In this dissertation, a three-dimensional computational model is presented in which pseudopod-driven amoeboid migration is analyzed in various geometries, and under varying cell parameters. Models are developed for the cell membrane, pseudopod pattern generator, extracellular matrix geometry, and fluid-cell/fluid-obstacle coupling, after which a detailed analysis is performed. The approach is based on use of immersed-boundary methods, which allow for seamless integration between the highly deformable cell, fluid, and arbitrarily-shaped extracellular geometry. Amoeboid swimming is first studied through an unbounded fluid domain, revealing effects caused through the alteration of membrane deformability, surface-protein diffusivity, and fluid viscosity. A regime change in cell dynamics, allowing the cell to transition from slow, random motion, to fast, persistent motion is observed in certain parameter ranges. Cell migration through various ECM geometries is then considered, where the influence of matrix porosity and obstacle size is added to the existing analysis. In addition to drastically altered behavior, interesting cell dynamics are seen due to cell-obstacle interactions. Finally, amoeboid locomotion is studied through an expanded assortment of ECM geometries, while a weak adhesion model characteristic of an amoeboid cell is adopted. In each case, a comprehensive study of cell behavior, pseudopod dynamics, and fluid field analysis is performed. The simulated cell is shown to be qualitatively similar in form to experiments, and quantitatively similar in regard to cell speed and dynamics. Insights into cell persistence, dynamics, and migration

speed are given. Overall, this model pushes the forefront of the three-dimensional computational modeling of amoeboid cells, revealing fascinating behaviors, trends, and dynamics. Its continued refinement has the potential to reveal further mechanisms of amoeboid migration and the influence of tissue geometry on its behavior.

Acknowledgements

Chapters 3-4 are based on the following journal articles, in which all simulation and analysis was done by myself.

1. E. J. Campbell and P. Bagchi. A computational model of amoeboid cell swimming. *Physics of Fluids*, **29**:101902 (2017).
2. E. J. Campbell and P. Bagchi. A computational model of amoeboid cell motility in the presence of obstacles. *Soft Matter*, **14**:5741 (2018).

Chapter 5 is based on a research currently in progress, where we expect to publish in the next few months.

3. E. J. Campbell and P. Bagchi. *Physical Review E* (2019).

Dedication

To my parents.

Table of Contents

List of Tables

List of Illustrations

Chapter 1

Introduction

1.1 Introduction

Life, in all its forms and variations, can be abridged into one single fundamental element: the cell. Whether this cell is an independent single-celled organism, or a member of the greater multicellular-organism collective, the capability of cells to effectively migrate through their environment bears significant importance, be it for wound repair [24], disease [21] and infection fighting [22], neural development [47], or reproduction [23]. Within the field of cellular motility, a multitude of diverse migration tactics is on display, from the flagellar-based mode commonly sported by many bacteria [25], to the exotic contractile-driven blebbing mode seen in aggressive forms of cancer [20]. This work, however, will focus on "amoeboid" migration, a characterization given to highly deformable cells which rely on membrane extensions to migrate [26]. In the following subsections, key elements of cell locomotion which are required to understand the amoeboid migration morphology are discussed.

1.2 The cell

Eukaryotic cells are composed of a plasma membrane which separates a cell from its external environment. This membrane is constructed of a lipid bilayer as seen in Figure 1.1, also containing copious amounts of proteins which exchange ions and molecules with the external environment, sense chemical signals, and interact with the substrate [47]. Existing directly below the plasma membrane is the cell cortex, or a concentrated three-

dimensional network of actin filaments which determines cell shape and plays key roles in migration [45]. Inside the cell is the cytoplasm, a viscoelastic combination of a gel-like fluid known as the cytosol, organelles, and other compounds, such as nutrients and proteins. The last major component of the cell is the cytoskeleton, a composition of actin fibers, intermediate filaments, and microtubules which aid in cell adhesion and migration, resisting mechanical stress, and organelle transport [56]. For modeling purposes, the complexities of a cell can be simplified as a viscous drop enveloped by a zero-thickness membrane.
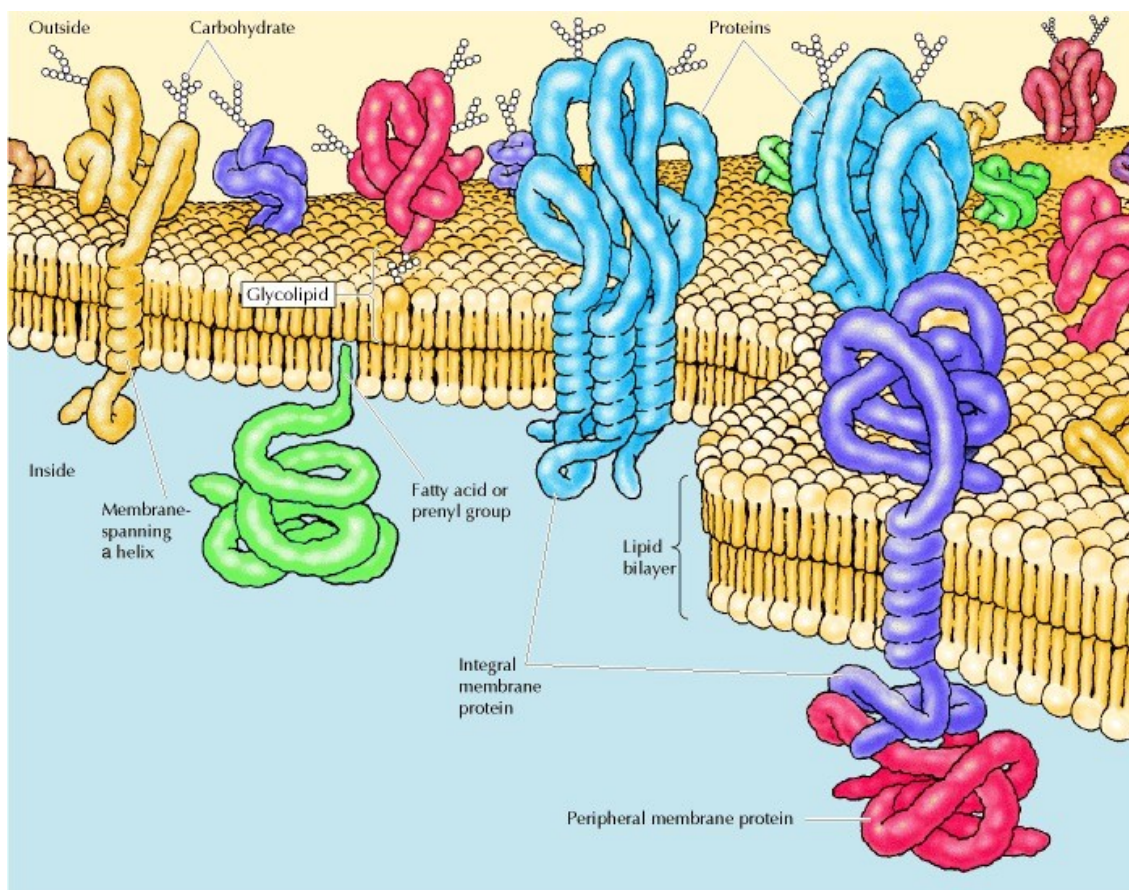
Figure 1.1: Fluid mosaic model of a cell's plasma membrane showing various proteins embedded in the lipid bilayer [45]. Image taken from Figure 2.48 of The Cell: A Molecular Approach by Geoffrey M. Cooper © 2000. Reproduced with permission of the Licensor through PLSclear.

1.3 The Extracellular Matrix (ECM)

Estimates of the average number of cells present within the human body are on the order of tens of trillions [38], with each cell given a predetermined biological role. The body is not simply composed of cells however. There also exists a porous and heterogenous structure (Figure 1.2) composed of macromolecules and other elements known as the Extracellular Matrix (ECM). The ECM acts like a scaffold, providing cells with a structure to adhere to and function on [39]. Additionally, the ECM is capable of influencing cell behavior through chemical signaling [37] or mechanical stimulation [36], effectively changing the way a cell behaves or expresses certain genes. These characteristics elucidate the very strong coupling between a cell and its environment, presenting a complex challenge to model. Of further interest are the ECM properties, and subsequent cell behaviors that arise based on scaffold geometry, and proportion and composition of ECM components. Bone, for instance, has a significantly different extracellular matrix compared to that of connective tissue [40]. In general, the ECM is composed of five major components which are discussed below [49]: collagen, elastin, proteoglycans, hyaluronan, and adhesive glycoproteins.

1.3.1   Collagen

Highly abundant within the human body, fibroblast-generated collagen is readily used as a structural component within the extracellular matrix. Rod-shaped molecules of type I collagen approximately three-hundred nanometers long aggregate to form fibrils [47]. Fibrils themselves can associate to form larger collagen fibers, which can reach several micrometers in diameter and length [45]. Combinations of the various isoforms and associations of collagen can produce very distinct tissues. Tendons, for instance, are almost

completely constructed of aligned bundles of densely-packed collagen, while bone is formed from layers of collagen fibrils implanted in calcium phosphate crystals for rigidity [47]. A tissue sample containing collagen fibers with varying orientations is shown in Figure 1.3. While fibrils and fibers are extremely common in the body, other variants of collagen, such as the type IV group, can produce dense sheets known as the basal lamina [49], which serves as a support structure for nerve and muscle cells in addition to epithelia. Collagen should be considered when modeling the ECM, since it is a primary structural component.
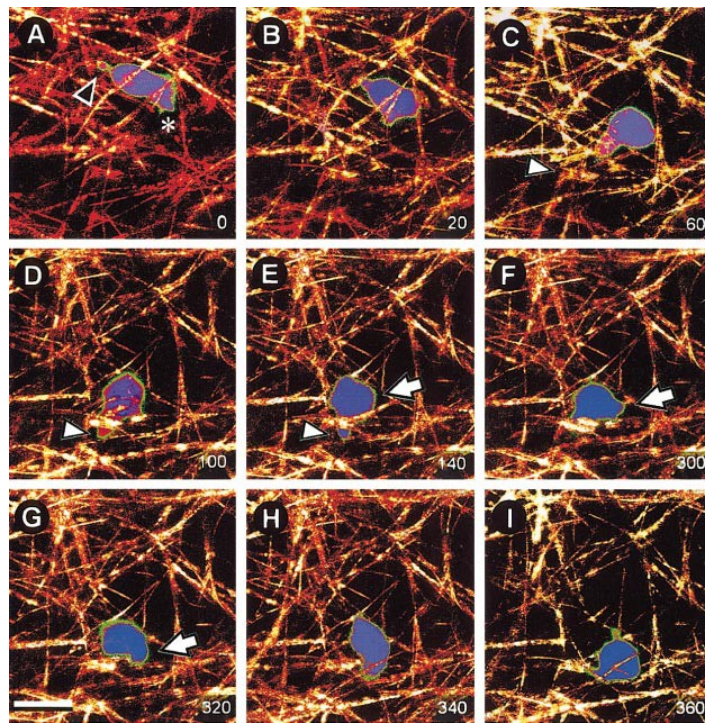
Figure 1.2: Amoeboid migration of a T lymphocyte through a 3D collagen matrix after staining with calcein-AM, and imaged by confocal time-lapse reflection and fluorescence microscopy [53]. Time elapsed is displayed in seconds. Asterisk (*) shows cell leading edge, while white and black arrowheads show pseudopod extension and uropod, respectively. Scale bar, 10 μm. Reprinted from The Journal of Leukocyte Biology, P. Friedl, S. Borgmann, and E.-B. Bröcker, Amoeboid leukocyte crawling through extracellular matrix: lessons from the Dictyostelium paradigm of cell movement, **70**, 2001; Permission given by John Wiley and Sons.
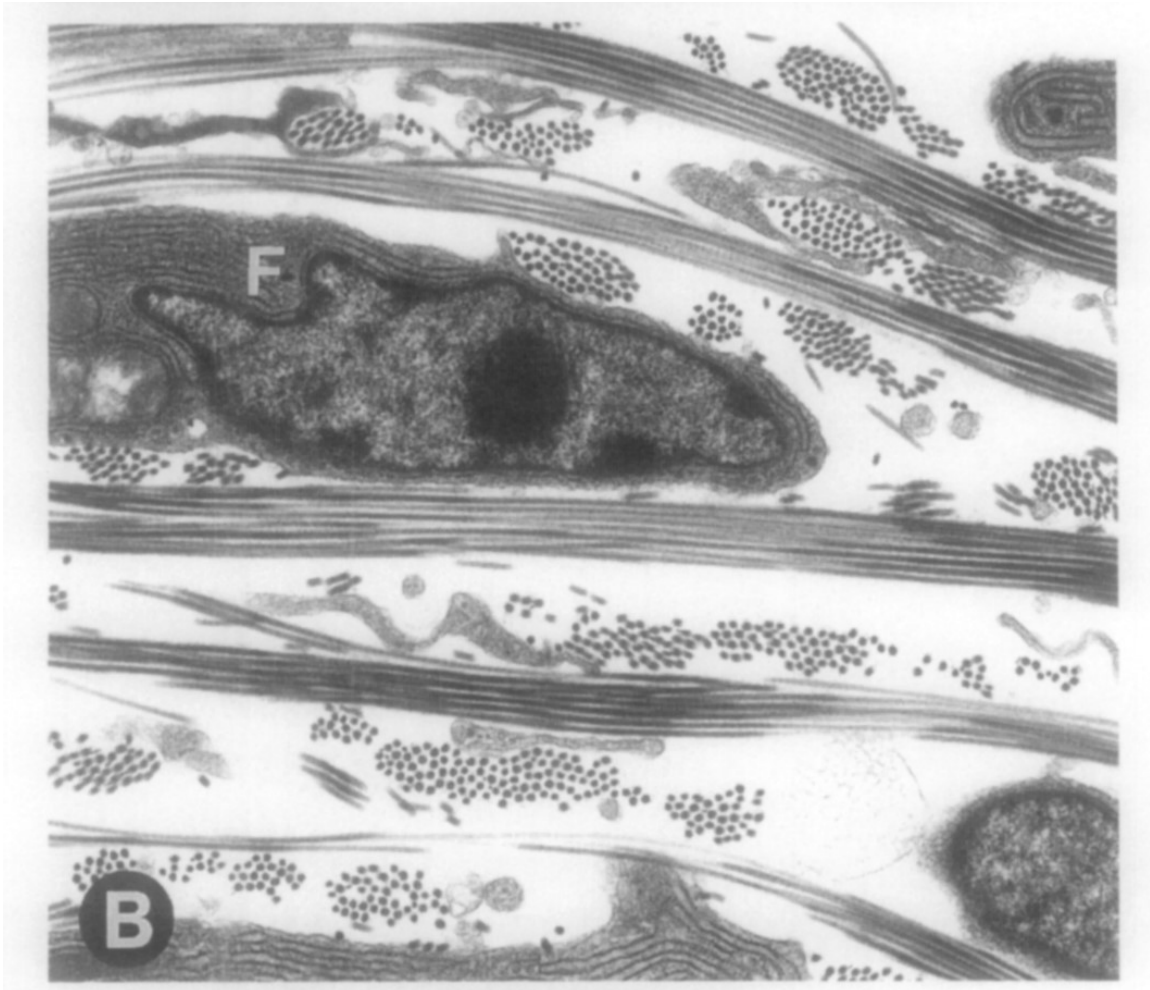
Figure 1.3: A transmission electron micrograph of the mid-dermal section of a 15 day-old chick embryo [77]. Collagen fibril bundles are arranged in an orthogonal manner with a fibroblast cell visible. Reprinted from the Journal of Structural Biology, **106**:1, C. Ploetz, E. I. Zycband, and D. E. Birk, Collagen fibril assembly and deposition in the developing dermis: Segmental deposition in extracellular compartments, 73-81, 1991 with permission from Elsevier.

1.3.2 Elastin

Like collagen, elastic fibers are also synthesized by fibroblasts and can be found throughout the body. Composed of fibrillin microfibrils and a crosslinked elastin core, these resilient fibers act like springs, reversing deformation in elastic tissues such as the

heart and lungs, blood vessels, skin, and bladder [49]. The importance of elastin can also be seen in old age, since elastic fibers are no longer created past adolescence, contributing to skin wrinkling and lack of resilience [47]. The physical mechanism behind elastic fibers is thought to be a change in entropy due to random coiling, with low-entropy stretched fibers shortening to a high-entropy state when relieved of stress [47].

1.3.3   Proteoglycans and Hyaluronan

Glycosaminoglycans, or GAGs, are long polysaccharide chains formed by repeating disaccharide sugar units [45]. All vertebrate cells are known to synthesize GAGs, which are generated from cell modifications to proteoglycan proteins and secreted into the extracellular matrix [46]. Due to their polar nature, GAGs are highly attractive to water, and are therefore thought to act as elastic water-trapping space fillers, attracting over fifty times their weight in water [41]. This ability allows GAGs to act as viscous lubricants within tissues [42] in addition to providing mechanical properties in cartilage and serving to inhibit the migration of microorganisms [48]. Hyaluronan, formerly known as hyaluronic acid, is considered separately from the other glycosaminoglycans due to its formation in the plasma membrane as opposed to other GAGs [44]. Furthermore, hyaluronan is considerably larger in size, estimated to exceed twenty-thousand disaccharide components, totaling more than twenty micrometers in length [47]. Unsurprisingly, due to the complexity in GAG synthesis, a degree of variability exists within the final properties of each chain [43]. This gives the fluid within the extracellular matrix locally heterogenous properties.

1.3.4   Adhesive Glycoproteins

Within the extracellular matrix, various types of cells are involved in a constant state of interaction with each other in addition to interactions with the common matrix macromolecules [45]. Adhesive glycoproteins are the "glue" that establishes these physical connections. Fibronectin, for instance, has bonding sites for cells, collagen, and proteoglycans in addition to crosslinking sites for other fibronectin proteins [47]. As a result, fibronectin plays an important role in extracellular matrix construction.

1.4 Biological Mechanisms of Cell Migration

Cellular locomotion is often an essential characteristic of many single- and multi-cellular organisms. The complexity of a motile cell may vary, from the simple case of a bacterium searching for food, to the complicated choreography required for a metastatic tumor cell to navigate through connective tissue. And while an untold diversity among methods of cellular locomotion exists, the purpose of this work is to model amoeboid migration by means of membrane protrusions. Under the standard model of cell migration, displacement occurs due to cycles of anterior membrane extension, subsequent anterior bond formation with a substrate, and finally, a posterior membrane contraction resulting in broken adhesive bonds in the rear and a net cell displacement [45]. The combination of protrusion, adhesion, and contraction is not exclusively required however. Cells have been observed migrating purely by protrusion [57,58] or contraction [12,20], or without the need for adhesion [50,57] demonstrating the capacity of strategies by which cells can migrate [63]. In an amoeboid cell, protrusive force is generated by growth of crosslinked actin filaments, contractile force is achieved through myosin motor proteins, and adhesion, while dispensable, is generally accomplished through integrins.

1.4.1 Actin

Actin is present inside a cell either in the form of unpolymerized G-actin monomers, or polymerized F-actin filaments approximately seven nanometers in diameter and up to several micrometers in length [45]. When perturbed by some stimulus, a complex cascade of events occurs, which results in actin being polymerized. Rho-family guanosine triphosphatases (GTPases) are activated, which themselves activate WASP/SCAR proteins resulting the nucleation of new actin filaments by the Arp2/3 complex [47]. Filaments can then be crosslinked to strengthen actin networks as seen in Figure 1.4, or bundled to form microvilli. Growing filaments form directly under the plasma membrane of the leading edge with piconewton-sized forces, thereby generating a membrane protrusion also known as a pseudopod [54]. Actin turnover and subsequent pseudopod retraction occurs when capping or severing proteins such as cofilin depolymerize F-actin filaments back into G-actin monomers. In addition to providing structure within the cell, polymerized actin in the cytoplasm contributes to its viscoelastic nature [47].

1.4.2 Myosin

Within the body, the myosin family of proteins is responsible for muscle contraction and the intracellular motility of organelles and other cargo, both of which are significantly important processes [54]. In a non-muscle motile cell, the myosin II variant protein converts chemical energy in the form of ATP into mechanical energy. Inside the cell, myosin II is normally distributed throughout the entire cell cortex. When migratory stimulation occurs, however, the myosin aggregates towards the rear of the cell [56]. Activation causes combinations of association and dissociation with an actin filament, coupled with conformational changes in the myosin head, resulting in the sliding of actin

filaments and an ensuing contractile force [45]. This procedure is illustrated below in Figure 1.5.
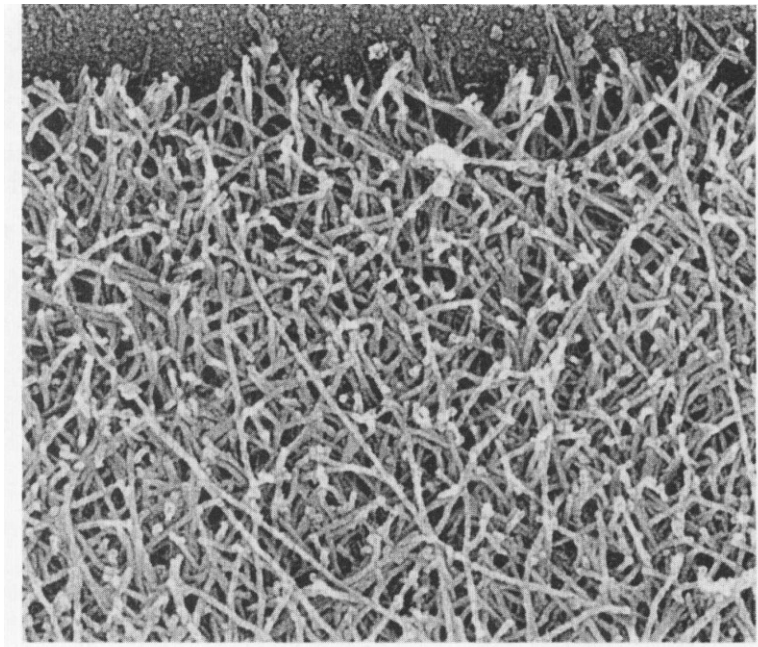
Figure 1.4: An electron micrograph of the actin network of the leading edge in a migrating keratocyte [76]. Republished with permission of T. D. Pollard from Molecular Mechanisms Controlling Actin Filament Dynamics in Non-muscle Cells, T. D. Pollard *et al*, Annual Review of Biophysics and Biomolecular Structure, **29**, 2000; permission conveyed through Copyright Clearance Center, Inc.
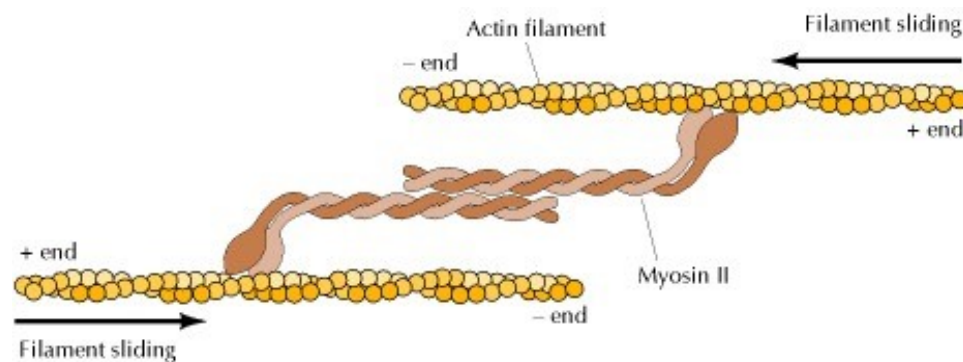
Figure 1.5: Illustration of a bipolar myosin II contractile assembly and its action on actin filaments [45]. Image taken from Figure 11.26 of The Cell: A Molecular Approach by Geoffrey M. Cooper © 2000. Reproduced with permission of the Licensor through PLSclear.

1.4.3 Adhesion

Under the standard model of cellular migration, adhesion proteins present in the leading edge of a cell adhere to ligands on the underlying substrate, effectively remaining in place as the cell advances forward [45]. When the adhesive group reaches the rear of the cell, contractile forces in the posterior cause these bonds to break as new bonds are again formed on the anterior. Cell adhesion is not exclusively found in cell migration, however. Skin and muscle cells, for instance, need to connect strongly with their neighbors to prevent rupture [47], while cells themselves are known to migrate with varying degrees of adhesive strength [59]. Because of this requirement in adhesive diversity, five different families of adhesion molecules are known to exist: cadherins, immunoglobulin-cell adhesion molecules (IgCAMs), selectins, mucins, and integrins [47].

Cadherins generally interact with other cadherins on adjacent cells in a calcium-dependent fashion, forming stable cell-cell junctions where adjacent cytoskeletons are linked together. The four remaining adhesion molecules, on the other hand, are transient in interaction. IgCAMs can be homophilic or heterophilic, meaning they can recognize and adhere to both similar or different adhesion molecules, respectively. Selectins are utilized primarily in the microcirculation, providing transient interactions for white blood cells to attach to the epithelial lining, after which, stronger integrin-based adhesions form, allowing the cell to leave the blood through extravasation [45]. Mucins are also present on white blood cells and endothelial cells, using carbohydrates to bond to selectins of other cells [47]. It is also possible that multiple adhesion protein families can work in tandem, such as during an extravasation event.

Integrins are present in most animal cells and are considered to be the primary adhesion protein responsible for connecting cells to the extracellular matrix. Integrins are composed of two transmembrane dimers labeled as α and β, which due to several unit types, provides over twenty different isoforms of integrins, each capable of bonding to specific ligand types [45]. Integrins bind to collagen and fibronectin within the extracellular matrix, thus allowing for sufficient adhesion as shown in Figure 1.6. The number and degree to which integrins are utilized may vary depending on cell properties as discussed in the following section.
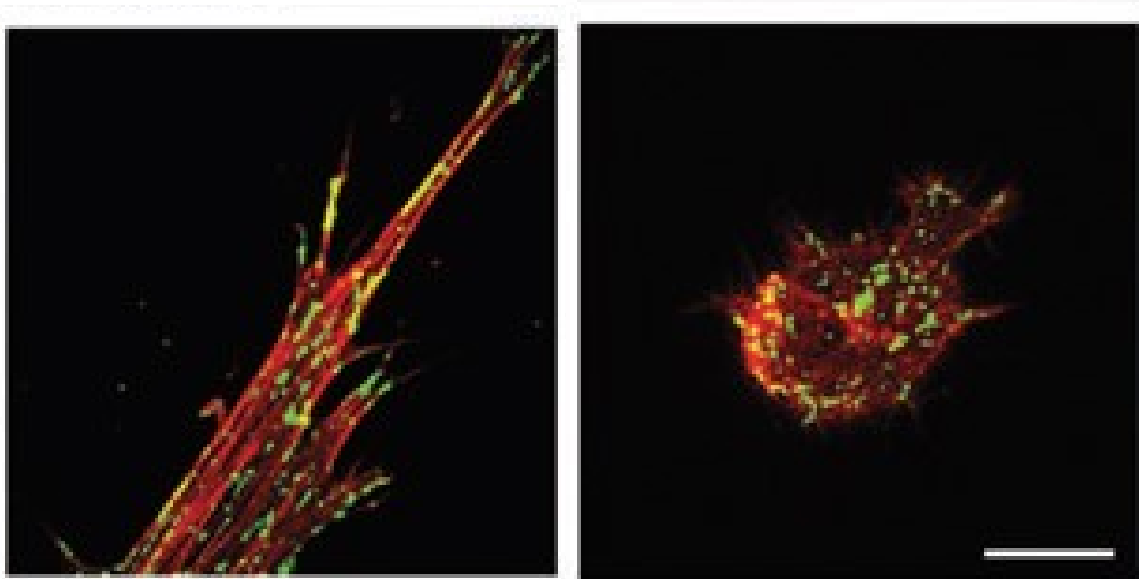
Figure 1.6: Human fibroblast distribution of $\beta 1$ integrin (green) and F-actin (red) in 3D matrices [149]. Scale bar represents 10 μm. **(Left)** Migration through 3D fibrin matrix. **(Right)** Migration through 3D basement membrane extract. Significant difference in cell morphology is seen when migrating through different tissue scaffolds. Image is from Tissue Engineering: Part A, **17**:5-6, 2011. Direct Comparisons of the Morphology, Migration, Cell Adhesions, and Actin Cytoskeleton of Fibroblasts in Four Different Three-Dimensional Extracellular Matrices, K. M. Hakkinen, J. S. Harunaga, A. D. Doyle, and K. M. Yamada. Reproduced with permission from Mary Ann Liebert Publishers.

1.5 Amoeboid vs. Mesenchymal Migration

Evolution has produced an untold assortment of cells with unique properties and behaviors. Therefore, it is no surprise to imagine that cells can achieve motility through very diverse means. Within the category of cells driven by membrane extensions, however, two distinctive morphologies merit discussion: amoeboid and mesenchymal locomotion. The amoeboid mode is characterized by an ellipsoidal cell shape only weakly dependent on integrin adhesion, which uses its high membrane deformability to quickly squeeze through or navigate around obstacles [54]. The mesenchymal mode of motility, on the other hand, is characterized as a slow moving, spindle-shaped morphology which is highly dependent on integrin-based adhesion and capable of degrading connective tissue through proteolytic enzyme remodeling. Figure 1.7 shows images comparing the amoeboid and mesenchymal morphologies, while Table 1.1 lists the key differences between the two modes of locomotion. One noteworthy difference is migration speed, with the amoeboid mode possibly reaching one to two orders of magnitude higher than the mesenchymal mode. Another important distinction is the degree of adhesiveness, as amoeboid cells are described to have low and transient levels of integrin expression on their membranes, while mesenchymal cells form clusters of focal contacts which generate high adhesive forces [28].

Further interest between the mesenchymal and amoeboid morphologies arises from recent studies, which have shown the blocking of matrix degrading proteolytic enzymes in cancer cells did not completely inhibit tumor cell migration [1]. It was observed that mesenchymal cancer cells could effectively convert to the amoeboid mode in what is known as a mesenchymal to amoeboid (MAT) transition. This compensation mechanism

elevates the importance of the amoeboid form of locomotion, since in addition to cancer cells, immune cells, nerve cells, epithelial cells, and even embryonic cells utilize the amoeboid morphology [45], making an investigation into its inner workings well worthwhile.
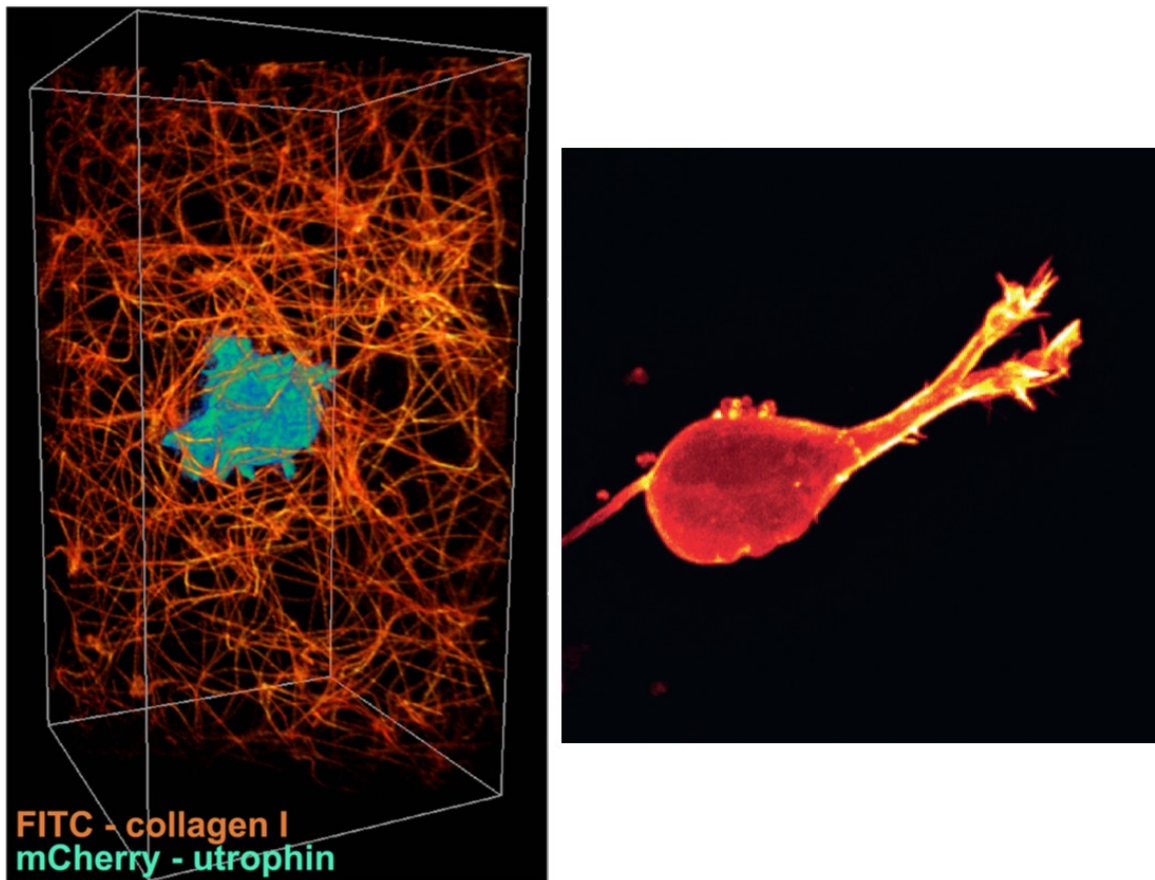
Figure 1.7: Amoeboid versus mesenchymal modes of motility. **(Left)** Neutrophil-like human HL-60 cell expressing mCherry-utrophin in a fluorescently labeled collagen matrix [75]. From B.-C. Chen *et al*. Lattice light-sheet microscopy: Imaging embryos to molecules at high spatial resolution. *Science*, **346**:6208, 2014. Reprinted with permission from AAAS. **(Right)** Lifeact–GFP expressing cancer cell within a 3D collagen hydrogel [26]. Reproduced with permission under the Creative Commons Attribution License (CC BY) from P. T. Caswell and T. Zech. Actin-based cell protrusion in a 3D matrix. *Trends in Cell Biology*, **28**:10, 2018. https://doi.org/10.1016/j.tcb.2018.06.003

Characteristic	Mesenchymal	Amoeboid
Cell shape	Elongated, fibroblast-like (length 50–200 µm)	Roundish/elliptoid (length 10–30 µm)
Growth in culture	Adhesive	Growth in suspension
Migration velocity	Low (0.1–1 µm/min)	Low to high (0.1–20 µm/min)
Cell-matrix interactions	Integrins and proteases focalize	Integrins and proteases are non-focalized
Structure of actin cytoskeleton	Cortical and stress fibres	Cortical
Adhesion force generated	High, fibre pulling and bundling	Low, minor fibre bending
Proteolytic extracellular-matrix remodelling	Present to extensive	Not present
Cellular migration mechanism	Traction dependent	Propulsive, cytoplasmic streaming
Mechanism overcoming matrix barriers	Path generation, formation of proteolytic ECM defects	Path finding, propulsion and cytoplasmic forward flow ('streaming'); squeezing through narrow regions (constriction ring)
Prototypic non-neoplastic cell	Fibroblast, smooth-muscle cell	Lymphocyte, neutrophil
Neoplastic cells, carcinoma	Fibrosarcoma, glioblastoma, defifferentiated epithelial cancer	Lymphoma, small-cell lung carcinoma, small-cell prostate cancer

Table 1.1: Characteristics describing the amoeboid and mesenchymal modes of motility [28]. Reprinted by permission from Copyright Clearance Center, Inc: Springer Nature, Nature Reviews Cancer, Tumour-cell invasion and migration: diversity and escape mechanisms, P. Friedl and K. Wolf, © 2003.

1.6 Scope of dissertation

As detailed in the above discussion, cell migration is a complex, multiscale process which combines aspects of biology, fluid dynamics, and solid mechanics. The amoeboid mode in particular presents an even more interesting challenge, due to its highly deformable membrane and fast speeds compared with other motility mechanisms. Additionally, pseudopod generation is a highly dynamic process involving internal and external signaling, as well as complex biochemistry within the cell. With that being said, the objective of this dissertation was to construct a three-dimensional computational model of amoeboid cell migration, which couples cell membrane deformability, protein dynamics, fluid interaction, and extracellular matrix geometry. A comprehensive analysis is performed on cell dynamics as both cell and matrix properties are varied.

1. **Numerical Methodology (Chapter 2):** An accurate computational model for a three-dimensional amoeboid cell membrane is developed using a front-tracking continuous forcing immersed boundary method. This membrane resists shear, area dilation, and bending. Pseudopod generation is accomplished through an activator-inhibitor system driven by surface reaction-diffusion equations. Flow is modeled using the unsteady stokes equation, which is solved using the projection method by finite volume and spectral methods. Matrix geometry is included using a sharp-interface ghost node method. This aggregate model is then used to study the behavior and dynamics of an amoeboid cell under various cell states and matrix geometries.

2. **Pseudopod-driven swimming of an amoeboid cell in a fluid medium (Chapter 3):** Recent experiments regarding amoeboid cells have demonstrated a capability to swim in a liquid medium through the use of pseudopod-driven membrane extensions [2-3]. These extensions appear at the cell front, then migrate towards the rear of the cell, mimicking paddles, until finally retracting. No discrete adhesion force was modeled. Consistent with Purcell's Scallop Theorem [6], the model discussed in Chapter 2 is applied to simulate pseudopod-driven amoeboid swimming in an unbounded fluid medium. Parameter studies are performed in order to determine the effect of varying membrane deformability, surface protein diffusivity, and cell-to-fluid viscosity ratio on cell behavior and dynamics.

3. **Adhesion-independent pseudopod-driven migration of an amoeboid cell in extracellular matrix geometry (Chapter 4):** Previous studies have shown three-dimensional amoeboid cell migration both in vivo [50] and in vitro [51] was essentially unaffected by the knockdown or absence of adhesion as compared to

wild-type cells. This is made possible by a highly deformable membrane which makes use of footholds and constriction rings to gain traction while migrating through connective tissue [52]. Pseudopod-driven amoeboid cells are introduced into periodic extracellular matrix geometries. Discrete adhesive interactions between the cell and matrix are not considered. The influence of membrane deformability, and matrix obstacle size and porosity are studied.

4. **Pseudopod-driven migration of an amoeboid cell in various extracellular matrix geometries with weak adhesion (Chapter 5):** While amoeboid cells are fully capable of migration through extracellular matrix sans adhesion, studies have suggested a weak, diffuse network of adhesion proteins exists on the cell's plasma membrane [53]. As such, the work on amoeboid migration through extracellular matrices considered in Chapter 4 is expanded upon with the introduction of a weak adhesion model derived from the work of Bell [4] and others [5,16]. In addition, three distinct extracellular matrix geometries are used as approximations to specific tissue types or as theoretical exercises. Studies are performed on the effect of membrane deformability, adhesive strength, and matrix geometry.

Chapter 2
Numerical Methodology

2.1 Problem Setup

Pseudopod-driven cellular migration through a three-dimensional computational domain is considered. In the case of migration through an unbounded fluid medium, the domain is triply periodic in order to reduce computational effort, while for the case of migration through extracellular matrix geometry, the domain is periodic in the x- and z-directions but bounded by a no-slip wall in the y-direction. The length of each side of the cubic domain is set to be 6π, where the number of Eulerian grid points is established to be 360 per dimension. The fluid is assumed to be initially quiescent and free of any pressure gradients until cell movement otherwise generates them.

2.2 Membrane Model

As discussed, the cell plasma membrane is composed of a lipid bilayer which provides a barrier between the cell and its environment. Directly beneath the bilayer is the cell cortex, which provides the cell with an actin-based structural framework. Because a generic amoeboid cell has a characteristic length of tens of micrometers, while the plasma membrane has thickness in the nanometer range, the cell membrane is therefore treated as having zero-thickness. In addition, because we do not consider the cell to have a nucleus or other organelles within the cytoplasm, the cell interior is treated as a viscous fluid-drop. Combined together, the lipid bilayer and cortex provide resistance against shear, area

dilation, and bending, with the actin cortex resisting shear, and the plasma membrane resisting area dilation and bending.

To model shear deformation and area dilation, we look to the work of Skalak *et al* [92] who developed constitutive energy functions for the lipid bilayer and cortex of red blood cell membranes. Equation 2.1 below illustrates the strain energy model, where G_S is the membrane shear modulus, and $I_1 = \epsilon_1^2 + \epsilon_2^2 - 2$ and $I_2 = \epsilon_1^2 \epsilon_2^2 - 1$ are the invariants of Green's strain tensor. The terms ϵ_1 and ϵ_2 are the principal stretch ratios.

$$W_E = \frac{G_S}{4}[(I_1^2 + 2I_1 - 2I_2) + CI_2^2] \tag{2.1}$$

Green's strain tensor arises from continuum mechanics and is defined by Equation 2.2, where $\boldsymbol{F} = \partial \boldsymbol{x}/\partial \boldsymbol{X}$ is the deformation gradient tensor, and $\boldsymbol{x}$ and $\boldsymbol{X}$ are the current and initial cell configurations in space, respectively. $\boldsymbol{I}$ is the identity tensor.

$$\boldsymbol{E} = \boldsymbol{F}^T \cdot \boldsymbol{F} - \boldsymbol{I} \tag{2.2}$$

The first grouped term in Equation 2.1 is associated with shear deformation, while the last term accompanies area dilation. The parameter C controls the allowable amount of area dilation, and is set to unity. Changes in cell surface area as high as 30% have been observed experimentally in the amoeba Dictyostelium discoideum [98], while area fluctuations are further possible through membrane wrinkles and vesicle fusion or detachment from endocytosis [99].

With knowledge of the strain energy function W_E, the principal elastic stresses on the membrane are found via Equations 2.3 and 2.4.

$$\tau_1 = \frac{1}{\epsilon_2} \frac{\partial W_E}{\partial \epsilon_1} \tag{2.3}$$

$$\tau_2 = \frac{1}{\epsilon_1} \frac{\partial W_E}{\partial \epsilon_2} \tag{2.4}$$

The elastic stresses present in the membrane from shear and area dilation are solved for by the finite element method, which is detailed in [95-97]. To begin, the cell membrane is discretized into 20,480 Delaunay triangles characterized by 10,242 nodes as seen in Figure 2.1A and B. A linear displacement field $\boldsymbol{v}$ is then defined over each element using shape functions (N) as seen in Equation 2.5, where the index i corresponds to the local vertex number of the element.

$$\boldsymbol{v} = N_i \boldsymbol{v}_i \tag{2.5}$$

Knowledge of the shape functions allows for the calculation of the deformation gradient tensor $\boldsymbol{F}$, which subsequently leads to the principal stretch ratios and the stress tensor $\boldsymbol{\tau}$. The in-plane elastic force on each element can then be calculated by the principal of virtual work, $\boldsymbol{f}_e^m = -\partial W_E/\partial \boldsymbol{v}$. The force at each node is then found by compiling the resultant as in Equation 2.6, where $\boldsymbol{P} = \epsilon_1 \epsilon_2 \boldsymbol{\tau} \cdot \boldsymbol{F}^{-T}$ is the first Piola-Kirchhoff stress tensor, and S_m is the area summation of the m elements surrounding the node in question.

$$f_e = \sum_m \int_{S_m} \frac{\partial \boldsymbol{N}}{\partial \boldsymbol{X}} \cdot \boldsymbol{P} dS \tag{2.6}$$
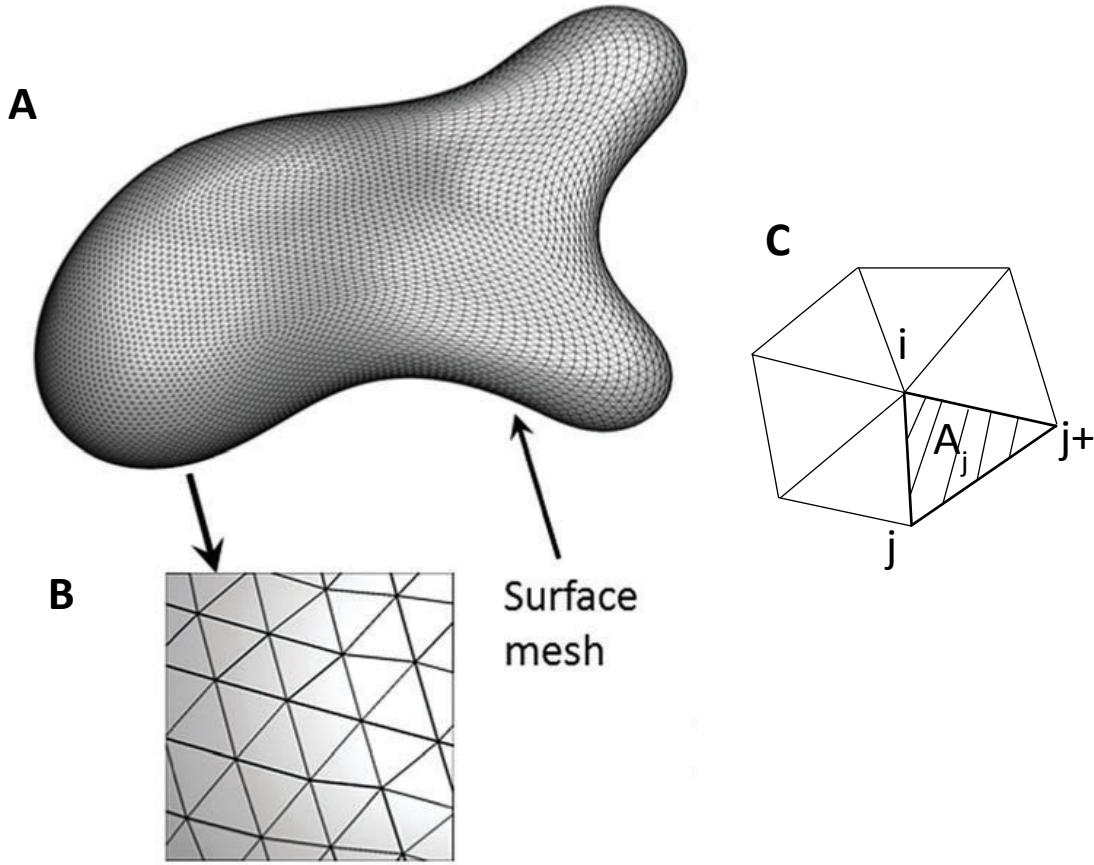
Figure 2.1: **(A)** Cell membrane composed of Delaunay triangular elements. **(B)** Zoomed-in view of Delaunay mesh. **(C)** Example of indices used for numerical curvature gradient calculation. Adapted from [148] with the permission of AIP Publishing.

To model the membrane bending resistance, we implement Helfrich's bending energy formulation as seen by Equation 2.7, where E_B is the bending stiffness, κ is the mean curvature, c_0 is the spontaneous curvature, and S is the cell surface area [93]. The spontaneous curvature serves to quantify the difference between the two layers of the lipid bilayer, which may be subjected to unalike chemical compositions or surroundings [94]. With this in mind, and a lack of sufficient literature on the subject, c_0 is set to zero.

$$W_B = \frac{E_B}{2} \int_S (2\kappa - c_0)^2 dS \tag{2.7}$$

A numerical implementation of Equation 2.7 is performed by considering the bending force density f_b in Equation 2.8, where κ_g is the Gaussian curvature and $\boldsymbol{n}$ is the surface outward normal. $\Delta_{LB} = \nabla_s \cdot \nabla_s$ is the Laplace-Beltrami operator, where $\nabla_s = \boldsymbol{I}_s \cdot \nabla$ is the surface gradient operator, and $\boldsymbol{I}_s = \boldsymbol{I} - \boldsymbol{nn}$ is the surface projection matrix.

$$f_b = E_b\left[(2\kappa + c_0)(2\kappa^2 - 2\kappa_g - c_0\kappa) + 2\Delta_{LB}\kappa\right]\boldsymbol{n} \tag{2.8}$$

The outward normal vector $\boldsymbol{n}$ is found by taking the vector sum of the element normal vectors surrounding a vertex, then taking a weighted average and normalizing to a unit vector. The curvatures κ and κ_g are calculated through the use of a quadratic surface fitting, the form of which is detailed is Equation 2.9. The parameters (x', y', z') represent the local coordinate system of the node in question, where z' is oriented in the direction of the approximated normal vector.

$$z' = ax'^2 + bx'y' + cy'^2 + dx' + ey' \tag{2.9}$$

As detailed in [100], an iterative process is performed where the coefficients of Equation 2.9 are found using the nearest vertices around a given point, along with the least-squares method until a satisfactory convergence for the estimated normal vector is achieved. The coefficients can then be used as follows to find each curvature.

$$\kappa = -\frac{a + c + ae^2 + cd^2 - bde}{(1 + d^2 + e^2)^{3/2}} \tag{2.10}$$

$$\kappa_g = \frac{4ac - b^2}{(1 + d^2 + e^2)^2} \tag{2.11}$$

Finally, the surface gradient and Laplace-Beltrami numerical implementation are discussed. Utilizing tools from the image reconstruction field [101-102], $\Delta_{LB}\kappa$ can be

written as follows, where H is the sum of element areas surrounding a vertex, and $N_1(i)$ contains the set of vertices directly surrounding node i. $\tilde{n}_j$ is the unit outward normal to the edge connecting points j and j_+ as detailed in Figure 2.1C.

$$\Delta\kappa_i = \frac{1}{2H} \sum_{j \in N_1(i)} \tilde{n}_j \cdot \left(\nabla_s\kappa_j + \nabla_s\kappa_{j+}\right)\|x'_j - x'_{j+}\| \tag{2.12}$$

The surface gradient of curvature $\nabla_s\kappa_j$ can be found through taking a weighted average on the gradients of curvature on the adjacent elements surrounding vertex i as seen by Equation 2.13.

$$\nabla_s\kappa_j = \frac{1}{H} \sum_{k \in N_1(j)} A_j \nabla_{T_j}\kappa \tag{2.13}$$

A_j is the area of triangle j denoted by the set of points $[i, j, j_+]$. Lastly, $\nabla_{T_j}\kappa$ can be implemented by the following equation with the assumption that κ only varies linearly in each element.

$$\nabla_{T_j}\kappa = \frac{1}{4A_j^2}\left\{\kappa_i\left[(x'_i - x'_j) \cdot (x'_j - x'_{j+})(x'_{j+} - x'_i) + (x'_i - x'_{j+}) \cdot (x'_{j+} - x'_j)(x'_j - x'_i)\right]\right.$$

$$+ similar\ terms\ with\ i\ and\ j\ interchanged$$

$$\left. + similar\ terms\ with\ i\ and\ j_+\ interchanged\right\} \tag{2.14}$$

The cell membrane can additionally be considered as viscoelastic, which has been done in prior works [95,103]. A Kelvin-Voigt model was implemented, where the membrane viscoelastic behavior was expressed as a sum of elastic and viscous stresses as shown in Equation 2.15.

$$\tau = \tau^e + \tau^v \tag{2.15}$$

The elastic stresses have been considered previously in Equations 2.3 and 2.4, while the viscous stress is modeled as follows, where μ_m is the membrane shear viscosity and $\boldsymbol{D}$ is the strain rate tensor. The viscous stress is computed using a time-convolution integral which relates the stress to its strain history.

$$\tau^v = 2\mu_m \left[\boldsymbol{D} - \frac{1}{2} tr(\boldsymbol{D})\boldsymbol{I}_S\right] \tag{2.16}$$

Validation of the membrane model has been performed previously in [107], where the aspiration of a red blood cell by a micropipette was analyzed and compared with experimental data, with a good agreement observed. General cell smoothness is seen even after extreme deformations occur, therefore confirming the accuracy of the method.

2.3 Pseudopod Pattern Generation Model

A key element to simulating amoeboid motility is a model which captures the dynamic nature of pseudopod extension, bifurcation, and retraction. Biologically speaking, membrane extension is accomplished through a complex series of events triggered inside the cell, resulting in crosslinked polymerized actin filaments generating protrusive forces. Pseudopod retraction then follows as the actin network is disassembled. However, due to the numerous amounts of signaling channels and proteins required to activate pseudopod dynamics, a more realistic modeling approach is taken. Here we model the cell protein dynamics on the surface of the cell using a coarse-grain method. This method relies on the generation of Turing instabilities, or spatiotemporal patterns generated from the combined reaction and diffusion of coupled discrete chemical species [78]. Turing models, also referred to as activator-inhibitor systems or diffusion-driven instabilities, have been applied in the past to study a great number of problems, from chemical reactions [81-82],

to embryonic development [83] and animal skin or fur patterns [79-80]. Additionally, Turing models have also been used to study amoeboid migration in two-dimensional [7-10] and three-dimensional [11] environments.

In our model, a Meinhardt-type activator-inhibitor system [7,84] is used to generate dynamic patterns which will be coupled to regions of pseudopod growth. Equations 2.17 to 2.19 below illustrate the system, where a_1, a_2, and a_3 are the concentrations of the local activator, global inhibitor, and local inhibitor, respectively. We consider the activator to represent the concentration of polymerized actin filaments. Similar works have presumed analogous correlations between actin and activator concentrations [8,32] or other proteins which are known to directly precede a motile response [9,29]. Along a similar vein, the global and local inhibitors are assumed to be related to the concentration of capping and severing proteins which act to stop or reverse the growth of actin.

$$\dot{a_1} = D_1\Delta_S a_1 + \frac{(r_1 + 5000\epsilon)\left(\frac{a_1^2}{a_2} + k_1\right)}{(s_3 + a_3)(1 + s_1 a_1^2)} - r_1 a_1 \tag{2.17}$$

$$a_2 = \frac{1}{S}\int_S a_1 dS \tag{2.18}$$

$$\dot{a_3} = D_3\Delta_S a_3 - r_3 a_3 + k_2 a_1 \tag{2.19}$$

A brief description of each parameter is as follows [84]. D_1 and D_3 are the surface diffusivities of the local activator and inhibitor, while S is the surface representation of the deforming cell. r_1 is linked to the generation and decay rate of the local activator, while k_2 sets the rate of local inhibitor production. Similarly, r_3 is the decay rate of the local inhibitor. k_1 is a basic activator production constant to initiate activator autocatalysis. s_1

controls the activator saturation level, thereby tuning the number of individual instabilities, and subsequently, the number of pseudopods which can be generated. s_3 is the Michaelis-Menten constant, often used to model enzymatic reactions, which sets the affinity of the inhibitor towards the activator. Finally, Δ_S is the surface laplacian, while the dot superscript seen on the left-hand side of the equations represents the time derivative. We note that Equations 2.17 and 2.19 have absorbed the rate parameter γ used in [7]. Table 2.1 below provides the dimensionless parameter values used in each simulation.

Parameter	D_1	D_3	r_1	r_3	k_1	k_2	s_1	s_3
Value	1	2-3	1000	650	0.1	250	1E-4	0.2

Table 2.1: Dimensionless parameters used in the Meinhardt activator-inhibitor system.

Lastly, the parameter ϵ serves as a spatiotemporal stochastic random noise, which is fed into the local activator equation in order to create perturbations in concentration. A chemotactic signal can additionally be added by biasing the noise, as has been done in other works [7-9] but is not considered here. The random noise ϵ is generated from an Ornstein-Uhlenbeck stochastic differential equation which is described below in Equation 2.20. W represents the Wiener process, which provides the stochastic behavior module.

$$d\epsilon = -\epsilon dt + (2.0E - 4)dW \qquad (2.20)$$

An Euler-Maruyama method (Equation 2.21) is used to numerically approximate the solution for each element of the cell. R is a random number taken from a normal distribution with a mean of zero and a standard deviation of unity. Additionally, μ is the

mean, σ is the variance, and θ is the rate of reversion to the mean. Parameter values are displayed below in Table 2.2. The timestep Δt is globally set to be 1.0E-3.

$$\epsilon^{n+1} = \epsilon^n + \Delta t(\theta^n[\mu - \epsilon^n]) + \sigma^{n+1}R\sqrt{\Delta t} \tag{2.21}$$

Parameter	Value
μ	0
σ	2.0E-4
θ	1

Table 2.2: Parameters used in the Euler-Maruyama method solution. μ is the mean, σ is the variance, and θ is the rate of reversion to the mean.

The coupled activator-inhibitor system is solved on the surface of the deforming cell using an evolving surface finite element method developed by Dziuk and Elliott [85]. Details of the solution are presented here. Consider the generic, time-dependent differential equation seen in Equation 2.22. Here, D is the diffusivity and $f(a)$ is the reaction term which may be a function of multiple species.

$$\dot{a} - D\Delta_S a - f(a) = 0 \tag{2.22}$$

We first multiply by an arbitrary weak function (ϕ) and integrate over the cell surface.

$$\int_S [\dot{a}\phi - D(\Delta_S a)\phi - f(a)\phi]\, dS = 0, \quad \forall \phi \tag{2.23}$$

Equation 2.23 can be simplified using integration by parts, in which one of the resulting terms will vanish because the cell surface is closed, so no net flux occurs [86]. This leads to Equation 2.24.

$$\int_S [\dot{a}\phi + D\nabla_S a \cdot \nabla_S \phi - f(a)\phi]\, dS = 0, \quad \forall \phi \tag{2.24}$$

This equation is displayed below with a superscript "e" added to indicate that approximations are to be taken.

$$\int_{S^e} [\dot{a}^e \phi^e + D\nabla_S^e a^e \cdot \nabla_S^e \phi^e - f(a^e)\phi^e]\, dS = 0, \quad \forall \phi \tag{2.25}$$

Approximations are now introduced for the species a and arbitrary function ϕ for each triangular element using basis functions.

$$a^e = \sum_{j=1}^{N_e} \alpha_j \chi_j \tag{2.26}$$

$$\phi^e = \sum_{k=1}^{N_e} \chi_k \tag{2.27}$$

$$\frac{d}{dt} \int_{S_e} \sum_{j=1}^{N_e} \alpha_j \chi_j \chi_k + D \int_{S_e} \sum_{j=1}^{N_e} \alpha_j \nabla_S^e \chi_j \cdot \nabla_S^e \chi_k - \int_{S_e} \sum_{j=1}^{N_e} f^e \chi_j = 0 \tag{2.28}$$

With further simplification, the above can be reduced into an ordinary differential equation for each element as follows.

$$\frac{d}{dt}(M^e \alpha^e) + K^e \alpha^e = F^e \tag{2.29}$$

Here, M^e is the element mass matrix, K^e is the element stiffness matrix, and F^e is an element forcing vector as described below. The matrix B is the gradient operator matrix derived from the triangular shape functions, whereas A^e is the area of an element. The mass and stiffness matrices may be fully solved on three-node triangular elements without the use of integration, while Gauss quadrature is needed for the forcing term.

$$M^e = \int_{S^e} \chi_j \chi_k \, dS = \frac{A^e}{12} \begin{bmatrix} 2 & 1 & 1 \\ 1 & 2 & 1 \\ 1 & 1 & 2 \end{bmatrix} \tag{2.30}$$

$$K^e = D \int_{S^e} \nabla_S^e \chi_j \cdot \nabla_S^e \chi_k \, dS = D \int_{S^e} B^T B \, dS \tag{2.31}$$

$$F^e = \int_{S^e} f^e \chi_j \, dS \tag{2.32}$$

Equation 2.29 can be globally assembled over each element, resulting in the final form of the activator-inhibitor equation below. A forward difference approximation is utilized for the time derivative, while a semi-implicit method is used for the remaining terms.

$$\frac{d}{dt}(Ma) + Ka = F \tag{2.33}$$

This method is used to solve for the local activator and inhibitor concentrations on the cell surface at each timestep. With knowledge of a_1, the solution for the global inhibitor a_2 is easily found as the average of local activator over the cell surface (Equation 2.34), where N is the total number of nodes. Note that this species is spatially uniform over the cell surface.

$$a_2 = \frac{1}{N} \sum_{i=1}^{N} a_1^i \tag{2.34}$$

Knowledge of the local activator concentration on each cell node will later tie into the protrusive force, which we assign a linear relation as seen below in Equation 2.35. The force is directed in the outward normal direction of the cell membrane by the unit vector $\boldsymbol{n}$, where ξ is deemed the force per actin filament. A linear relation is chosen for the protrusive force [7] since the complexities between cell signaling and actin polymerization are not fully understood, while computational models using other force relations have found no significant differences [9].

$$\boldsymbol{F}_p = \xi a_1 \boldsymbol{n} \tag{2.35}$$

2.3.1 Validation

Both qualitative and quantitative validations have been performed to determine the accuracy of our surface finite element method. Qualitative tests were done by solving the Fitzhugh-Nagumo activator-inhibitor system on a rigid sphere as seen in [87]. Figure 2.2 below illustrates our solution as a spiral wave meandering over the spherical surface for several timesteps. We note that even after sufficient time has elapsed, the wave is still well resolved, demonstrating the accuracy of our method.

Qualitative validation was also done by comparing the types of Turing instabilities we were capable of generating against existing models in the literature. Through adjustment of several parameters in Equations 2.17-2.19, our finite element method is capable of producing arrays of high-concentration spots of varying sizes and densities. Furthermore, dynamic and bifurcating patterns are also possible, while variations of stripes and spots are

also seen. Figure 2.3 illustrates some of the diverse patterns which have been generated.

We note that the results agree very well with works which have modeled activator-inhibitor

systems previously [7,86,88,89].
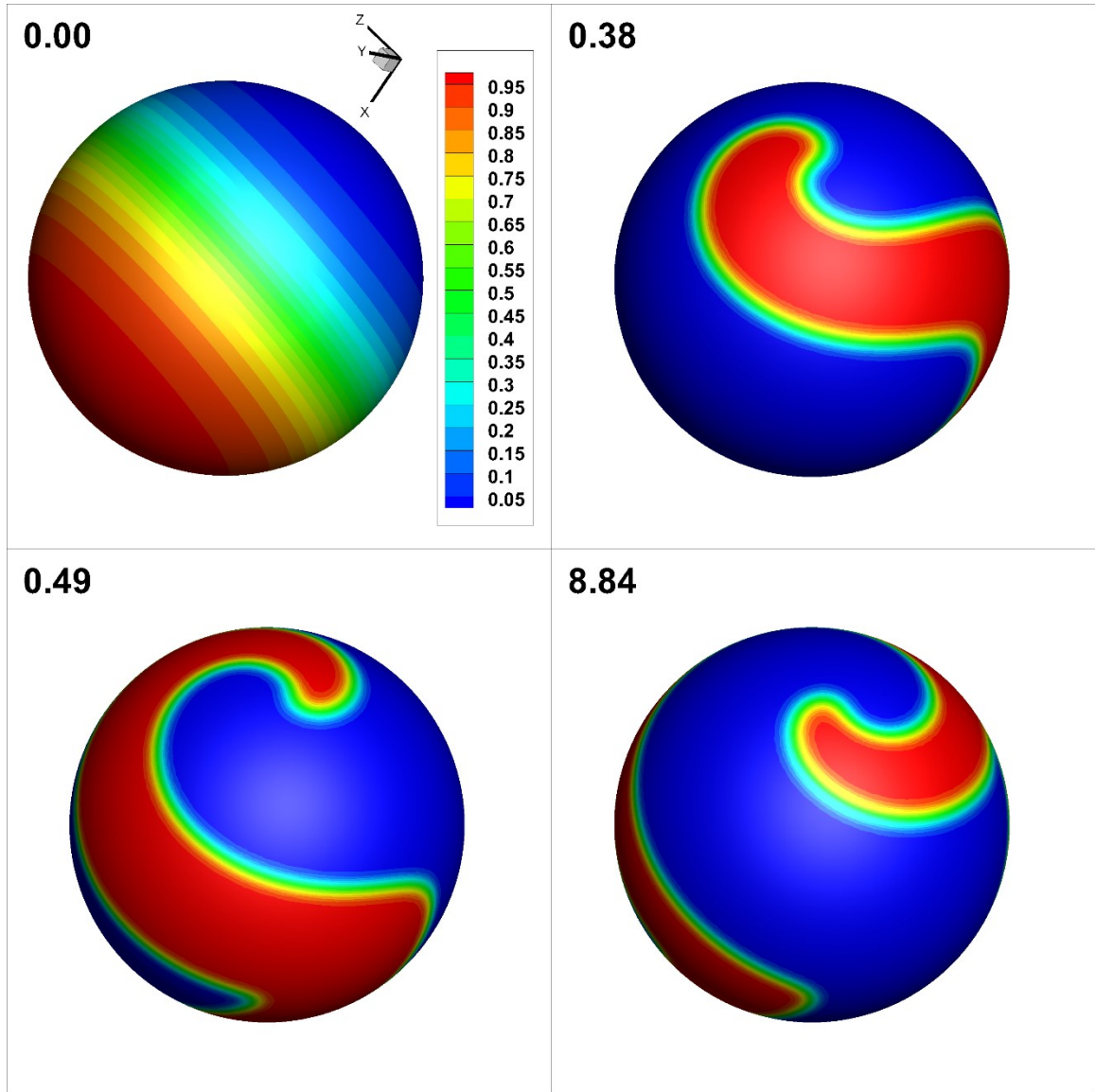
Figure 2.2: Solution of the Fitzhugh-Nagumo activator-inhibitor system on a rigid sphere using our surface finite element method. Dimensionless solution times are indicated.
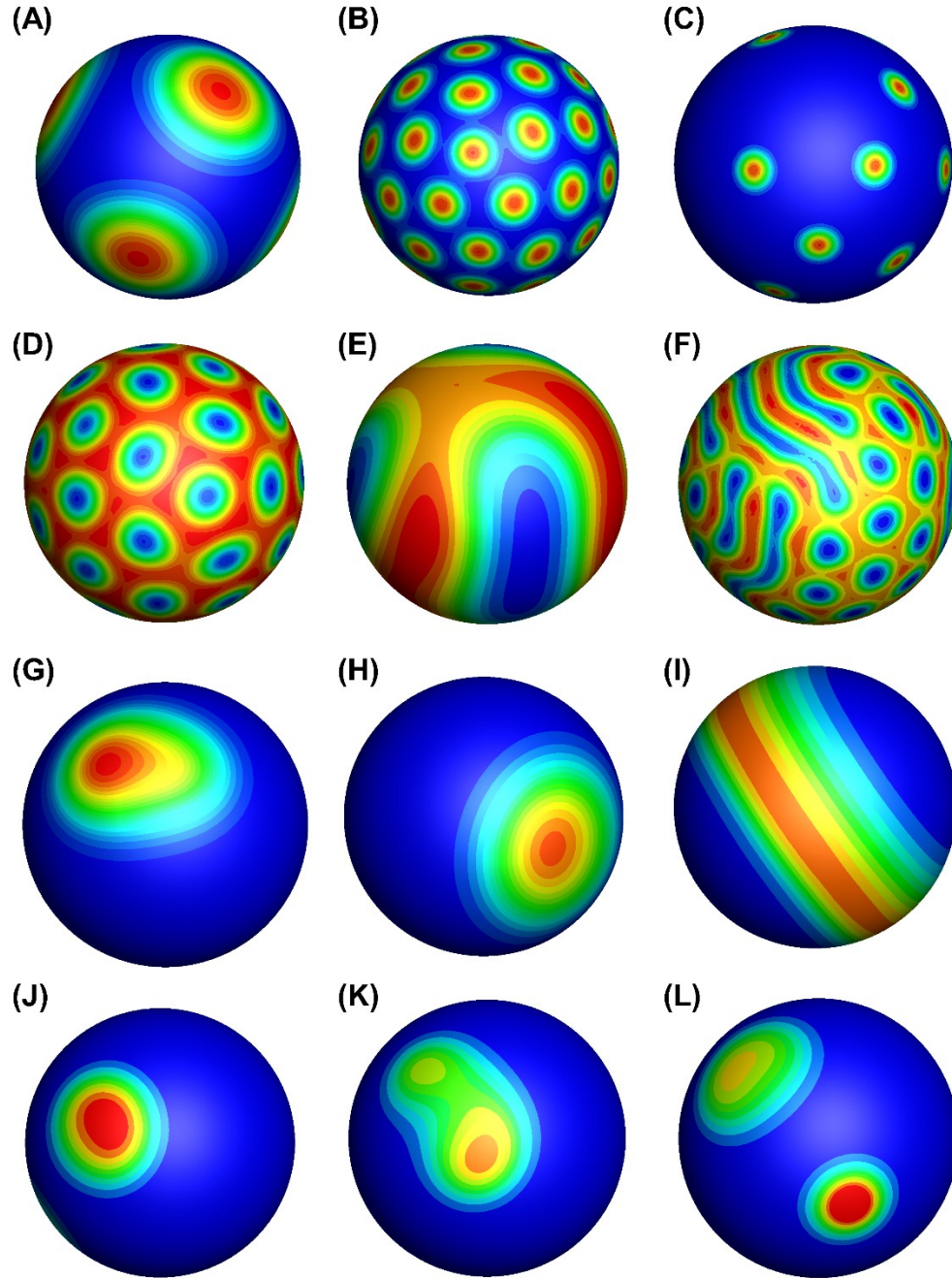
Figure 2.3: Diversity of patterns generated with our surface finite element method using Meinhardt kinetics. **(A)** Six large, stable spots. **(B)** Numerous small, stable spots. **(C)** Multiple small, stable spot scattered over the surface. **(D)** Numerous small, stable spots with inverted concentrations. **(E)** Stable ridges. **(F)** Combinations of inverted ridges and spots. **(G)** A meandering spot which changes direction, darting about. **(H)** A single spot rotating around the surface. **(I)** A hemispherical band cyclically forming at one pole and terminating at the other. **(J-L)** A bifurcating system. Red contours represent high concentration.

Finally, a quantitative validation was performed by solving the diffusion equation on a rigid sphere as described by Equation 2.36.

$$\dot{a} = \Delta_s a \qquad (2.36)$$

An initial distribution following Equation 2.37 was applied, and the system was allowed to run towards a steady-state value. Figure 2.4 tracks the concentration of one point on the sphere as well as the exact solution (Equation 2.38), and we find agreement between the two.

$$a(\boldsymbol{x}, t = 0) = \frac{z}{R} \qquad (2.37)$$

$$a(\boldsymbol{x}, t) = \frac{z}{R} e^{-2t} \qquad (2.38)$$
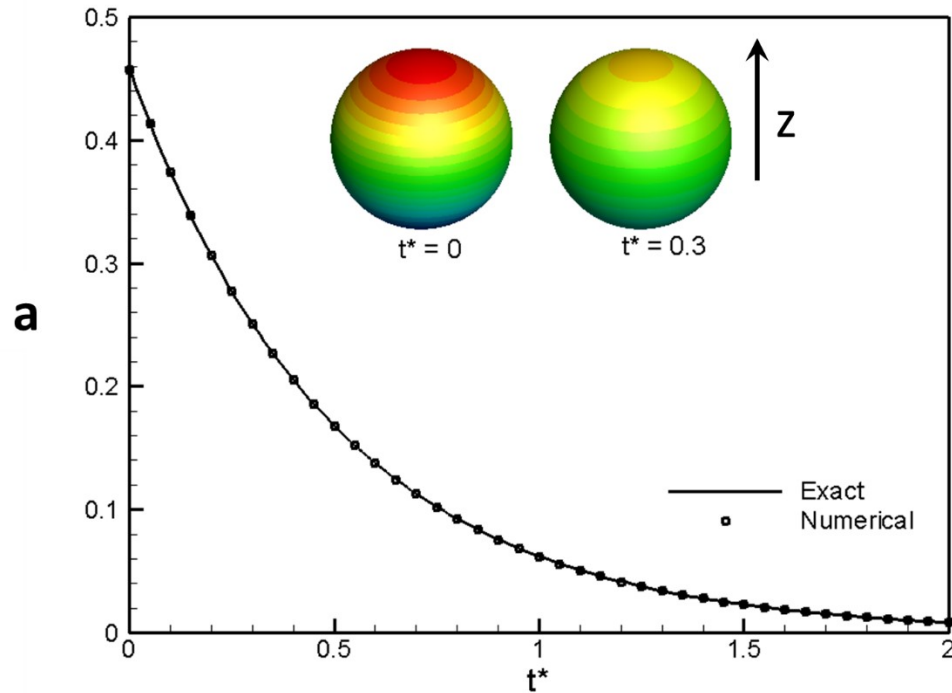
Figure 2.4: Solution of the diffusion equation on a rigid sphere using our surface finite element method. One point on the rigid sphere is tracked over time and compared to the exact solution.

2.4 Weak Adhesion Model

The amoeboid migration mode has been described as highly deformable with a diffuse, non-clustered, linear surface distribution [1]. And although experiments have shown adhesion to be dispensable for amoeboid migration in confined matrix geometries, adhesion is still a necessary cell function which mediates cell behavior, retention, invasion, and communication [50]. With this in mind, an amoeboid-specific adhesion model was sought to study new cell dynamics engendered by cell-matrix adhesive interactions.

Among the existing amoeboid migration works within the literature, attempts to study adhesion have produced a variety of models. Some consider adhesion to be negligible [8,13,29], while others assign an ad hoc, drag-based constraint which acts against migration [7,34]. Other models have set adhesive force to be proportional to cell adhesion complex density [30] or receptor-ligand concentrations and matrix elasticity [31]. Cirit *et al* modeled nascent and stable adhesions at the leading edge using ordinary differential equations [14]. Finally, discrete adhesion models which consider each bond as a deformable spring have been considered [11,32].

Perhaps the most prominent adhesion model comes from the work of Bell *et al* [4], and its derivatives [5,104], which utilizes thermodynamic calculus to model discrete adhesions as springs driven by reaction kinetics. The model is further strengthened with the addition of a stochastic Monte-Carlo method [16], which adds uncertainty to whether or not a bond will form or break. To begin, reaction rates relating the separation distance between the cell and obstacle surface are established as seen in Equation 2.39 and 2.40, where K_f is the forward reaction rate (bond creation) and K_r is the reverse reaction rate (bond retraction).

Furthermore, K_r^o and K_f^o are the unstressed reaction rates, σ is the spring constant, σ_{ts} is the transition-state spring constant, l and l_o are the current and reference ligand lengths, and $K_B T$ is the thermal energy based on the Boltzmann constant and absolute temperature.

$$K_r = K_r^o \exp\left[\frac{(\sigma - \sigma_{ts})(l - l_o)^2}{2K_B T}\right] \tag{2.39}$$

$$K_f = K_f^o \tag{2.40}$$

The probabilities of forward reaction (P_f) and reverse reaction (P_r) are subsequently established as described by Equations 2.41 and 2.42.

$$P_f = 1 - \exp\left(-K_f \Delta t\right) \tag{2.41}$$

$$P_r = 1 - \exp(-K_r \Delta t) \tag{2.42}$$

The Monte-Carlo method is then applied by considering the parameters N_f and N_r, random numbers selected between zero and unity. If $P_f > N_f$, a proposed bond will form, while if $P_r > N_r$, an existing bond will terminate [5,66]. Finally, for the bonds which have successfully formed, or for the bonds which have remained intact, an adhesive force based on Hookean spring physics may be defined.

$$f_a = \sigma(l - l_o) \tag{2.43}$$

2.5 Extracellular Matrix Geometry

As is the case present in the *in vivo* setting, cells often encounter a variety of obstacles in their extracellular environment, be it other cells, or the many matrix constituents which makeup body tissue. Here we discuss a framework for including rigid, non-moving obstacles into the fluid computational domain. Obstacle geometries are "immersed" into

the extracellular fluid, serving as the solid-phase component of the porous medium. A no-slip boundary condition is imposed on the surface of each obstacle. Because the continuous-forcing immersed boundary method is more well-behaved for elastic interfaces than rigid boundaries, however, a direct-forcing immersed boundary method is alternatively used. This Sharp-Interface Ghost Node method, which is introduced in detail in [107], allows for the implementation of arbitrarily-shaped obstacles whose surfaces do not necessarily coincide with the regular Eulerian mesh. Because of this freedom of geometry, additional considerations are required to enforce the no-slip condition on the obstacle surface.

As depicted in Figure 2.5, the Eulerian nodes determined to be inside of a closed obstacle are relabeled as solid nodes. The solid nodes immediately underneath the obstacle surface are further classified as ghost nodes (GN). A boundary intercept (BI) is then defined to be the point on the cell surface intersected by the surface normal vector passing through the ghost node. Finally, an image point (IP) is defined as the point outside of the cell running along the ghost node normal at a distance equivalent to the spacing between the ghost node and boundary intercept. The boundary intercept velocity $\boldsymbol{u}_{BI}$ is then set as the average value of the ghost node and image point velocities, $\boldsymbol{u}_{GN}$ and $\boldsymbol{u}_{IP}$, respectively. Enforcement of the no-slip condition requires setting $\boldsymbol{u}_{BI}$ to zero as seen in Equation 2.44.

$$\boldsymbol{u}_{BI} = \frac{(\boldsymbol{u}_{GN} + \boldsymbol{u}_{IP})}{2} = 0 \tag{2.44}$$

Finally, with knowledge of $\boldsymbol{u}_{IP}$ from a trilinear interpolation of the solved velocity field, the ghost node velocity can be determined as $\boldsymbol{u}_{GN} = -\boldsymbol{u}_{IP}$. This velocity value is enforced during solution, ensuring the no-slip condition on each obstacle surface is satisfied.

Obstacle validation has been performed in previous studies [107], where a rigid and nondeformable spherical obstacle was subjected to shear flow. Velocity data was compared to the analytical solution with excellent agreement. A more complex validation was performed by considering multiple deformable cells migrating through a bifurcating and merging rectangular channel, which produced good quantitative agreement.
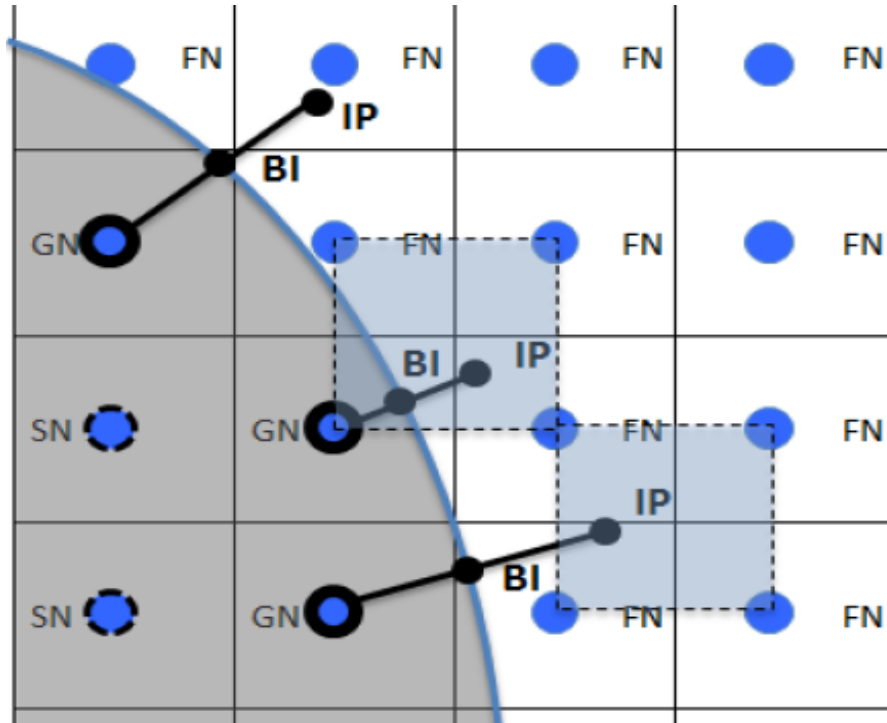
Figure 2.5: Illustration of the Ghost Node method. Ghost node velocities are valued such that a no-slip condition will occur at the boundary intercept.

2.6 Fluid-Structure Interaction

We consider both the cytosol in the cell interior and the extracellular fluid to be incompressible Newtonian fluids. Additionally, since viscous forces dominate at the microscale, the Reynold's number is taken as zero. We also assume the absence of any inertial terms, which leads to the Stoke's equations and incompressibility condition as seen

below, where $\boldsymbol{u}$ is the velocity field vector, p is the pressure field, and μ is the fluid viscosity. While a viscosity contrast can be applied between the cytosol and external fluid, we assume the fluid densities to be that of water.

$$\nabla \cdot \boldsymbol{u} = 0 \tag{2.45}$$

$$0 = -\nabla p + \nabla \cdot \mu[\nabla \boldsymbol{u} + \nabla \boldsymbol{u}^T] \tag{2.46}$$

Coupling between protrusive force, cell deformation, and fluid motion is done by considering the continuous-forcing immersed-boundary method [105], which allows for a single set of governing equations to be defined for the cell interior and exterior. To differentiate between the two fluid domains, an indicator function $I(\boldsymbol{x})$ is used as seen below in Equation 2.47, where μ_i is the cytosolic interior viscosity, and μ_o is the viscosity of the extracellular fluid.

$$\mu(\boldsymbol{x}, t) = \mu_o + (\mu_i - \mu_o)I(\boldsymbol{x}, t) \tag{2.47}$$

Naturally due to cell migration, the indicator function, which has a magnitude of either unity or zero, requires constant updating as the cell moves through the domain. This is accomplished by solving the Poisson equation seen below in Equation 2.48, where δ is the three-dimensional Dirac-delta function, x is a location in the fluid domain, x' is a point on the cell membrane, $\boldsymbol{n}$ is the outward normal vector, and S is again the cell surface.

$$\nabla^2 I(\boldsymbol{x}, t) = \nabla \cdot \int_S \delta(x - x')\boldsymbol{n} dS \tag{2.48}$$

The influence of the cell membrane on the fluid, which serves as the boundary between the fluid interior and exterior, is accounted for by introducing a source term into the governing equations as seen below, where $\boldsymbol{f}_e$ and $\boldsymbol{f}_b$ are the forces due to shear

deformation and area dilation, and bending, respectively. $\boldsymbol{f}_p$ is the membrane protrusion force due to pseudopod extension, and $\boldsymbol{f}_a$ is the membrane force resulting from adhesive bonding with the extracellular matrix.

$$0 = -\nabla p + \nabla \cdot \mu[\nabla \boldsymbol{u} + \nabla \boldsymbol{u}^T] + \int_S \left(\boldsymbol{f}_e + \boldsymbol{f}_b + \boldsymbol{f}_p + \boldsymbol{f}_a\right) \delta dS \qquad (2.49)$$

The delta function δ is zero except on the cell membrane, thus allowing the coupling between cell and fluid. Numerically, however, the delta function is approximated using a cosine function which smoothly spans over four Eulerian grid points in the fluid domain as seen by Equation 2.50, where h is the distance between Eulerian nodes in the fluid, x_i is an Eulerian node, and x'_i is Lagrangian node on the cell surface [106].

$$\delta(x - x') = \frac{1}{64h^3} \prod_{i=1}^{3} \left[1 + \cos\frac{\pi}{2h}(x_i - x'_i)\right], \qquad (2.50)$$

$$for \; |x_i - x'| \leq 2h, i = 1, 2, 3$$

$$= 0, otherwise$$

2.7 Flow Solver

Equation 2.49 is solved to obtain the fluid velocity field $\boldsymbol{u}(\boldsymbol{x})$ in the domain. The cell membrane velocity $\boldsymbol{u}_m$ can then be found via an interpolation integral coupled with the Dirac-delta function as seen in Equation 2.51, where $\boldsymbol{x}'$ is again a Lagrangian node on the cell surface, and $\boldsymbol{x}$ is a fluid node. Advection of the membrane nodes labeled as $\boldsymbol{x}_m$ can then be performed using $d\boldsymbol{x}_m/dt = \boldsymbol{u}_m$, thus resulting in the new cell position at the next timestep.

$$\boldsymbol{u}_m(\boldsymbol{x}') = \int_S \boldsymbol{u}(\boldsymbol{x})\delta(\boldsymbol{x} - \boldsymbol{x}')d\boldsymbol{x} \qquad (2.51)$$

The numerical technique for solving the computational domain which includes the cell membrane, internal and external fluid, and obstacle geometries is detailed in [107] but is briefly discussed here. A projection method is used for the solution of the unsteady Stokes equations. First, an advection-diffusion equation is solved, where the body-force terms representing the cell membrane, protrusion, and adhesion forces are treated explicitly using an Adams-Bashforth second-order method. Viscous terms are treated semi-implicitly using a Crank-Nicholson method. The pressure and velocity field within the Eulerian grid are organized in a staggered arrangement, with pressure at the center of an element, and velocity components at the edges. Spatial derivatives are evaluated using second-order finite differencing. The advection-diffusion equation is then solved using an alternating direction implicit (ADI) method. Next, a Poisson equation is solved to enforce the incompressibility constraint. An implicit solution is performed, while the periodic nature of the computational domain allows the use of a Fourier expansion for fast solutions.

2.8 Dimensionless Parameters and Scaling

Three dimensionless parameters are considered for a deformable amoeboid cell immersed in an unbounded fluid medium as described by Equations 2.52 through 2.54. λ is defined as the ratio between internal cell viscosity and external fluid viscosity. A range from $0.1 - 10.0$ is considered in Chapter 3 but kept at an equal ratio in Chapters 4 and 5. β is the ratio between local inhibitor diffusivity to local activator diffusivity, and is set in the range of $1.5 - 3.5$ in Chapter 3. In Chapters 4 and 5, β is kept exclusively at 3. Finally, α is defined to be the ratio of protrusive force to membrane elastic force, which is set in

the range of $1.0 - 10.0$ in Chapter 3, but limited to a maximum of 7.0 in Chapters 4 and 5. Here, R is the cell radius, and G_s is the membrane shear modulus.

$$\lambda = \frac{\mu_{cytosol}}{\mu_{fluid}} \tag{2.52}$$

$$\beta = \frac{D_3}{D_1} \tag{2.53}$$

$$\alpha = \frac{\xi}{G_s R} \tag{2.54}$$

When the cell is exposed to matrix geometries, two more dimensionless parameters are required as listed in Equations 2.55 and 2.56. ϕ is defined as the matrix porosity, or void space over the total space of the computational domain, and ranges from 0.54 for the densest matrix implemented to 1.00 for an unbounded domain. Finally, γ is the ratio of obstacle radius to the radius of the cell, and varies from $0.25 - 2.00$.

$$\phi = \frac{V_{void}}{V_{total}} \tag{2.55}$$

$$\gamma = \frac{R_{obstacle}}{R} \tag{2.56}$$

Length is scaled by the cell radius R, which for migrating amoeboid cells is in the range of $10 - 50 \ \mu m$ [27]. Time is scaled by $\frac{R^2}{D_1}$ and velocity by $\frac{D_1}{R}$. The shear modulus G_s is on the order of $10^{-6} \frac{N}{m}$ [90] while the activator and inhibitor diffusivities, D_1 and D_3 are on the order of $1 \frac{\mu m^2}{s}$, while the force per actin filament ξ ranges from $3 - 8 \ pN$ [91]. The strength of an integrin bond is approximately $40 \ pN$ [19].

Chapter 3

Pseudopod-Driven Swimming of an Amoeboid Cell in a Fluid Medium[1]

Amoeboid cells migrate through the use of pseudopods, or cylindrical extensions of the cell membrane which protrude, bifurcate, and retract in a dynamic fashion, resulting in a net displacement of the cell. This complex problem involves the interaction between the internal cytoplasm and extracellular fluid medium, coupled with bio-molecular reactions taking place on the cell surface in addition to extreme cell deformations. As has been recently observed experimentally, amoeboid cells are capable of swimming in a fluid medium completely absent of adhesive traction forces. In this work, an amoeboid cell is immersed inside an unbounded fluid domain where pseudopod-driven locomotion is activated. Results are compared to experiments both qualitatively and quantitatively. It is found that swimming behavior transitions from a random-like motion to a persistent unidirectional motion as cell deformability or protein diffusivity increase. This behavior is subsequently accompanied by an increase in swimming speed, and is due to the focusing of pseudopods on the cell anterior. Greater numbers of pseudopods are generated with increasing deformability and protein diffusivity, thereby amplifying this effect. Similar behavior is seen with regard to low viscosity ratio, while a nonlinear effect is seen in swimming speed as the viscosity ratio is increased. Results show a strong coupling between cell deformability, protein diffusivity, and fluid viscosity.

3.1 Introduction

As was described in Chapter 1, the amoeboid migration mode presents a highly deformable and dynamic migration mechanism through its use of pseudopods, or active actin-based membrane extensions which protrude, bifurcate, and retract over time, resulting in a net locomotion of the cell. A multitude of cells are known to migrate using the amoeboid mode, such as immune cells as they search and destroy foreign pathogens [22], epithelial cells during wound repair [24], embryonic positioning during reproduction [23], and even the metastasis of cancer cells [1]. The amoeba *Dictyostelium discoideum* (Dicty) also achieves motility through pseudopod-based mechanisms, and has served as an excellent case study due to its size and speed under experimental conditions.

In summary, pseudopod creation is a complex process beginning with the activation of external receptors due to outside stimuli. Signaling cascades then occur in which the nucleation of actin is started by the Arp2/3 complex, converting G-actin monomers into F-actin filaments which are crosslinked directly below the plasma membrane, resulting in a protrusive force which extends the cell forward. Contraction of the cell rear via the molecular motor Myosin II combined with the creation of adhesive bonds in the anterior, and rupture of bonds in the posterior creates a cyclic behavior which results in a net cell migration. For the case of a swimming cell, however, no adhesion is present. Furthermore, no explicit contractile mechanism is present within our model. Recent experimental observations have shown that amoeboid cells are capable of swimming while suspended in a fluid medium using only pseudopod-based modes, which extend near the cell anterior, bifurcate, migrate towards the rear, and finally retract [2-3,113]. These observations are validated by Purcell's Scallop Theorem, which states that non-reciprocal motions in time,

such as that caused by dynamic pseudopod activity, could generate a drag force sufficient for propulsion on the microscale [6].

Among the various properties of an amoeboid cell, deformability is known to play a critical role in regard to cell migration [2-3,9,27,113]. In fact, because metastatic cancer cells were observed to be much softer than their stiffer, benign counterparts [115], cell deformability has been proposed as a biomarker for metastatic potential [114]. Both fibroblasts and breast cancer cells which underwent cell softening were seen to exhibit higher migration speeds and an increased proliferation of malignant cells [116]. In addition to the membrane elasticity, the rheology of the cell cytoplasm and extracellular fluid are two major parameters which control cell deformation. Streaming flow occurs within a growing pseudopod as it extends outward and encounters drag imposed by the extracellular fluid [119-120]. A protruding pseudopod must also overcome membrane tension, after which the resulting tension and membrane curvature can affect actin-associated proteins like Ras [117-118], thereby generating a coupled feedback loop affecting cell motility.

While the field of amoeboid motility has seen significant modeling advancement recently, a full three-dimensional model still remains a challenge [121]. Numerous models consider only the biochemical aspect of cell migration, but not fluid flow or cellular deformation [122-123]. Other models which do consider cell deformation are limited to two-dimensions [8,124-127], while further models are limited to relatively simple cell shapes [127-129]. Several noteworthy studies are now discussed. Vanderlei *et al* [130] constructed a two-dimensional motile cell model using the immersed boundary method, resolving cell deformation, internal and external fluid flows, and a cell-volume reaction-diffusion system, thus allowing advection-diffusion of biochemical species within the cell

as it migrates and deforms. Bottino and Fauci [131] also modeled a two-dimensional, deformable and motile amoeboid cell using an immersed boundary method, where the cytoskeleton was modeled as a network of dynamic springs immersed in fluid. In addition to protrusive and contractile forces, cycles of attachment and detachment while crawling over a substrate were seen. Elliott *et al* [7] constructed a three-dimensional model of a deforming cell with bifurcating pseudopods. Similar to other models [8,9,125-126,128-129], however, no modeling of cytoplasm or extracellular fluid was done, which as discussed, is an important factor in determining cell motility. Farutin *et al* [108] and Wu *et al* [132] both conceived of a deformable cell driven via an axisymmetric oscillating force. But, while internal and external fluids are considered, the complex dynamic nature of pseudopods are not captured, nor is the random movement that would be expected for amoeboid motion. Najem and Grant [133] simulated the migration of neutrophils responding to external cues in three-dimensions using a phase-field approach, but ignored the presence of fluids. Finally, Moure and Gomez [10-11] used a phase-field approach to simulate two- and three-dimensional amoeboid motility through obstacle fields and fibrous networks. Cytosolic fluid and rheology, acto-myosin dynamics, and membrane signaling dynamics using activator reaction-diffusion equations were all considered.

3.2 Results

3.2.1 General Swimming Behavior

Figure 3.1 displays a sequence of a swimming amoeboid cell as it migrates through the fluid medium over time. Qualitative comparisons are made using references [2-3,9,27,113,135,157-158], and good agreement is seen between predicted amoeboid shapes and experimental images of migrating cells. Since the fluid is coupled to the cell, *ad hoc*

models for the drag are not needed as has been done in earlier studies [7-8,29,125-126,128,]. The effect of fluid drag on the cell is directly resolved. Furthermore, the nonlinear membrane model used is a significant improvement over other models, and as a result, simulations can be run for long durations, even for cells which generate complex and highly deformed shapes. Several interesting types of behavior are witnessed within the sequence. *de novo* pseudopod formation, bifurcation, pseudopod meandering, and retraction are all seen in each simulation, contributing to the highly dynamic behavior seen as the cell migrates. Looking at Figure 3.1A in particular, the cell is initialized as a sphere with uniform activator and inhibitor concentrations set. Random noise generated within the reaction-diffusion system then causes perturbations which develop into a single high-concentration activator instability. Because activator concentration is directly linked to protrusive force, a *de novo* pseudopod begins to emerge as the membrane extends outwards (Figure 3.1A (a)). As the pseudopod protrudes further into the extracellular fluid, a bifurcation begins to take place, where the parent pseudopod splits into two daughter pseudopods as seen in (b) and (c). Responding to the protrusive force directions imparted to the pseudopods, a meandering behavior is seen in (c) and (d), which further propels the cell forward. Another bifurcation is seen in (e) which then develops into the form shown in (f). In (g), the decay of a pseudopod is shown, where the membrane protrusion still remains after the high-concentration activator has diminished. This causes a fundamental shift in pseudopod direction, as seen in (h) where a new forward direction is maintained by further pseudopod bifurcations. In (i) through (o), another characteristic behavior is seen in which pseudopods focus toward the front of the cell, providing a consistent protrusive force and allowing the cell to maintain a nearly persistent direction. This directional motion

is then interrupted in (o) by an errant pseudopod which causes a turn as seen by (p) and (q).

As shown in Figure 3.1, the active nature of pseudopod dynamics causes significant three-dimensional movement and deformation.
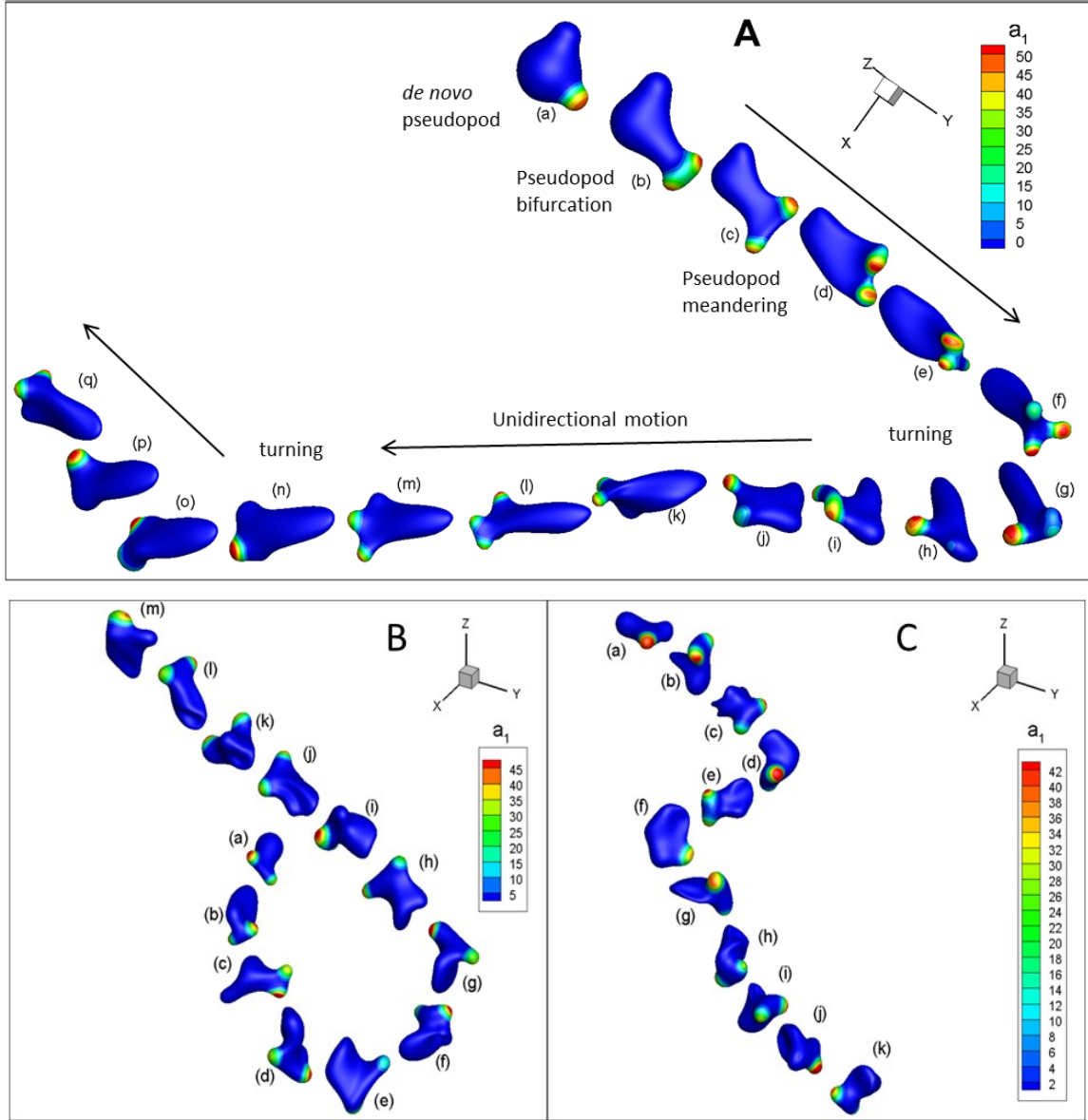
Figure 3.1: Sequence of images of a swimming amoeba as predicted by our simulations. **(A)** $\alpha = 5$, $\beta = 3$, $\lambda = 1$. Direction of cell motion is from (a) to (q). Color contours represent the activator concentration. **(B)** $\alpha = 3$, $\beta = 2.5$, $\lambda = 1$. **(C)** $\alpha = 2$, $\beta = 2$, $\lambda = 0.1$. Reprinted from [148] with the permission of AIP Publishing.
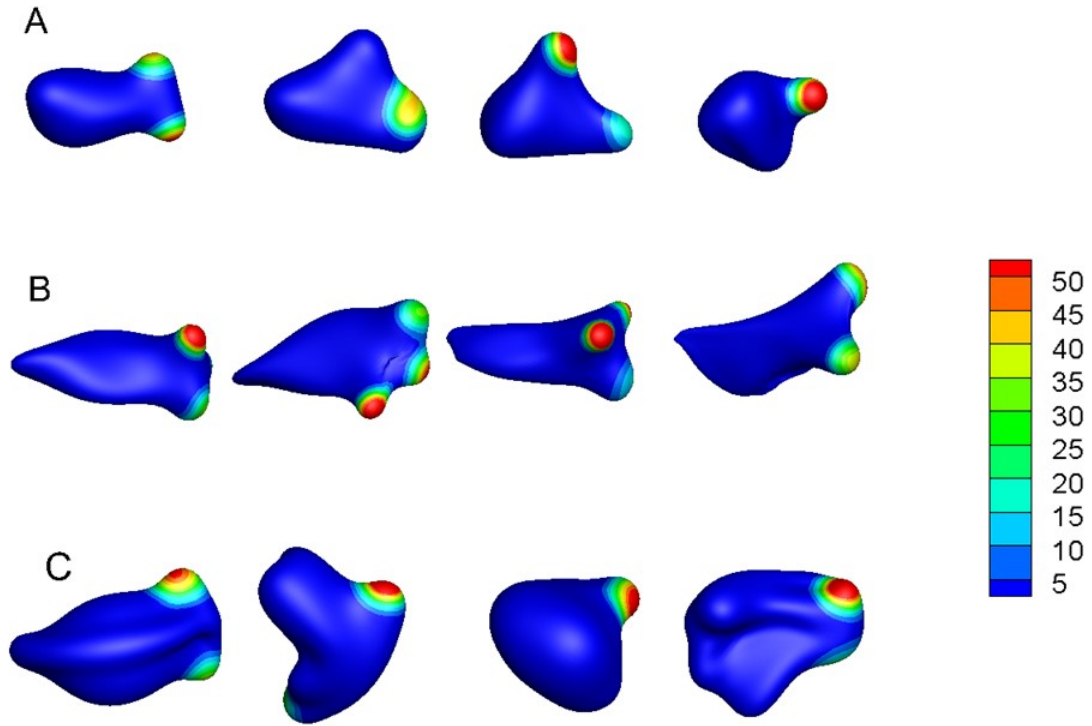
Figure 3.2: Instantaneous cell shapes at reduced membrane stiffness. **(A)** $\alpha = 1.5$, $\beta = 3$, $\lambda = 1$. **(B)** $\alpha = 5$, $\beta = 3$, $\lambda = 0.1$. **(C)** $\alpha = 5$, $\beta = 3$, $\lambda = 10$. Swimming direction is from left to right. Color contour represents activator concentration. Reprinted from [148] with the permission of AIP Publishing.

Parameter studies have revealed the large dependence that membrane stiffness, protrusive force, protein diffusivity, and fluid viscosity have on cell shape and dynamics. Figure 3.2 illustrates the differences in cell shape for several parameters. For the parameter α, for which larger values correspond to reduced membrane stiffness, cells generally adopt a more spherical shape when $\alpha < 3$. For values of 3 or greater, however, elongated cell shapes are observed as seen by Figure 3.1A (k)-(n). Similar behavior is seen when the diffusivity ratio β is varied. When $\beta > 2.5$, elongated cell shapes are again seen, while for

smaller values of β, rounded shapes can be found. Comparable observations can be made with the viscosity ratio λ, where elongated cell shapes and generally spherical shapes are seen for $\lambda < 1$ and $\lambda \geq 1$, respectively, as seen in Figure 3.2 B and C. Pseudopods themselves are noted to be more slender and longer for cases with softer membranes and higher diffusivity ratios, while they are seen as shorter and wider for stiffer membranes and lower diffusivity ratios. For small α, the protrusive force is not significant enough to overcome membrane tension, thus resulting in mostly spherical shapes (Figure 3.2A). A general roundness is also seen for high values of viscosity ratio λ, where viscous dissipation and membrane tension act to counter the protrusive force. Pseudopod remnants can also be seen in Figure 3.2C for the case of high viscosity ratio, where larger shape recovery times slow down the rate of pseudopod retraction even though activator concentrations have decayed.

3.2.2   Instantaneous Velocity and Cell Trajectory

Because our model provides no bias in the stochastic noise fed into the activator equation, external cues are not present, and therefore do not affect cell dynamics. As a result, pseudopod generation, bifurcation, meandering, and retraction occur randomly and as dictated by key cell properties. We have found, however, that under certain parameter ranges, cell migration behaviors can transition from a random-walk like behavior to a more persistent swimming migration. Figure 3.3A illustrates several cell centroid trajectories of amoeboid cells over time and with various cell parameters to show this effect. Cells categorized by lower values of α and β, and higher values of λ (color trajectories) are seen to travel shorter distances characterized by sharp and frequent turns. Changes in direction were discussed previously, and are caused by pseudopod meandering and retractions. On

the opposite spectrum of parameters, higher values of α and β, and lower values of λ (black trajectories) are noticeably longer in length and have fewer and smaller magnitude directional changes, resulting in a persistent migration.

Instantaneous cell centroid velocities V_C are shown in Figure 3.3B for several values of α and β. The randomness in cell migration can be observed from fluctuations in the velocity curves, where larger-scale changes in velocity are due to directional changes of the whole cell, while smaller maxima and minima occur as a result of the motions from pseudopod dynamics. Velocity magnitudes are also seen to vary, with higher speeds seen for larger α and β with the reverse true for smaller values. Further analysis reveals larger values of β show smaller-magnitude fluctuations in velocity, demonstrating a more persistent directional motion characterized by fewer deviations from pseudopod dynamics. For the viscosity ratio, similar effects are noted. Larger values of λ show higher degrees of fluctuations leading to smaller velocities, while smaller λ results in reduced fluctuations and higher velocities brought about by persistent motion.
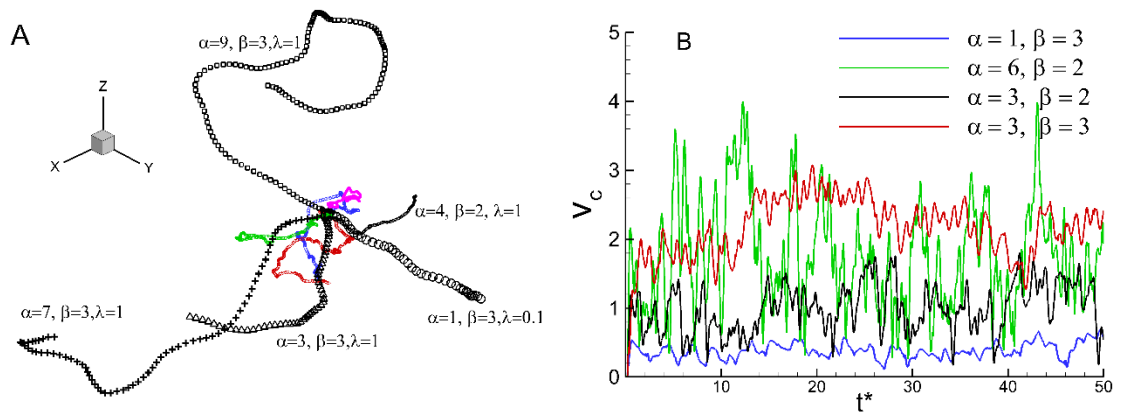
Figure 3.3: **(A)** Sample cell trajectories. Parameter values are noted for the trajectories shown using black symbols. For green, blue, and red, $\alpha = 6, 7,$ and 8, respectively. $\beta = 2$ and $\lambda = 1$. For magenta, $\alpha = 1, \beta = 3, \lambda = 10$. **(B)** Instantaneous velocity of cell centroid.

A question arises of whether the swimming migration seen in our simulations is characterized as diffusive or ballistic (super diffusive). Often the subject of entire works in the literature, it has been shown that ballistic motion can occur over shorter time scales on the order of persistence time, while longer times can be described as diffusive after encountering the caprices of the cell's migration [134-135]. Mean Squared Displacement (MSD) was computed and is displayed in Figure 3.4 for several cell trajectories. At larger times, the MSD appear to exhibit a linear trend, indicating a diffusive behavior, though a full determination would require more extensive simulations which were considered as beyond the scope of this work.
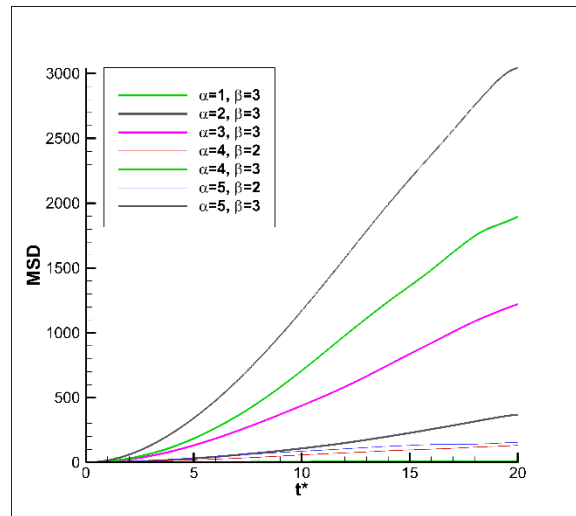
Figure 3.4: Mean Squared Displacement (MSD) for several parameter ranges. Reprinted from [148] with the permission of AIP Publishing.

3.2.3 Flow Field

Several snapshots showing instantaneous velocity fields for various cell parameters and cell dynamics are illustrated in Figure 3.5. Simulations reveal transient and dynamic fluid velocity fields both inside and outside of the cell. During a pseudopod extension event, cytoplasmic streaming into the growing pseudopod is observed. On the exterior of the

pseudopod, fluid is seen to be drawn towards the growing pseudopod and pushed away. The reverse is true during a retraction event, where exterior flow follows the receding pseudopod, while a streaming flow occurs towards the main cell body in the interior. Velocity magnitudes are seen as larger when near a pseudopod due to the actively protruding membrane, while reduced magnitudes occur after high-concentration instabilities have decayed due to passive effects. Figure 3.5 also shows complex and unsteady flow patterns which result from dynamic cell and pseudopod motion.
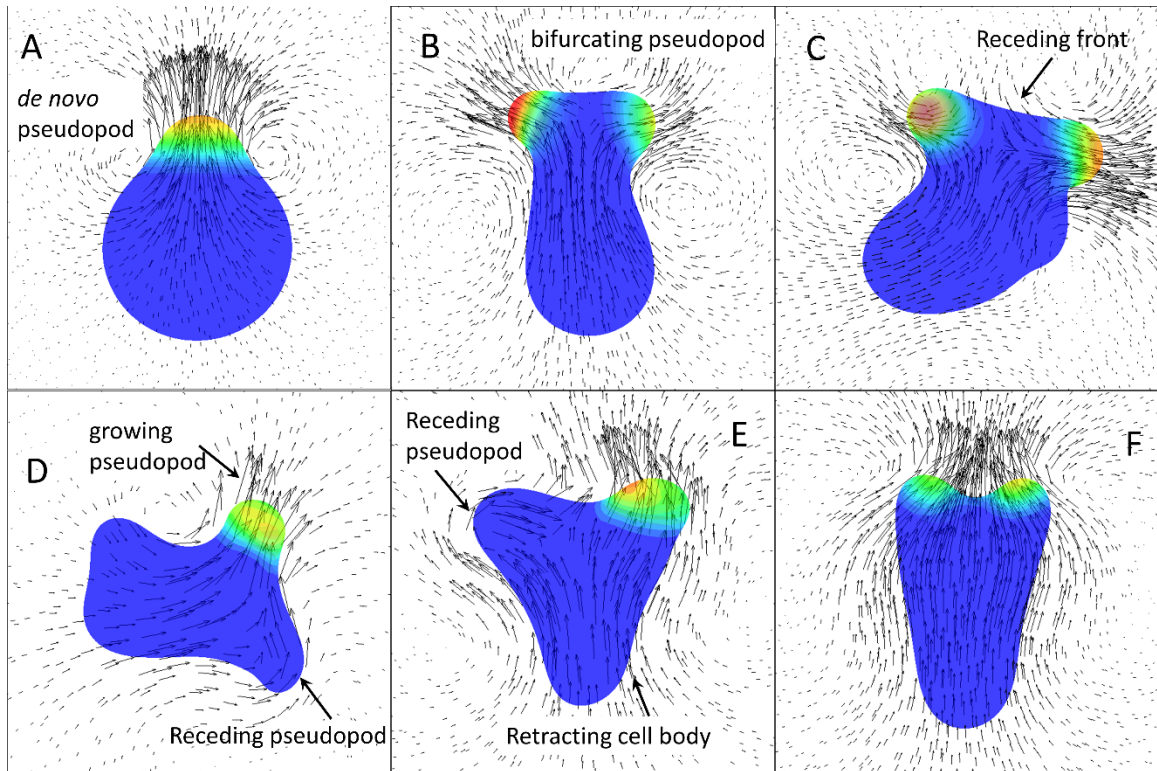
Figure 3.5: Instantaneous fluid velocity vectors drawn in a plane passing through the cell centroid and superimposed with a two-dimensional cell shape. Colors represent activator concentration. Reprinted from [148] with the permission of AIP Publishing.

Within the literature are discussions regarding two paradigms of cell swimming: pushers and pullers. Pushers are described as generating a fluid repulsion along the directional axis of swimming, and a fluid attraction along the sides of the cell. Pullers are the exact opposite, pulling in fluid along the axis of swimming, and repelling fluid away from the sides. Other unclassified flow patterns, which can be considered a hybrid of pusher and puller motion can also exist inside the flow field. In references [108,132], deformable vesicles were studied using spherical harmonics for protrusive and contractile force. Out of the four strokes of the displacement cycle, one showed pusher motion, and another showed puller motion. The remaining strokes showed a hybrid type motion encompassing aspects of both modes. Figure 3.6 displays these some of the different classifications observed within our simulations. Pusher migration, as seen in Figure 3.6A, was only noted to occur during the initial transient period when opposing pseudopods were forming, and only for cases of high α. Puller motion, on the other hand, and which is seen in Figure 3.6B and C, was noted to occur more frequently and regardless of α, but with smaller values of β. In most cases, though, fluid patterns cannot be described by pushers or pullers. Figure 3.6D-F illustrate several examples where cell elongation and pseudopod focusing on the cell anterior prevent other modes from occurring.

Pusher and puller classification were also performed qualitatively and quantitatively to analyze beyond an instantaneous cell state. For each case, flow fields were examined over the entire solution time, after which conclusions were made. Additionally, classifications were determined through calculation of the stresslet tensor $\boldsymbol{S}$, of which the general form is described by Equation 3.1 below [136].
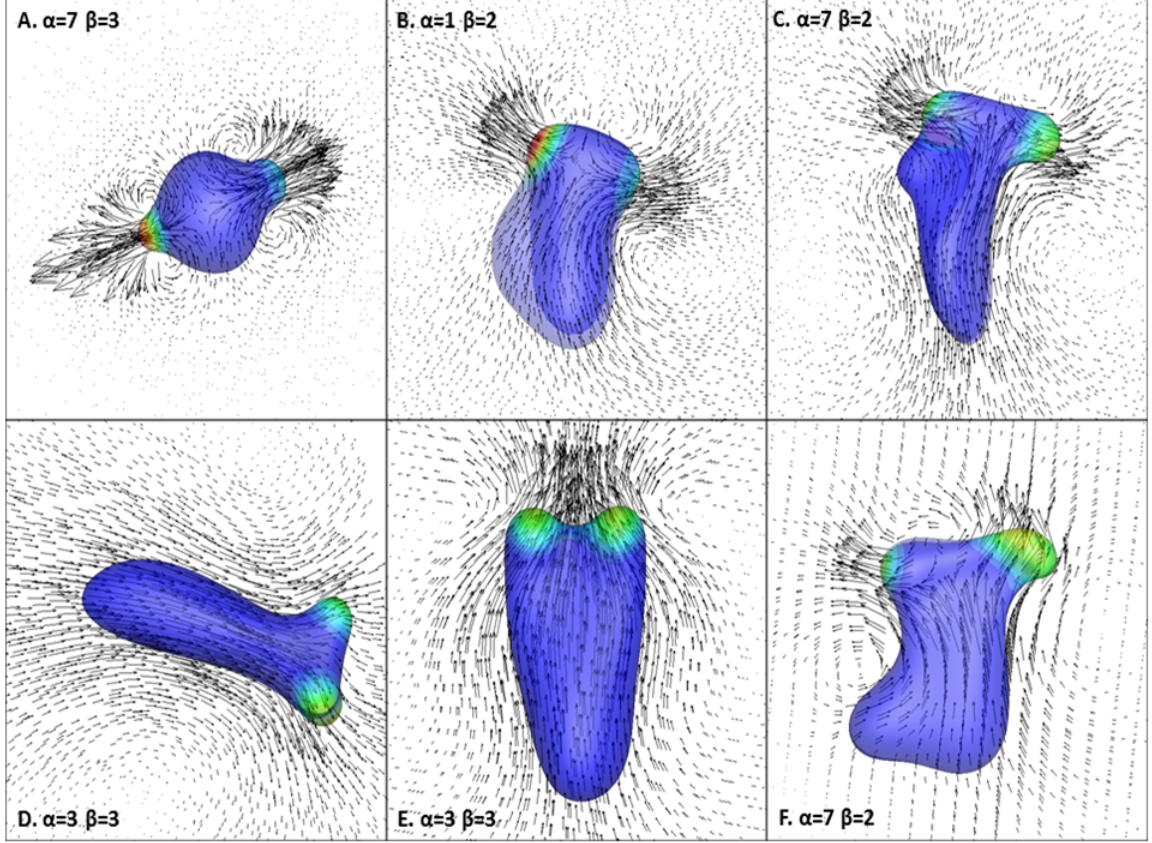
Figure 3.6: Instantaneous fluid velocity vectors. **(A)** pusher-like motion as observed during initial transience. **(B-C)** Puller-type motion. **(D-F)** Neither pusher-like or puller-like motion. Color contours represent activator concentration. Reprinted from [148] with the permission of AIP Publishing.

$$S_{ij} = \oint_S \left[\frac{1}{2}(x_j \tau_{ik} + x_i \tau_{jk})n_k - \frac{1}{3}(x_k \tau_{kl} n_l)\delta_{ij} - \mu(u_i n_j + u_j n_i) \right] dA \qquad (3.1)$$

For a three-dimensional cell which experiences extreme deformation and dynamic pseudopod motion, however, the stresslet tensor has constantly changing non-zero terms, making it difficult to interpret. Assuming the problem of an axisymmetric swimmer moving along the $\boldsymbol{e}_z$ direction, however, allows the stresslet to be simplified to a scalar Ψ as seen below.

$$\mathbf{S} = \Psi \left(\boldsymbol{e}_z \boldsymbol{e}_z - \frac{1}{3} \boldsymbol{I} \right) \tag{3.2}$$

During initial transient periods, our simulated cells can be approximately modeled as being axisymmetric, and therefore Ψ can be computed. For the case of a pusher, $\Psi = -15{,}500$, while for a pusher, $\Psi = 190$. The signs of the pusher and puller stresslet are negative and positive, respectively, as is the case in the literature [137].

3.2.4 Pseudopod Dynamics

The dynamic nature of Turing instabilities are used to evolve membrane protein concentration, which is then linked to protrusive force. Experiments have revealed high concentrations of proteins such as Ras or F-actin at the site of a pseudopod [125,159]. This effect is modeled using Turing instabilities, which result in the generation, migration, and bifurcation of activator patches on the cell surface. Corresponding pseudopod dynamics result in a paddle-like, non-reciprocal motion which agrees with Purcell's theorem [6]. Furthermore, pseudopod bifurcation, or "tip-splitting," is perceived as the key event in amoeboid swimming motility [135,159].

As inferred from Figures 3.1 and 3.2, cell shape is heavily dependent upon pseudopod dynamics, which themselves are dependent on the membrane stiffness, protein diffusivity, and fluid viscosity. For larger values of α and β, and smaller values of λ, pseudopods were shown to focus near the front of the cell, resulting in an elongated and persistent cell motion. On the other hand, for smaller values of α and β, and larger values of λ, cells were seen as mostly spherical while pseudopods showed no preference in direction. Elongation of the cell was seen to occur as a direct result of oriented pseudopods. Additionally, for larger values of α and β, and smaller values of λ, a maximum number of pseudopods,

around $3 - 4$, were seen to exist in simulations. Only $1 - 2$ pseudopods were seen for the alternate parameter ranges.

In order to quantify the directional persistence observed in cells, directionality was quantified by plotting the pseudopod tip normals over time using the spherical coordinates θ and ϕ as seen in Figure 3.7. For stiff cells with lower values of α (Figure 3.7A), or with values of $\lambda > 1$ (Figure 3.7D), pseudopod tips are seen as uniformly distributed across the entire spherical domain, indicating generation or positioning of pseudopods in random directions. Scattered pseudopods are also noted to occur for smaller values of β as seen in Figure 3.7A. On the other hand, for softer cells with higher values of α (Figure 3.7C) or values of $\lambda < 1$ (Figure 3.7E), pseudopods are seen to form in a narrow grouping of points, indicating that pseudopods are focused or generated in the same direction. A tighter grouping of pseudopods is also seen as β is increased. One would expect an activator-inhibitor system with random noise to generate random activator patches, yet our simulations have predicted a persistent unidirectional motion is possible in the absence of an external cue or bias on the activator-inhibitor system. This behavior was also observed in experiments [113,134-135], where it was also found that cells were persistent because pseudopods maintained direction. This behavior is a direct result of pseudopod dynamics, which in turn depend on membrane deformability, protein diffusivity, and fluid viscosity.

Looking at Figure 3.7F, the primary mechanism for persistent cell migration by focused pseudopods can be observed. Starting with the cell on the right, a bifurcation occurs, after which two daughter pseudopods migrate outwards and away from each other, creating a concavity in the cell membrane. Soon after, the pseudopods begin to move back inwards towards the point of bifurcation. One pseudopod will then retract, leaving the remaining

pseudopod free to bifurcate in a similar direction, thus preserving the overall directionality of the cell. Finally, the inherent three-dimensionality of the swimming amoeboid cell can be seen in Figure 3.7G, where pseudopod bifurcations are shown to occur in the plane normal to the plane of the previous bifurcation. This aspect of migration could not be inferred from two-dimensional experimental images. This behavior also seems to be a three-dimensional equivalent of the progression in Figure 3.7F, which is noted to occur continuously until persistence is broken by errant pseudopod dynamics.
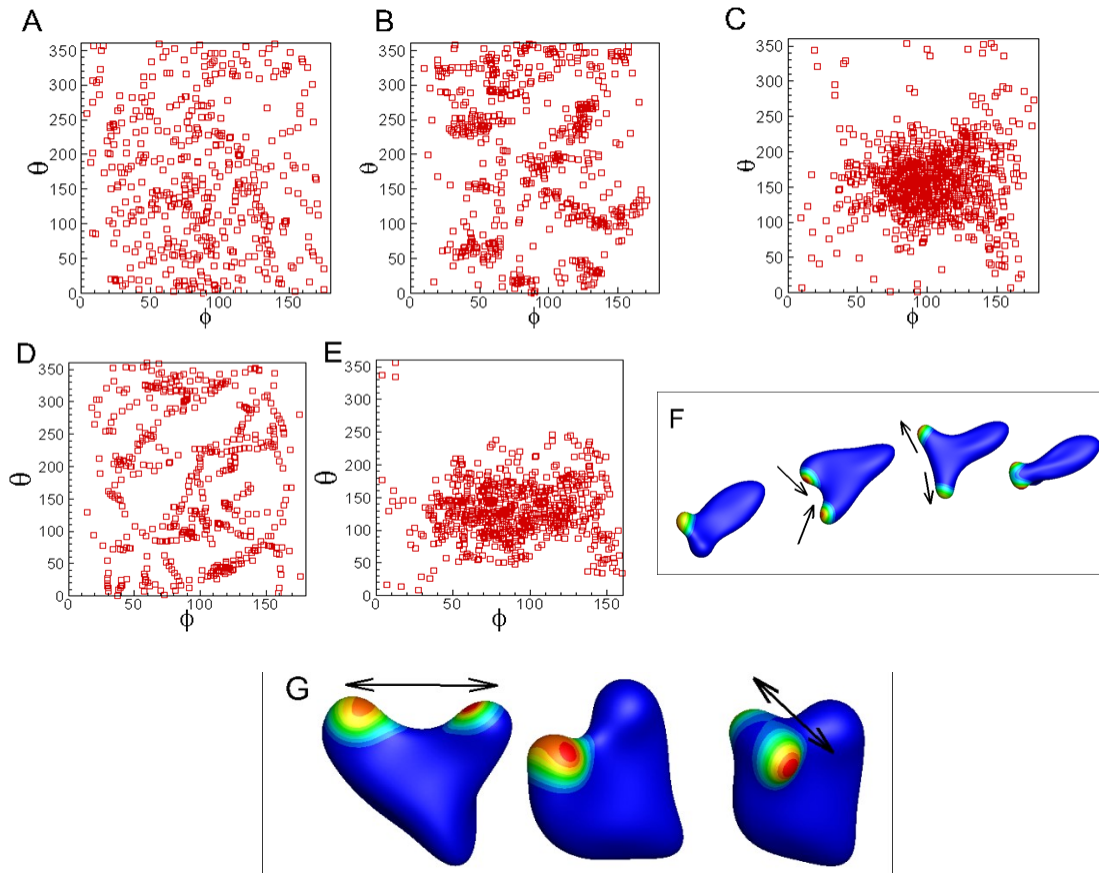
Figure 3.7: Pseudopod directionality is quantified by the angular position of pseudopod tips using spherical coordinates θ (0 to 2π) and ϕ (0 to π). **(A)** $\alpha = 1$, $\beta = 2$, $\lambda = 1$. **(B)** $\alpha = 1$, $\beta = 3$, $\lambda = 1$. **(C)** $\alpha = 6$, $\beta = 3$, $\lambda = 1$. **(D)** $\alpha = 2$, $\beta = 3$, $\lambda = 10$. **(E)** $\alpha = 2$, $\beta = 3$, $\lambda = 0.1$. Data points are separated by 0.05 dimensionless time. **(F)** Mechanism of focused directionality of pseudopods. **(G)** Pseudopods bifurcate at angles perpendicular to previous bifurcations. Color contours represent activator concentration. Reprinted from [148] with the permission of AIP Publishing.

Quantification of pseudopod statistics was performed in Figure 3.8, where the average and maximum number of pseudopods present are shown in addition to the average pseudopod lifetime. Dependence on α, β, and λ is presented. The maximum number of pseudopods ranges from $2-4$, while pseudopod averages are in the range $1.0-2.5$. Similar trends are noted to occur over each parameter range. The average number of pseudopods present on a cell at any given time is seen to increase with larger α and β, and with decreasing λ. This corresponds to a cell becoming more deformable or as the diffusivity ratio increases. For stiffer cells, no more than two pseudopods are seen at a time, while the number increases to three or four as the cell becomes softer. Similarly, for low values of the diffusivity ratio, a maximum of two pseudopods is seen, while three or four pseudopods can be observed with higher diffusivity ratio.

In Figure 3.8, the average pseudopod lifetime is seen to depend on α and β, but not for λ. Lifetimes are also noted to decrease with increasing α, which we attribute to a greater propensity to bifurcate when exposed to higher levels of deformability. Lower lifetimes also correspond to higher frequencies of pseudopod tip-splitting as α is increased. In this case, an existing pseudopod can bifurcate before the alternate pseudopod retracts, resulting in higher levels of bifurcation frequency and greater amounts of membrane extensions present at a given point in time. Pseudopod lifetimes are also seen to increase with increasing β, which is caused by the activator concentration increasing faster than the inhibitor concentration, thus allowing Turing instabilities, and subsequently, pseudopods to survive longer.
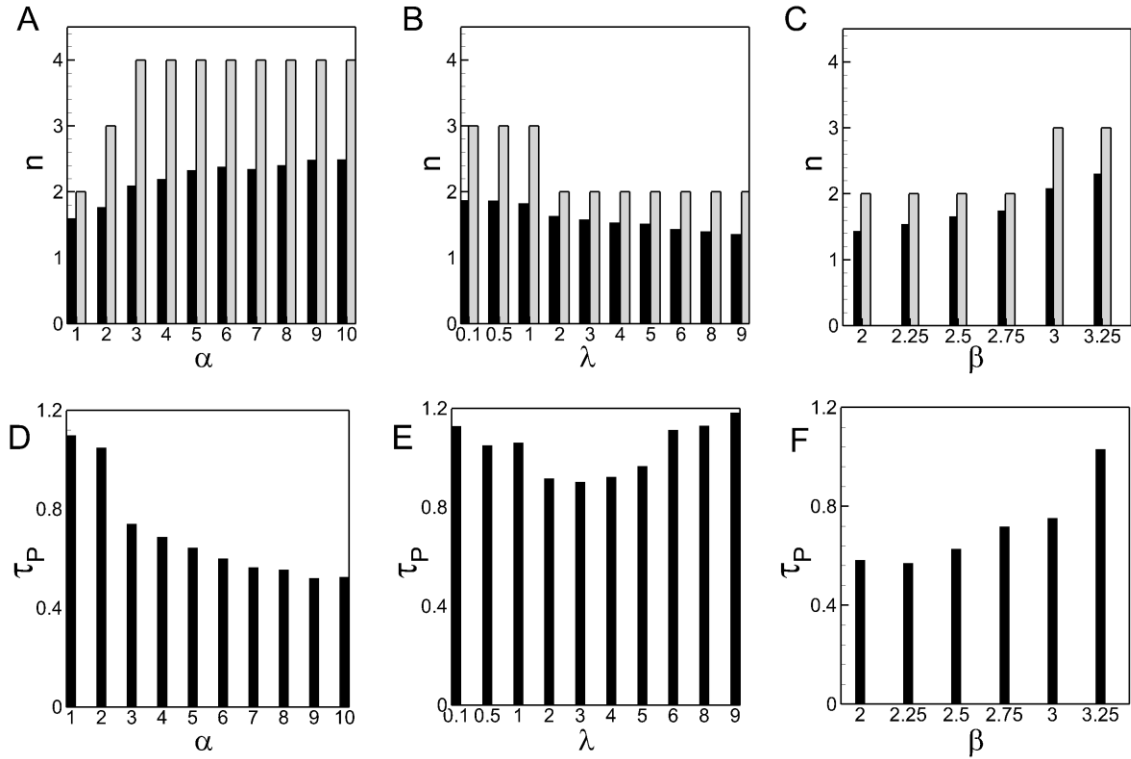
Figure 3.8: Pseudopod dynamics. **(A-C)** show average (black bars) and maximum (grey bars) number of pseudopods as functions of α, λ, and β, respectively. **(D-F)** show average lifetime (scaled by R^2/D_1) of a pseudopod. Reprinted from [148] with the permission of AIP Publishing.

3.2.5 Swimming Speed

As inferred by the trajectory and velocity plots in Figure 3.3, pseudopod dynamics play a large role in determining the swimming speed of an amoeboid cell. Speed is likewise linked to the mechanical properties of the cell in addition to the protein diffusivity controlling the activator-inhibitor system. Figure 3.9 plots the time-averaged speed $\overline{V_c}$ (scaled by D_1/R) as a function of α for two different values of the diffusivity ratio. Average swimming speed is seen to increase with increasing α, which is expected due to larger protrusive forces acting on the cell. However, a sizable difference in speed is seen between $\beta = 2$ and $\beta = 3$. Earlier discussions are again referenced to explain this behavior. In

Figure 3.7A-C, pseudopod tips are shown to focus in a particular direction as α and β increase, thereby summing the individual protrusive forces of each pseudopod and resulting in a higher cell speed. When β is low, however, pseudopods do not focus, and therefore produce a random-type motion characterized by lower swimming speed. Similarly, in Figure 3.8, a greater number of pseudopods is produced with higher value of β. Coupled with a pseudopod focusing, more pseudopods result in a higher protrusive force, and therefore a higher swimming speed.

Figure 3.9 also shows an increase in the slope of $\overline{V_c}$ as the diffusivity ratio is increased. As a result, cell deformation is seen to have a greater effect on cell speed for larger values of the inhibitor diffusivity. Likewise, inhibitor diffusivity provides greater influence as the cell becomes more deformable. This statement details the strong coupling between cell deformability and surface protein diffusion, which in turn both affect pseudopod dynamics and cell speed. The average speed $\overline{V_c}$ is again plotted against diffusivity ratio and viscosity ratio for several values of α in Figure 3.10. In Figure 3.10A, the swimming speed is noted to be almost constant in the range $\beta < 2.25$. As β increases past this amount, however, the swimming speed begins to increase substantially. This trend is again caused by pseudopod dynamics detailed in Figures 3.7 and 3.8, which show both an increase in the number of pseudopods with β as well as a higher degree of focusing. Pseudopod lifetimes are also noted to increase with β, thus allowing for longer usages of protrusive force. Taken together, these properties lead to higher protrusive force and higher swimming speed as a result.
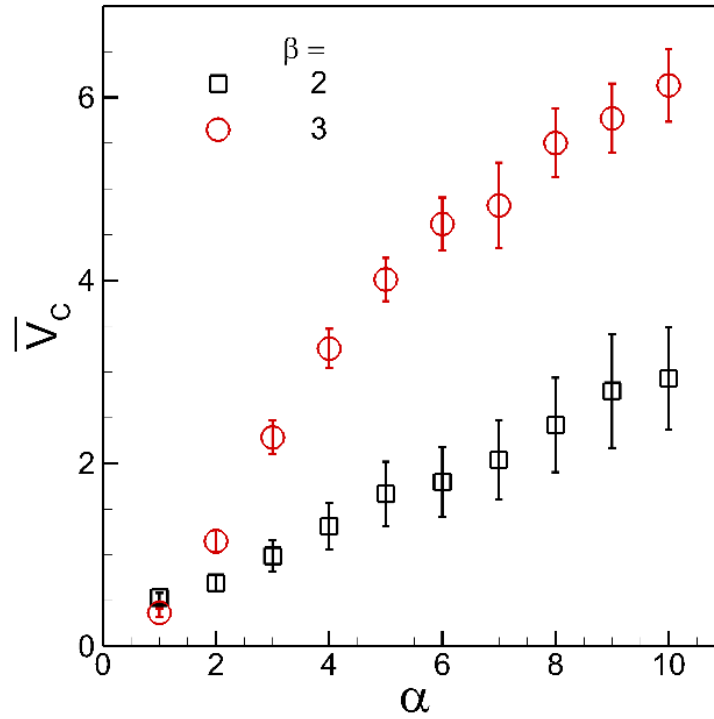
Figure 3.9: Average cell speed as a function of α. Error bars represent one standard deviation. Reprinted from [148] with the permission of AIP Publishing.

The influence of cytoplasmic to extracellular viscosity on the average swimming speed is seen in Figure 3.10B for several values of α. Two distinct trends, which are separated by a minimum, are immediately discernible. When $\lambda < 1$, an inverse correlation between swimming speed and viscosity ratio exists: As λ increases, $\overline{V}_c$ is seen to decrease. When minimum swimming speed is reached at $\lambda = 3$, the viscosity ratio and swimming speed become positively correlated, where $\overline{V}_c$ increases with λ. In both regimes, an explanation can be found by looking at the pseudopod dynamics. As the viscosity ratio decreases, the maximum number of pseudopods is seen to increase (Figure 3.8B). Furthermore, pseudopods are found to focus on the cell anterior as seen by Figure 3.7E. Combined with larger pseudopod lifetimes, these dynamics give the cell a higher protrusive force focused

in the same direction for a longer period of time, thus resulting in higher swimming speeds. The case of higher viscosity ratio can be similarly argued. While the number of average pseudopods is seen to decrease with increasing λ and pseudopods are shown to form uniformly in all directions, pseudopod lifetimes are seen to increase, thus contributing to the slower increase seen for large λ.
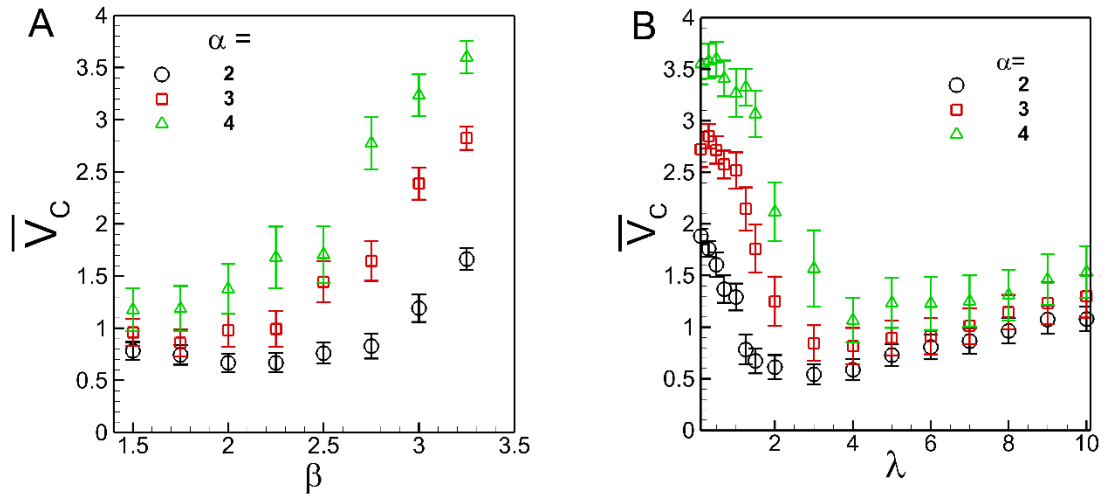
Figure 3.10: Time averaged cell speed as a function of **(A)** diffusivity ratio β and **(B)** viscosity ratio λ for various values of α. Reprinted from [148] with the permission of AIP Publishing.

Our data on the average swimming speed is quantitatively comparable to that of experiments. Although most experimental works deal with cell crawling on a substrate, some such as [113] have reported data on both migration mechanisms. To convert to dimensional quantities, we use a cell size of $20\ \mu m$, and an activator diffusivity of $1\ \mu m^2/s$. Speed is then scaled by D_1/R, which results in a typical swimming speed of $3-9\ \mu m^2/min$ for a dimensionless range of $\overline{V}_c \approx 1-3$, considering moderate cell parameter values. This range agrees well with experiments showing $3\ \mu m^2/min$ for swimming cells, and $7-12\ \mu m^2/min$ for crawling cells [113,134]. Additionally, we also

look at the average pseudopod tip velocity, which is in the range of $15 - 21 \ \mu m^2/min$, and has good agreement with the experimental value of $18 \ \mu m^2/min$ [113].

Other experimental studies have used wild-type and mutant cells to study amoeboid motility. In [159], wild-type amoeba were observed to have a more elongated shape and a higher migration speed ($\sim 22 \ \mu m/min$), while nearly spherical mutant cells moved much slower at ($\sim 3 \ \mu m/min$). We link these observations to membrane stiffness, protein diffusivity, and cytoplasmic viscosity. Cells are seen to decrease speed and become rounder as membrane stiffness increases. Our simulated speeds go from $1.5 - 18 \ \mu m/min$ as α ranges from 1 to 10. Variations in cell speed therefore agree well with experimental data for wild-type and mutant cells. Instantaneous velocity plots also show similarities with corresponding plots in Figure 3.3B.

3.3 Summary

In conclusion, results were presented for a three-dimensional model of a pseudopod-driven amoeboid cell swimming through a fluid medium. The effect of membrane deformability, surface protein diffusivity, and cytoplasmic to extracellular fluid viscosity was investigated for cell dynamics, fluid field velocity, pseudopod statistics, and cell swimming speeds. A transition from a slow-moving cell characterized by randomly generated pseudopods to a persistent cell with higher speed was predicted with increasing cell deformability and protein diffusivity, and decreasing viscosity ratio. Persistent swimming was seen without any explicit bias within the activator-inhibitor system, and occurred as a direct result to changing pseudopod dynamics. Pseudopod directionality, quantity, and lifespan were quantified based on deformability, protein diffusivity, and viscosity ratio. While swimming speed was seen to increase with increasing deformability

and protein diffusivity, non-monotonic behavior was seen as the viscosity ratio was changed. Results show a strong coupling between cell deformation and membrane protein diffusion in deciding cell motility.

Chapter 4

Adhesion-Independent Pseudopod-Driven Migration of an Amoeboid Cell in Extracellular Matrix Geometry[2]

Locomotion of amoeboid cells is accomplished through finger-like extensions of the cell body known as pseudopods, which are the primary method of motility for many cells within the body including leukocytes, embryonic cells, and cancer. In addition to the involvement of complex deformation, biomolecular reactions, and viscous interactions, cells within the body are often exposed to a confined geometry known as the Extracellular Matrix (ECM). Here we present a computational modeling study of an amoeboid cell migrating through a fluid-filled porous matrix array characterized by finite-sized periodic spheres. The influence of cell deformability, matrix porosity, and obstacle size on motility are analyzed. Migration is found to be completely inhibited below a certain parameter range, to which phase plots are presented. New cell dynamics seen as a result of obstacle interactions are found, including probing, tug-of-war, doubling-back, and freezing or cell arrest. Furthermore, the nearly persistent unidirectional motion seen in unbounded migration is found to be lost in the presence of obstacles due to modified pseudopod dynamics. This mechanism, however, is seen to aid in matrix penetration as the cell seeks new avenues to travel through. These results show a strong coupling between cell

---

[2] Adapted from Ref. 103 with permission from The Royal Society of Chemistry.

deformability and ECM properties, thereby providing new insight into amoeboid migration in a confined medium.

4.1 Introduction

In this chapter, the pseudopod-driven amoeboid cell is immersed in porous extracellular matrices of rigid spheres, while porosity and obstacle size are varied. Numerous examples can be drawn upon regarding amoeboid cell migration within the body. Some physiological processes include the migration of leukocytes through tissue [22], fibroblast reconstruction of damaged tissue [59], epithelial cell migration for wound healing [24], and key positioning of cells during embryonic development [23]. One of the most prominent examples, however, is the amoeboid migration of cancer cells as they detach from the tumor and metastasize into healthy tissue [21,57,138].

Pseudopod formation itself represents a complex process. Key proteins such as Arp2/3 or WASP, which are activated by some stimulus, proceed to activate nucleation sites within the cell, polymerizing G-actin monomers into F-actin filaments [139]. A protrusive force is generated by these growing filament networks, thereby causing a local protrusion of the cell membrane. When adhesive interactions are possible, further considerations are necessary. Adhesive proteins such as integrins form bonds between a substrate and cell body to allow for force transmission. Myosin II proteins present in the cell rear then generate a contraction event, forcing the cell forward as posterior bonds are broken.

While cells are fully capable of crawling or swimming [2,3,113] though, cells within the body are frequently exposed to confining three-dimensional environments. Known as the Extracellular Matrix (ECM), this complex and heterogenous structure is constructed of

various protein fibers embedded in a gel-like polysaccharide fluid [39,51,57,140,141]. The ECM microstructure, which is characterized by features such as porosity, pore size, and fiber orientation, plays host as a scaffold for cells, often influencing their behavior through alignment, stiffness, and elasticity [142]. For instance, mesenchymal cancer cells adopt large adhesive forces as they bore through tissue in order to metastasize and form new tumors, while fibroblasts may use large adhesive forces in connective tissue, remodeling the ECM as they pass through. Amoeboid motility through the ECM is decidedly different, though. Amoeboid cancer cells require little to no adhesive capability, instead using their high deformability to squeeze through gaps in the matrix tissue [58,143-144]. Neutrophils are also capable of adopting the amoeboid mode with little or no adhesion. In fact, neutrophils lacking integrins showed no significant differences migrating in three-dimensional environments as compared to wild-type cells [52]. Furthermore, the amoeboid mode can also serve as a compensation strategy for other migration modes which are either blocked or inconvenient [1]. Because of this unique adaptation, ECM conditions characterized by little or weak adhesion coupled with high confinement can cause the amoeboid phenotype to be selected [58]. For instance, a metastatic cancer cell can revert to the amoeboid mode if their ECM-degrading mesenchymal mode is inhibited, thereby continuing its malevolent journey.

In this work, our objective was to present a computational model serving to study amoeboid motility through a confined medium. Several noteworthy studies have investigated cell motility through confined spaces. Wu *et al* [132] modeled the swimming of a two-dimensional amoeboid cell through a confined microchannel and without adhesion using the boundary integral method and force harmonics to model protrusive and

contractile forces. Confinement was found to increase swimming speed to a certain limit, after which migration was negatively affected. Lim *et al* [13] developed a two-dimensional model of an adhesion-free blebbing cell migrating through microchannels of increasing confinement, treating the cell as an elastic membrane and elastic actin cortex connected by Hookean springs. Using the boundary integral method, they found locomotion was possible without adhesion, while confinement benefits migration to a certain extent. Schlüter *et al* [34] analyzed the dynamics of a two-dimensional rigid cell subjected to Stoke's drag, migrating on a substrate composed of moveable cylindrical fibers of varying orientations and stiffness using a force-based method. Cells were observed to prefer stiffer matrices over softer variants, where cell persistence was seen to increase with more ordered substrates. Elliott *et al* [7] considered amoeboid motility through two-dimensional rigid but moveable obstacle fields, in addition to three-dimensional unbounded medium, although fluid interactions were not considered. Pseudopods were generated via an activator-inhibitor system, while adhesion was modeled simply as a frictional force. Hecht *et al* [29] simulated two-dimensional chemotactic amoeboid cells without adhesion in unbounded flow and through obstacle and maze-like geometries. Moure and Gomez [10] created a phase-field model for a three-dimensional amoeboid cell, including transport equations to describe cytosolic biochemistry dynamics, an activator-inhibitor system to describe cell biochemistry, and hydrodynamic drag to describe adhesive forces. Simulations were generated for two-dimensional cells moving through obstacle geometries, in addition to three-dimensional cells migrating through rigid, periodic, fibrous cylindrical networks.

Also worth briefly discussing are the works by Vanderlei *et al* [130], whose two-dimensional model resolved cell deformation, internal and external flow, and advection-diffusion of biological species within the cell volume. Bottino and Fauci [131] similarly modeled a motile cell with the cytoskeleton described by networks of fluid-immersed springs. Farutin *et al* [108] considered a deformable cell driven by an oscillating axisymmetric force in an unbounded medium, while Najem and Grant [133] used a phase-field method to simulate three-dimensional neutrophil migration responding to external cues, but ignoring fluid interactions.

While significant advancements have been made in modeling amoeboid motility, three-dimensional migration through confining medium remains a challenge, since confinement is known to heavily influence cell behavior. As a result, two-dimensional studies cannot fully replicate cell dynamics seen in three-dimensions [51]. Furthermore, simulation allows freedom of ease to vary matrix and cell properties, which would otherwise be difficult in an experimental setting. With this in mind, a three-dimensional pseudopod-driven amoeboid cell model migrating through arrays of rigid, nondeformable spheres immersed in viscous fluid is presented.

4.2 Results

4.2.1 Interaction Between Reaction-Diffusion, Surface Shape, and Deformation

While not the exact focus of this dissertation, the reaction-diffusion system was observed to produce very interesting dynamics. Key differences were seen between activator-inhibitor modeling on a rigid, spherical cell, and that on a cell with varying membrane deformabilities. The effect of curvature also produced interesting observations. Finally, obstacle interactions with cells were shown to alter dynamics significantly. The

physical insights discussed here are helpful towards understanding the amoeboid dynamics which will be analyzed in forthcoming sections.
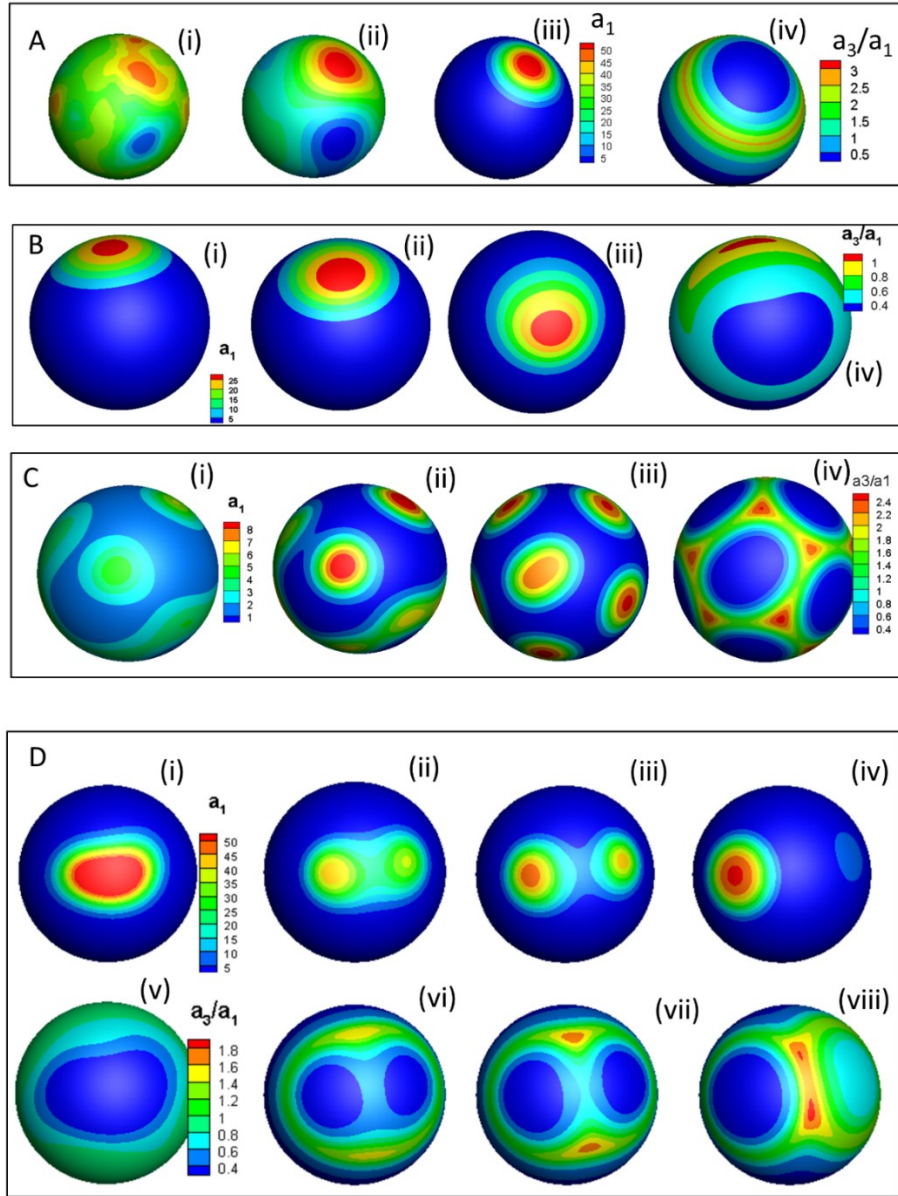
Figure 4.1: Different Turing instabilities generated by the activator-inhibitor system. For **(A-C)**, evolution of the activator patch is shown in (i)-(iii) using the activator concentration a_1, while (iv) shows the ratio of local inhibitor to activator concentration a_3/a_1 corresponding to the time instance (iii). For activator concentration a_1, the regions in red are those of high concentration. **(A)** Single, steady patch. **(B)** Traveling patch. **(C)** Multiple patches. **(D)** Bifurcating patch. In **(D)**, (i)-(iv) shows the activator concentration field, and (v)-(viii) shows the inhibitor to activator concentration ratio at the same time instances. Reproduced from [103] with permission of the Royal Society of Chemistry.

(A)   Turing Patterns on Rigid Spheres

Generated by the reaction-diffusion equations, Turing instabilities lead to the growth and bifurcation of high concentration activator regions. The local activator, described by Equation 2.17, represents a positive-feedback process where a small increase in concentration due to the local noise ϵ is further amplified due to the nonlinear term dependent on a_1^2/a_2 (Figure 4.1A). As the activator grows, however, so does the inhibitors (Equations 2.18 and 2.19). The global inhibitor a_2 suppresses high concentrations of the activator everywhere on the surface except near the instability, where a_1 and a_3 continue to grow. Because of this growth, a gradient develops which sets up the diffusion of each species away from the high-concentration region. The result is a dynamic equilibrium balanced by species production, annihilation, and diffusion resulting in specific patterns of high-concentration activator which is shown in Figure 4.1A(i)-(iii), where a single activator instability is generated. In Figure 4.1A(iv) however, a ring of a_3/a_1 concentration is seen to surround the local activator instability. This suggests the activator is surrounded by a larger-concentration inhibitor which keeps the spot in equilibrium as any concentration which diffuses away is likely neutralized.

By varying the parameters in the reaction-diffusion equations, different patterns can be formed as was shown in the pattern generation section in Chapter 2. For example, in Figure 4.1B, a traveling patch which moves about the sphere is developed, while Figure 4.1C shows the formation of multiple steady patches. In Figure 4.1D, a repeating bifurcating pattern is seen. Stable patches are generated when the inhibitor diffusion is faster than then activator diffusion $(D_3 > D_1)$ while a traveling instability occurs when diffusivities are comparable $(D_3/D_1 \approx 1)$. In each example, though, the high-concentration activator patch

is surrounded by a ring of high a_3/a_1 magnitude, which dictates the eventual equilibrium of the patterns. For example, in Figure 4.1B, the ring thickness varies around the activator patch. As a result, the activator is neutralized if it diffuses out in one direction, but is virtually unaffected when escaping in the other direction. This results in a "moving" activator patch.

Bifurcation patterns are formed when the reaction rate parameter r_1 is large. As seen in Figure 4.1D, a single activator instability bifurcates into two patches, which then move apart as the ring of a_3/a_1 drives a wedge in between them. Eventually one instability decays, and the bifurcation cycle continues. Phase diagrams for the different patterns obtained on a rigid sphere are given in Figure 4.2. $\beta = D_3/D_1$, r_1, and s_1 are varied, showing the sensitivity in which patterns may be formed. For an appropriate pseudopod-generation model, we limit the reaction-diffusion parameters to those which create a bifurcating patch.
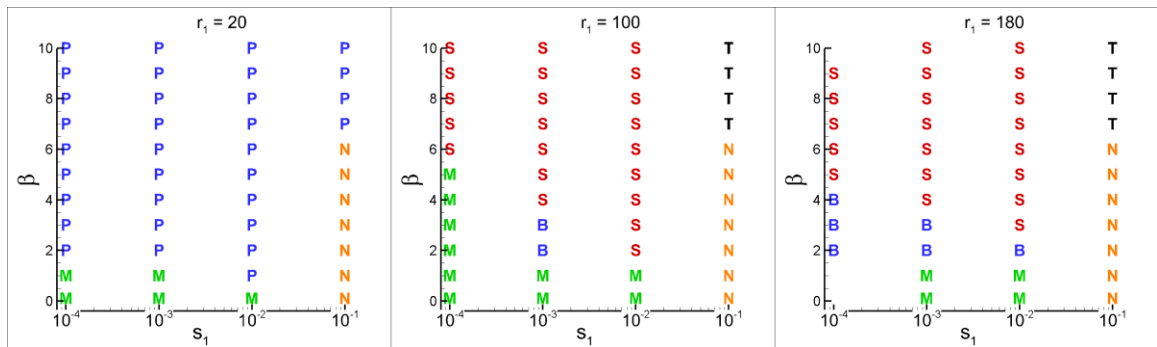
Figure 4.2: Turing patterns generated by the reaction-diffusion equations on a rigid sphere: Single, steady patch of activator (P), travelling patch (M), bifurcating patch (B), multiple stable patches (S), stripes (T), and a noisy lack of patterns (N). The bifurcating pattern appears over larger space with increasing reaction rate r_1, since the reaction-diffusion system becomes more unstable. Reproduced from [103] with permission of the Royal Society of Chemistry.

(B)   **Influence of Curvature on Turing Patterns**

The above discussion was related to Turing patterns on a rigid sphere with constant curvature. Now, the effect of surfaces with varying curvature are discussed. It has been shown in the literature that diffusion is possible entirely due to curvature. A species can in fact concentrate on a convex surface (positive gaussian curvature), or diffuse away from a hyperbolic surface (negative gaussian curvature) [153-154]. Therefore, the former mechanism causes faster growth of activator and local inhibitor in the high curvature regions, also enhancing the relative instability of the pattern. To illustrate this effect, Figure 4.3 shows a Turing pattern on a rigid sphere and on a cup-shaped surface using the same reaction-diffusion parameters. The rigid sphere simulation only produces a single and steady activator patch, while the cup-shaped geometry shows a patch which only bifurcates near the high-curvature region. This curvature dependence is enforced by the surface Laplacian in Equations 2.17 and 2.19.
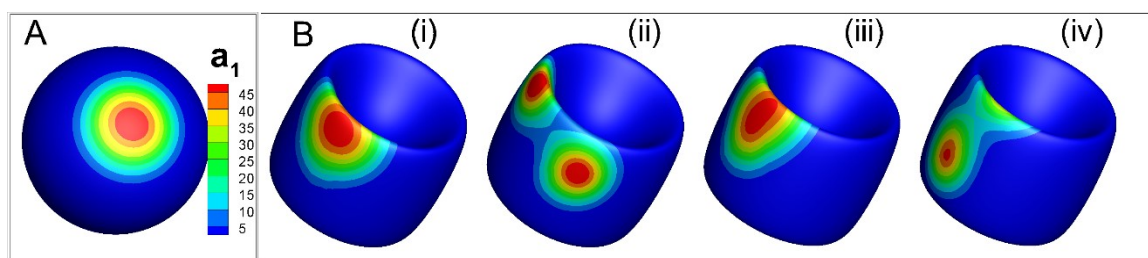
Figure 4.3: Influence of surface curvature on pattern formation. **(A)** A single, steady activator patch is generated on the surface of a rigid sphere for $\beta = 3$ and $r_1 R/D_1 = 150$. **(B)** In contrast, the patch becomes unstable and bifurcates when a cup-shaped object is considered for the same reaction-diffusion parameters. (i)-(iv) show a time sequence of the bifurcating patch. Colors show activator concentration, where red is high activator concentration (a_1). Reproduced from [103] with permission of the Royal Society of Chemistry.

(C)   Surface Deformation

In Figures 4.1 and 4.3, a red contour color is associated with high activator concentration (a_1). For a deformable surface, however, the protrusive force is coupled directly to the activator concentration. In the areas with high a_1, the result is a bulging outward wherever the instability is localized to. This process is shown in Figure 4.4A which shows the evolution of the activator concentrations and deformable surface as a pseudopod is generated and then bifurcates. To mimic the behavior of bifurcating pseudopods which have been observed to continually bifurcate, we have selected the relevant parameters for the reaction-diffusion equations to produce an activator-inhibitor system which repeatedly generates bifurcating instabilities. In Figure 4.4B, the ratio a_3/a_1 is plotted, which shows a similar behavior to that of a bifurcating instability on a rigid surface as seen by Figure 4.1D. The ring forms encroaches on the lone patch, thereby forcing a bifurcation and the subsequent separation of each pseudopod. One Turing instability will then die out, and with it the pseudopod linked to it, after which the cycle will repeat again.

Deforming surfaces cause activator instabilities to become more unstable, as seen by the phase plots in Figure 4.4C and D, which describe bifurcating regions in terms of β and r_1. Figure 4.4C is for the case of a rigid sphere, while Figure 4.4D is that of a deforming sphere with a deformability of $\alpha = 5$. The region where bifurcations occur is seen to expand in the case of the deformable sphere, because the protruding surface generates a curvature which as noted in section B creates a more unstable activator patch which bifurcates. To summarize, we use patterns of bifurcating activator patches to mimic the bifurcations of pseudopods in amoeboid cells. These patterns are more likely to bifurcate

in regions of high curvature, and therefore are also more likely to form when a protrusive

force is present, as is the case in a deformable cell.
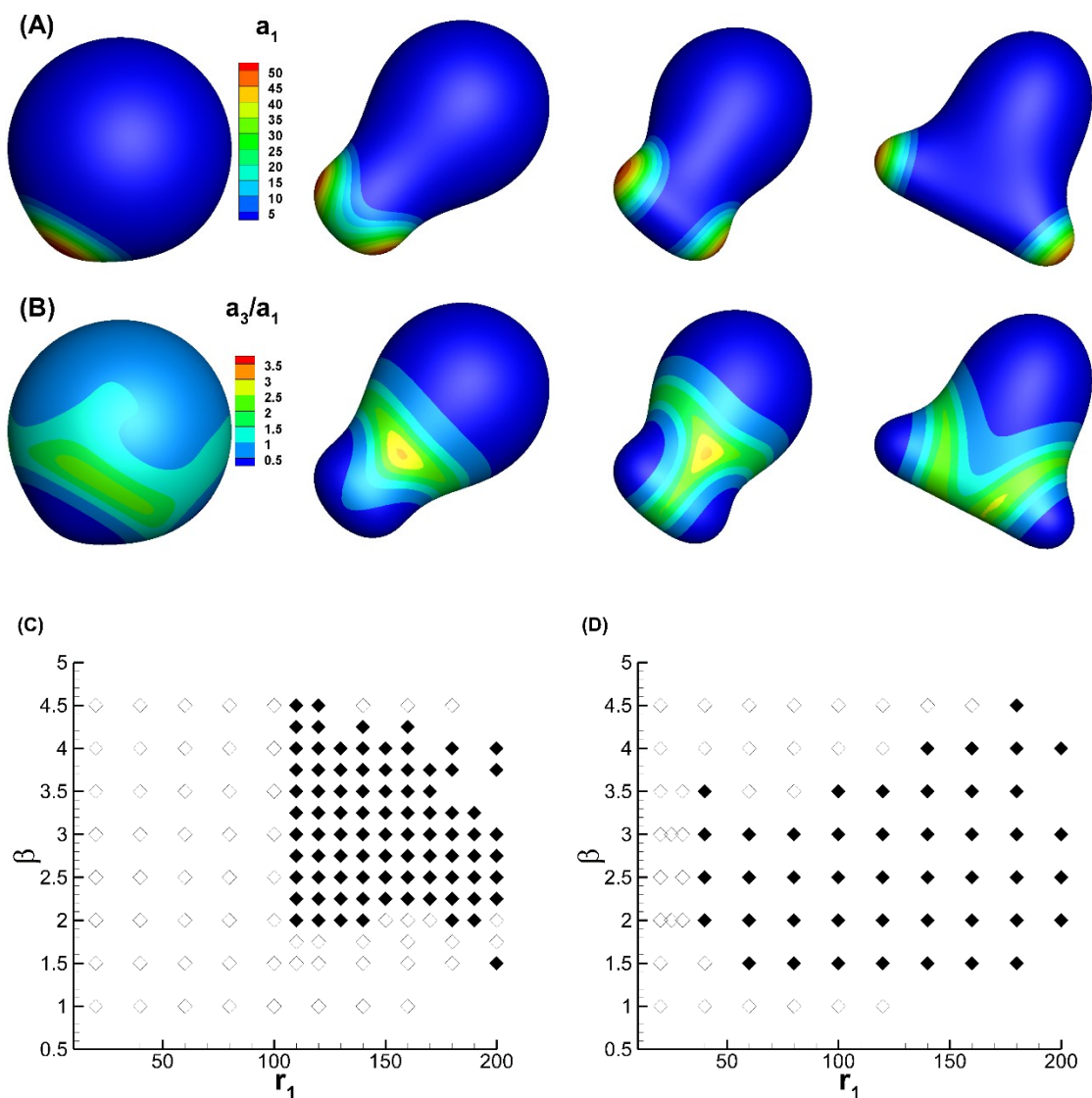
Figure 4.4: Influence of surface deformation on Turing patterns. **(A)** Time sequence of bifurcating activator patch, and the resulting bifurcating pseudopod is shown for a deformable cell. **(B)** Ratio of local inhibitor to activator concentrations at the same time instances as in **(A)**. **(C-D)** are phase plots showing bifurcating (filled symbols) and non-bifurcating (open symbols) for **(C)** the rigid sphere and **(D)** deformable cell. Reproduced from [103] with permission of the Royal Society of Chemistry.

(D)   **Presence of Obstacles**

In Figure 4.5, an obstacle is encountered by the deforming sphere. Two pseudopods attempt to wrap around it, which results in a concave impression left by the obstacle. In the bifurcation cycle, one activator instability decays, after which the other instability bifurcates. As discussed in Section B, the high curvature near the rim causes the activator patch to become unstable and bifurcate, while locally hyperbolic regions just below the rim help stabilize the patch. As the activator tries to move past the rim, it causes further protrusion around the sphere, and as a result, an increase in curvature which adds to the concavity. As a result, the patch is bounded inside the concave cavity, where bifurcations continuously occur over time as the process repeats.
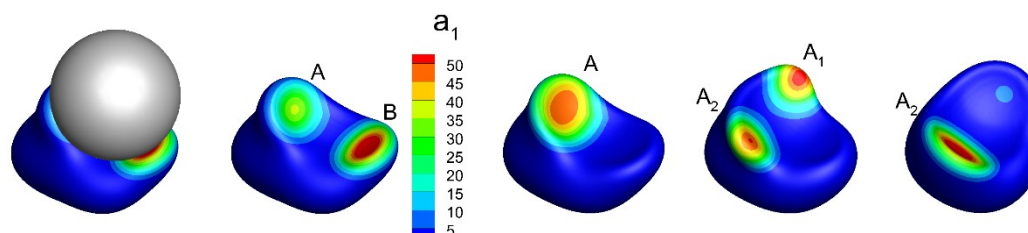
Figure 4.5: Time sequence of pseudopod dynamics in the presence of an obstacle (sphere in grey). Activator concentration is shown in color, with red being the maximum concentration. The membrane protrudes outward at regions of high activator concentration. Starting with two activator patches labeled as **A** and **B**, one of them **(B)** dies over time, while the other **(A)** bifurcates in to two daughter patches, and hence, two pseudopods labeled **A1** and **A2**. Subsequently **A1** dies, and the process repeats. The activator patch favors hyperbolic regions (Section B). As it tries to move over the rim, it causes even more elongation of the rim, thereby confining itself within the concave front. Reproduced from [103] with permission of the Royal Society of Chemistry.

So, it is the interaction between cell deformation and the obstacle which causes the activator patches, and therefore the pseudopods to be confined to the concave region. We have run additional simulations with a concave-shaped rigid geometry (similar to Figure

4.3), and observed an activator patch can indeed escape the concavity and form pseudopods on other points on the surface.

4.2.2 General Motility Behavior

A sequence of an amoeboid cell migrating through the ECM over time is considered in Figure 4.6. Beginning with an initially spherical shape and allowing the activator-inhibitor system to run, a Turing instability develops which forms a protruding *de novo* pseudopod. Cycles of bifurcations, pseudopod growth, and retractions are common as the cell navigates around the rigid obstacles. Indeed, the cell shapes accompanying each type of cell process are similar to experimental images of crawling and swimming Dicty cells seen in [2-3,27,53,113]. Cells are noted to squeeze through gaps as the protrusive force from each pseudopod acts to pull the cell forward. Figure 4.6 also shows cells as being highly deformed and confined by ECM geometry as its pseudopods weave around and through dense obstacles. The cell body is often seen conforming to obstacle geometry as pseudopods pull the cell near the adjacent ECM. Furthermore, when forward migration is hindered by obstacles, the cell is capable of repolarizing, where it turns around along its original trajectory in order to find a more suitable path. More interesting dynamics are also seen. Pseudopods can protrude independently in opposite directions, forcing the cell to straddle against an imposing obstacle. In time, a pseudopod will then retract, allowing the cell to proceed forward past the obstacle. Interesting interactions between the activator-inhibitor system and cell membrane are seen when deformed by a convex obstacle. Bifurcating Turing patterns are seen to remain confined to regions of concavity on the cell front, preventing a cell from generating pseudopods, which results in a stuck cell. To address this issue, a lubrication pressure is added to the model which acts on the cell

membrane if its distance to the obstacle surface is less than two Eulerian grid points. This is also conveniently the same distance used to distribute membrane force using the delta function from Equation 2.50. Tests were run to determine if migration would be fundamentally changed using a smaller or greater distance, with results indicating a negligible change. Secondly, if an active pseudopod achieves a distance closer than two Eulerian grid points to an obstacle surface, the entire activator-inhibitor system across the cell is reset to unity, while the surface noise is zeroed. A similar approach was taken in [10-11], and allows the generation of Turing instabilities, and therefore pseudopods, in alternate directions, allowing the cell to continue migrating through the ECM.
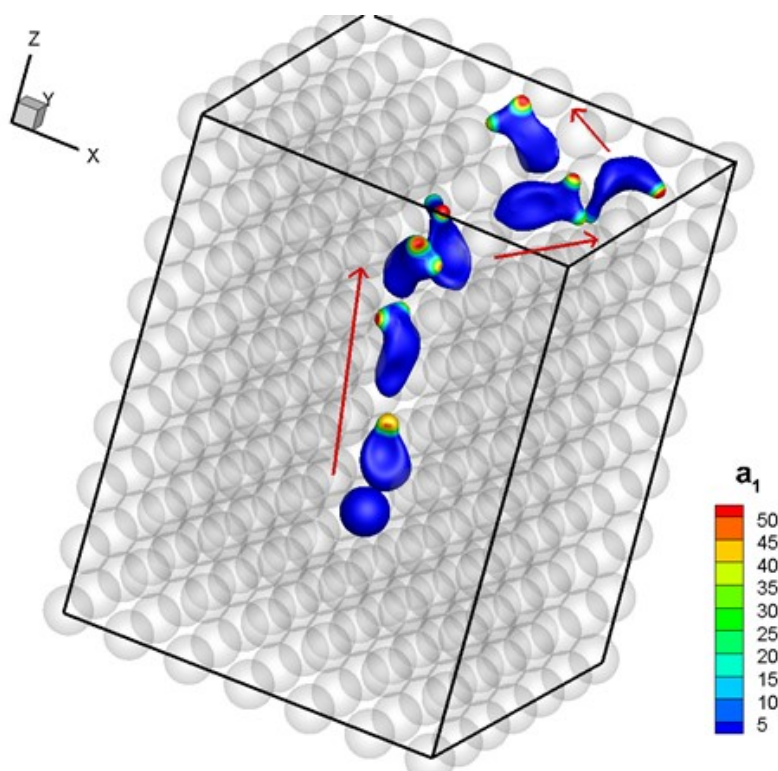
Figure 4.6: Simulation results: sequence of images of a migrating amoeboid cell through the extracellular space. The extracellular solid phase represented by an array of rigid, non-moving spheres of finite size is shown in grey. Parameters are $\alpha = 5$, $\gamma = 1$, and $\phi = 0.79$. Direction of cell motion is shown by red arrows. Color contours on the cell surface represent activator concentration. Reproduced from [103] with permission of the Royal Society of Chemistry.
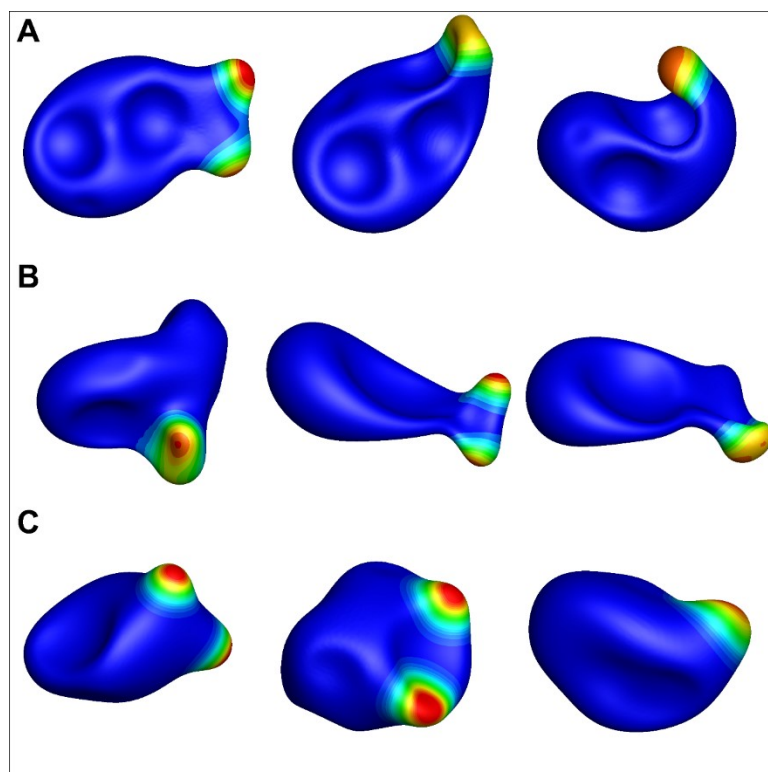
Figure 4.7: Examples of highly complex cell shapes predicted by simulations. **(A)** $\alpha = 5$, $\gamma = 0.5$, and $\phi = 0.83$. **(B)** $\alpha = 7$, $\gamma = 1.0$, and $\phi = 0.68$. **(C)** $\alpha = 1$, $\gamma = 1.0$, and $\phi = 0.83$. Color contours on the cell surface represent activator concentration. Reproduced from [103] with permission of the Royal Society of Chemistry.

Predicted cell shapes are seen as comparable to experimental images of cells migrating through tissue [1,22,50,53]. Cells are observed to undergo significant deformation as they interact with obstacles, where the degree of deformation is determined by membrane stiffness, matrix porosity, and obstacle size. Comparisons can be made in Figure 4.7, where cell shapes are shown for several different parameter sets. The extremely deformed cells seen here show off the robustness of our method and nonlinear membrane model. The Lagrangian mesh remains fully resolved, therefore no mesh refinement is required as compared to other works which require *ad hoc* corrections [7,9,123-124,126,128]. Case A of Figure 4.7 shows a cell with high deformability ($\alpha = 7$), smaller obstacle radius

($\gamma = 0.5$), and moderate porosity ($\phi = 0.83$). Deformation is clearly evident as multiple

obstacle impressions are left on the cell as it successfully navigates through the ECM. This

is possible even under conditions of high confinement. Case B of Figure 4.7 considers a

cell with high deformability ($\alpha = 7$), cell-sized obstacle radius ($\gamma = 1.0$), and low matrix

porosity ($\phi = 0.68$). Due to the increased confinement, the front half of the cell appears

highly flattened as it attempts to migrate through the narrow gap between obstacles, while

the cell rear bulges out as cytoplasmic fluid is squeezed backwards. In case C of Figure

4.7, a cell with low deformability ($\alpha = 1$), cell-sized obstacle radius ($\gamma = 1.0$), and

moderate porosity ($\phi = 0.83$) is pictured. Deformation is again noticeable, yet due to the

increase in cell stiffness, the cell appears more spherical and cannot penetrate the matrix.

Interesting dynamical modes which were observed during cell-obstacle interactions are

now discussed. Figure 4.8 illustrates two time sequence plots of cell migration, where

obstacles have been removed for clarity purposes. In Figure 4.8A, the sequence begins at

(a) and ends at (n). Starting at (a), two *de novo* pseudopods are generated. As one

pseudopod decays and begins to retract, the other pseudopod bifurcates into two daughter

pseudopods as seen in (b). Further pseudopod activity occurs in (c), until and interesting

behavior is seen in case (d). All existing pseudopods are terminated and begin to retract as

the cell enters a brief period of inactivity. We have named this behavior "freezing" or

temporary cell arrest, as the cell may remain inactive for several dimensionless time. In

(e), the cell reactivates with a bifurcating *de novo* pseudopod, which also changes the cell's

direction. Further pseudopod activity is seen in (f) and (g), where a turn is instigated due

to an obstacle situated directly ahead in the cell's path. Because anterior pseudopods cannot

move the cell forward, an errant pseudopod is eventually generated which forces a sharp

turn in the cell, thus allowing it to further penetrate the matrix. In (h) through (j), further pseudopod dynamics such as bifurcation and meandering are seen, while in (k), meandering helps the cell turn gradually. Another freezing event occurs in (l) and (m), where the transition to a relaxed equilibrium shape can be seen. Finally, in (n), *de novo* pseudopods are again formed which propel the cell forward.

Another interesting dynamical behavior is seen in Figure 4.8B. Similar to the previous sequence, the cell begins with *de novo* pseudopod formation at (a), which results in a bifurcation at (b). In (c), the termination of active pseudopods can be seen due to an obstacle directly ahead, thus causing the cell to generate a pseudopod, forcing a hard turn. In (e) through (g), pseudopod bifurcations are seen. A freezing event then occurs in (h), causing the cell to briefly become inactive as it retracts. In (i), the cell become active again with a *de novo* pseudopod, which then bifurcates in (j). Another termination takes place in (k), setting the stage for a new type of behavior seen in (l) through (n). The cell begins to generate pseudopods which briefly extend outwards, usually through narrow gaps, and which quickly contact an obstacle, resulting in their subsequent termination and retraction. This process happens repeatedly, allowing the cell to slowly move forward and overcome the obstacle. We call this behavior probing, and while freezing is characterized by a complete withdrawal of pseudopods and period of inactivity, probing exhibits an activator concentration which cyclically grows and retracts pseudopods. Another instance of probing can be seen in (p) through (s) after a turning event in (o).
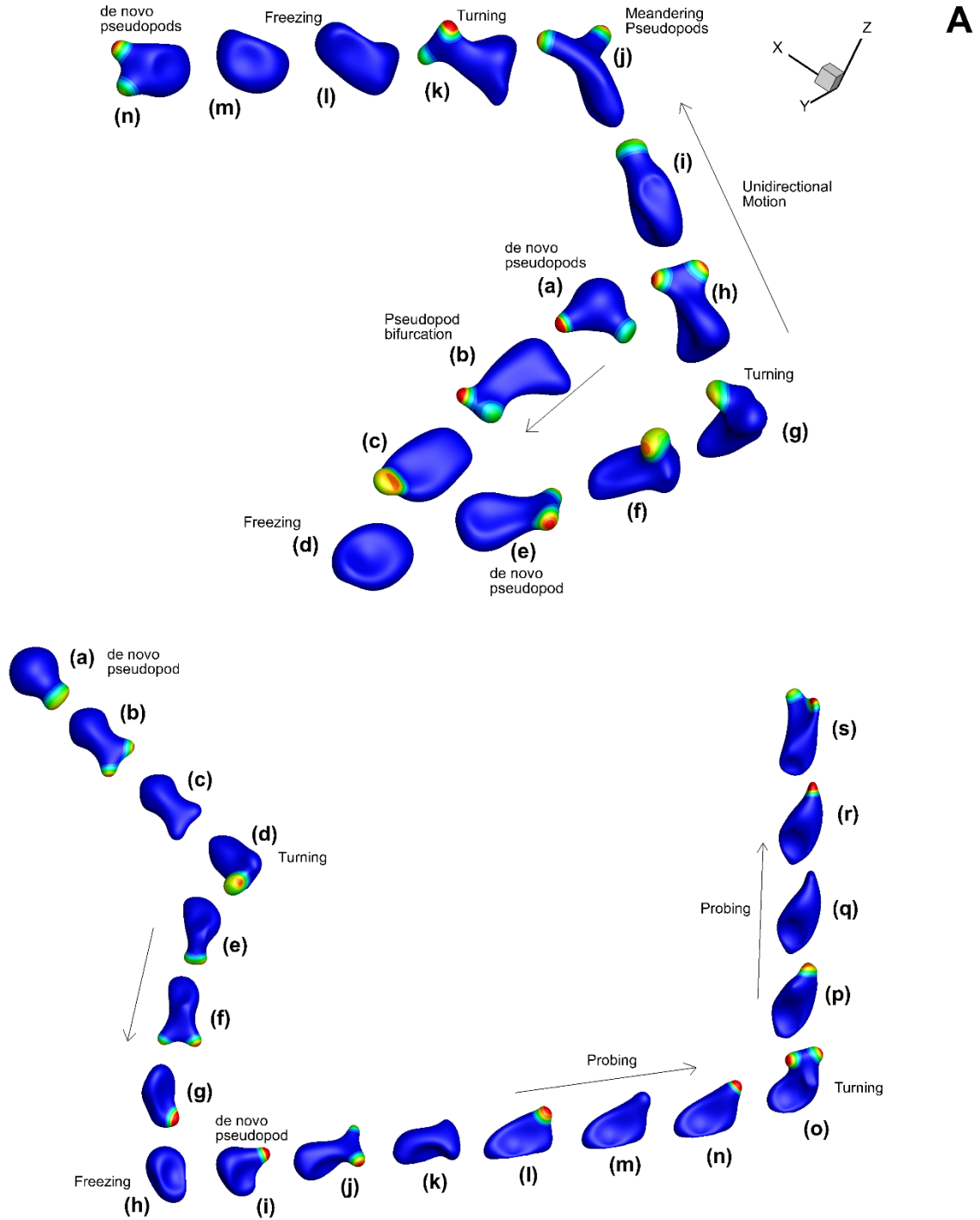
Figure 4.8: Different motility dynamics observed in our simulations for amoeboid cells migrating through the ECM. Spherical obstacles are not shown for clarity. The time sequence begins at (a) and proceeds onwards. **(A)** $\alpha = 5$, $\gamma = 1.0$, and $\phi = 0.79$. **(B)** $\alpha = 7$, $\gamma = 1.0$, and $\phi = 0.68$. See text for descriptions. Color contours represent activator concentration. Reproduced from [103] with permission of the Royal Society of Chemistry.

4.2.3 Obstacle-Mediated Dynamics

The freezing and probing dynamics offer new insights into amoeboid cells migrating through confining matrix environments. For this reason, each dynamic is further investigated. Figure 4.9A examines the case of freezing, showing an instantaneous velocity plot stacked together with a distance traveled curve. During three time periods within the interval of simulation, cell speed is shown to drop to essentially zero, while the distance traveled remains constant. These two pieces of evidence further strengthen the case that the cell becomes inactive during a freezing event. At the exact end of a freezing occurrence, the instantaneous velocity quickly spikes as a *de novo* pseudopod forms and pulls the cell out of its confined state. A sequence showing the amoeboid cell's transition to inactivity during a freezing event is shown in Figure 4.9B. The sequence shows pseudopod extension followed by termination and retraction, where the cell begins to adopt a more spherical shape. The cell remains in an inactive state for several dimensionless seconds until a suitably positioned pseudopod can pull the cell into a new location. We note that activator patches are still being formed by Turing instabilities during a freezing event, but they are quickly reset due to the possibility of the cell becoming stuck on a convex obstacle as previously discussed. If areas of high-concentration activator continue to form in inconvenient areas, the freezing event will continue until a suitably placed instability can remove the cell from its present location. Freezing behavior has been observed experimentally for neutrophils migrating in three-dimensional ECM [52]. It is possible, however, that this behavior could be generated through chemokine-directed activity, since chemokines are known to induce cell arrest to halt T-cells in areas of infection [22], or draw leukocytes to stop or slow down near a source [145]. Because our simulations lack

any chemical signaling, it is possible that confinement, a mechanical effect, can also instigate cell arrest.
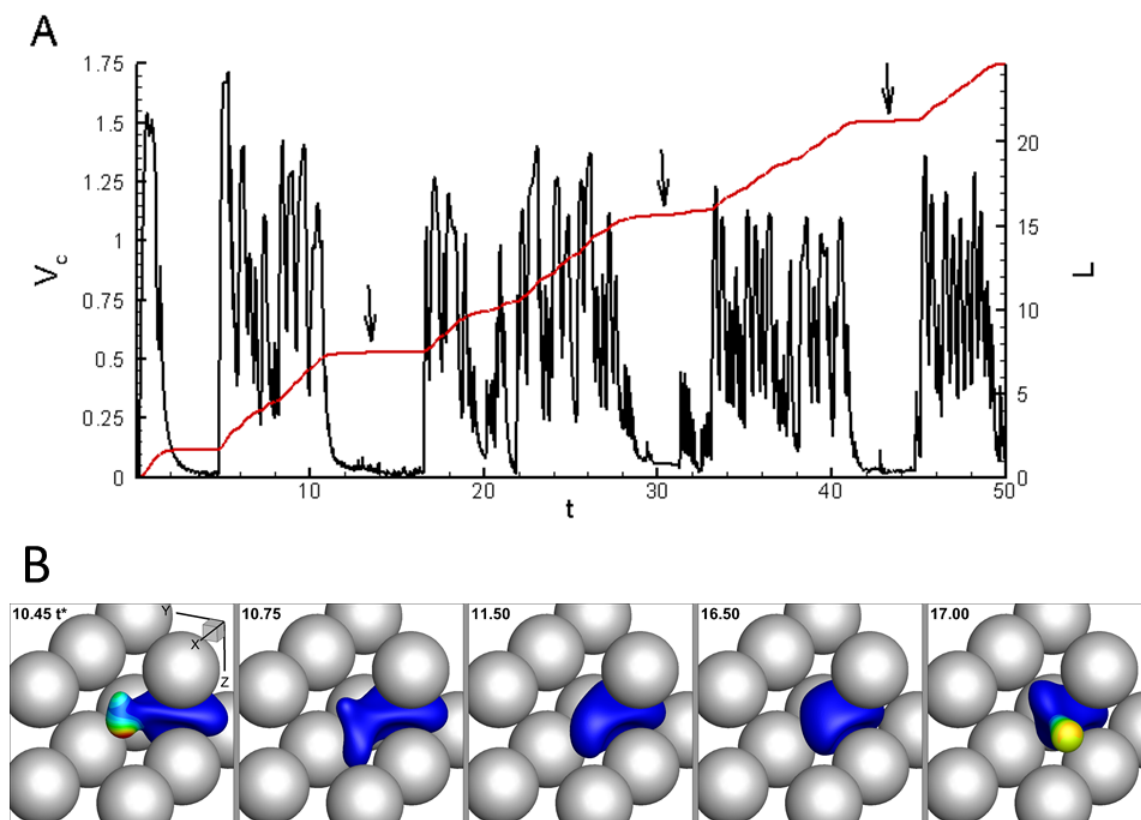
Figure 4.9: Obstacle-mediated dynamics: Freezing of cells in a highly confined matrix. **(A)** Instantaneous velocity of the cell centroid V_c (left axis, black line), and distance traveled L (right axis, red line). Parameters are $\alpha = 5$, $\gamma = 1.0$, and $\phi = 0.79$. Arrows are used to indicate freezing events. **(B)** Time sequence of cell behavior during the freezing event occurring over $t \approx 10.5 - 17.0$ in (A). The sequence shows pseudopod termination, cell retraction, and formation of a new pseudopod in a different direction. Reproduced from [103] with permission of the Royal Society of Chemistry.
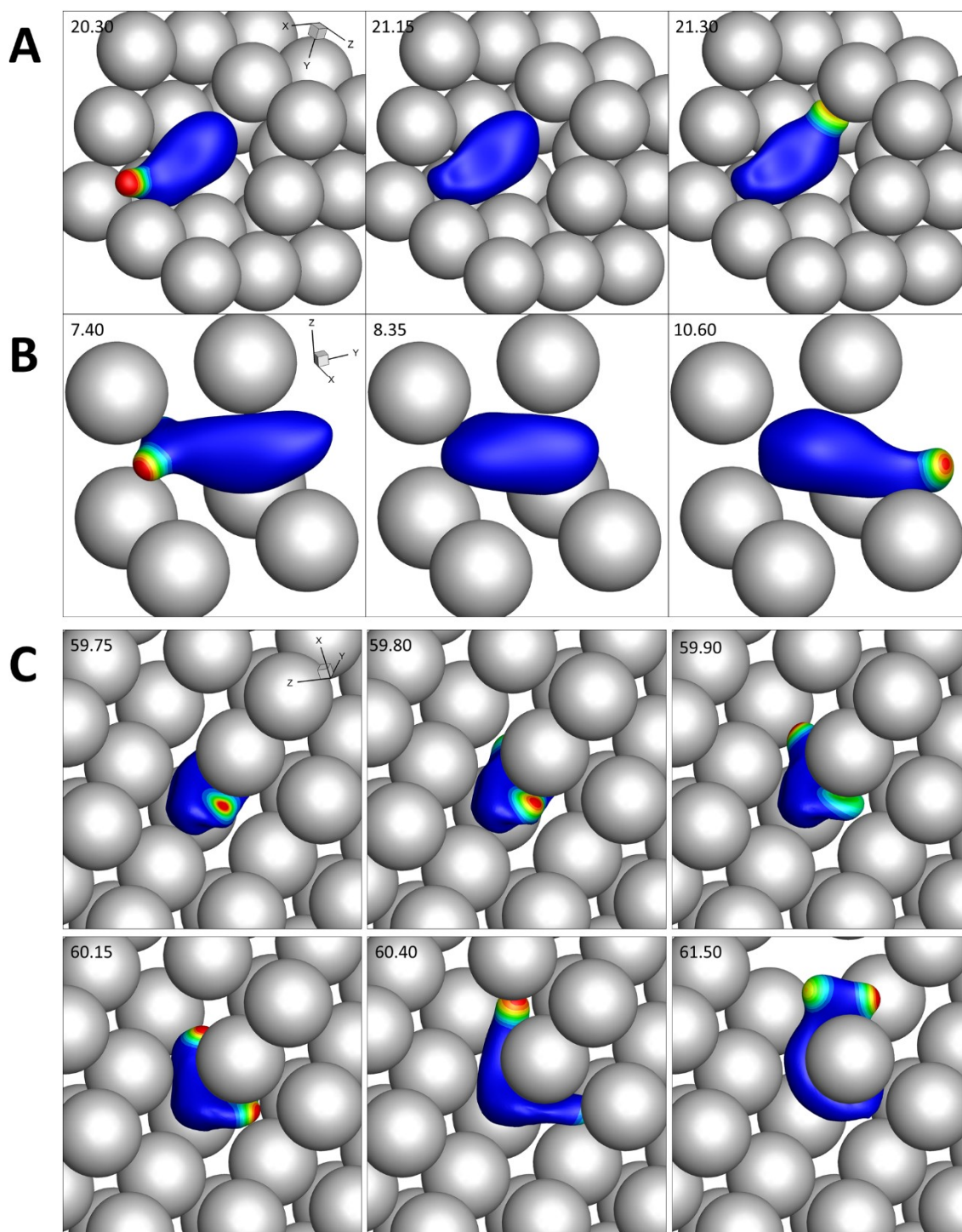
Figure 4.10: Obstacle-mediated dynamics: **(A-B)** Two examples of doubling-back dynamics. (**C**) Tug-of-war between pseudopods straddling an obstacle. Some obstacles have been removed for clarity. Dimensionless time is listed in the top left corner of each frame. Reproduced from [103] with permission of the Royal Society of Chemistry.

During freezing events, or after pseudopod termination due to obstacle closeness, another interesting dynamic is observed, and shown in Figure 4.10A and B. Termed "doubling-back," cells which are prevented from migrating in the forward direction by obstacles are sometimes shown to freeze briefly, then completely repolarize and turn around along their original trajectory. Doubling-back behavior has been observed in experimental conditions with T-cells confronted by impassible structures directly ahead [22]. Note that the same mechanism which causes freezing is responsible for doubling-back. A pseudopod collision with an obstacle forces a reset of the activator-inhibitor system, after which a new *de novo* pseudopod is formed by chance on the cell rear. The cell is then able to continue its migration through the matrix. Another interesting dynamic, termed tug-of-war is seen in Figure 4.10C. This behavior occurs when opposing pseudopods fork around both sides of an obstacle, effectively forcing the cell to remain impacted until one pseudopod decays and retracts, leaving the remaining pseudopod free to carry the cell forward. The tug-of-war dynamic has also been observed experimentally with neutrophils *in vitro*, noting no significant bias in the direction chosen by the cell [146].

Finally, a more detailed description of the probing dynamic is performed. Recall that an extending pseudopod will trigger a reset of the activator-inhibitor system to prevent instabilities forming in the concave membrane indented by the obstacle. After a brief pause, a pseudopod again forms in the same position on the cell. Cycles of this probing behavior allow the cell to creep forward through a constriction. Figure 4.11A shows the instantaneous cell centroid velocity during a probing event. Small shark-fin shaped curves in the velocity plot are evident, with each spike representing the movement of the cell centroid due to extension and retraction of a single pseudopod. An illustration of this

behavior is seen in Figure 4.11B. Compared to the velocity plot for freezing in Figure 4.9A, we note that the cell velocity is always nonzero, since probing is slowly forcing the cell forward through the constriction. A probing event can also end with the bifurcation of a pseudopod as shown in Figure 4.11C. Although the confinement is large in this example, we note that probing can occur in more porous environments if a pseudopod is suitably positioned near an obstacle. Probing has also been observed in experiments, which showed constant shape change with protruding and retracting pseudopods [52,145]. The idea of probing can also be related to dynamic information sampling, where exploratory pseudopod protrusions are used for spatiotemporal sensing to examine the cells adjacent environment [22,145].
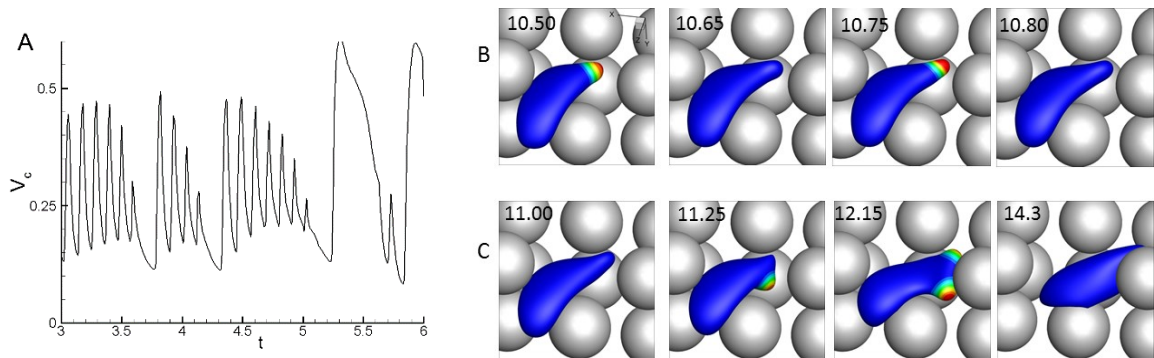
Figure 4.11: Probing dynamics. **(A)** Instantaneous velocity of cell centroid for $\alpha = 7$, $\gamma = 1.0$, and $\phi = 0.68$. **(B)** Sequence showing cell activity during a probing event. **(C)** Sequence showing the transition from probing to bifurcation dynamics. Some obstacles have been removed for clarity. Dimensionless time is listed in the top left corner of each frame. Reproduced from [103] with permission of the Royal Society of Chemistry.

4.2.4 Limits on Motility

Because cell migration is heavily reliant on pseudopod dynamics and confinement, it is no surprise that obstacle-induced pseudopod dynamics such as freezing or probing have large effects on overall cell migration. If confinement becomes too severe, cell motion can

completely be inhibited. We have found that cell deformability, matrix porosity, and obstacle size have a significant effect on cell migration. In Figure 4.12A, the influence of cell deformability and matrix porosity on the instantaneous cell velocity is plotted, where the corresponding cell centroid trajectories are plotted in the inset. For a low deformability ($\alpha = 1$) and a moderately dense matrix ($\phi = 0.68$), cell migration is not possible. Although activator patches and pseudopods are generated on the cell as seen by the fluctuations in velocity, they are unable to penetrate the small gaps of the matrix. The cell may change its direction of motion, but simply cannot penetrate the ECM due to an insufficiently low deformability. If deformability is increased to $\alpha = 5$ for instance, the cell is sufficiently soft to penetrate the matrix, though large fluctuations in speed indicate some difficulty in doing so based on the cell shape (similar to Figure 4.7B). Probing and other dynamics are also likely to be observed in this confined geometry. If the cell deformability is kept constant at $\alpha = 5$, but the matrix porosity is adjusted to $\phi = 0.54$, the cell is again unable to penetrate the matrix. Probing and other dynamic events are also likely to occur as the cell attempts to bypass the obstacle geometry. Finally, if the porosity is increased to $\phi = 0.87$, sufficient space between obstacles allows the cell to move with limited difficulty as seen by Figure 4.12A. A large distance is seen to be traveled in the trajectory inset (black line). Additionally, larger fluctuations are seen within the instantaneous velocity, indicating that obstacles may interfere with a cell's migration, but the cell quickly turns using alternate pseudopods and proceeds through the ECM.
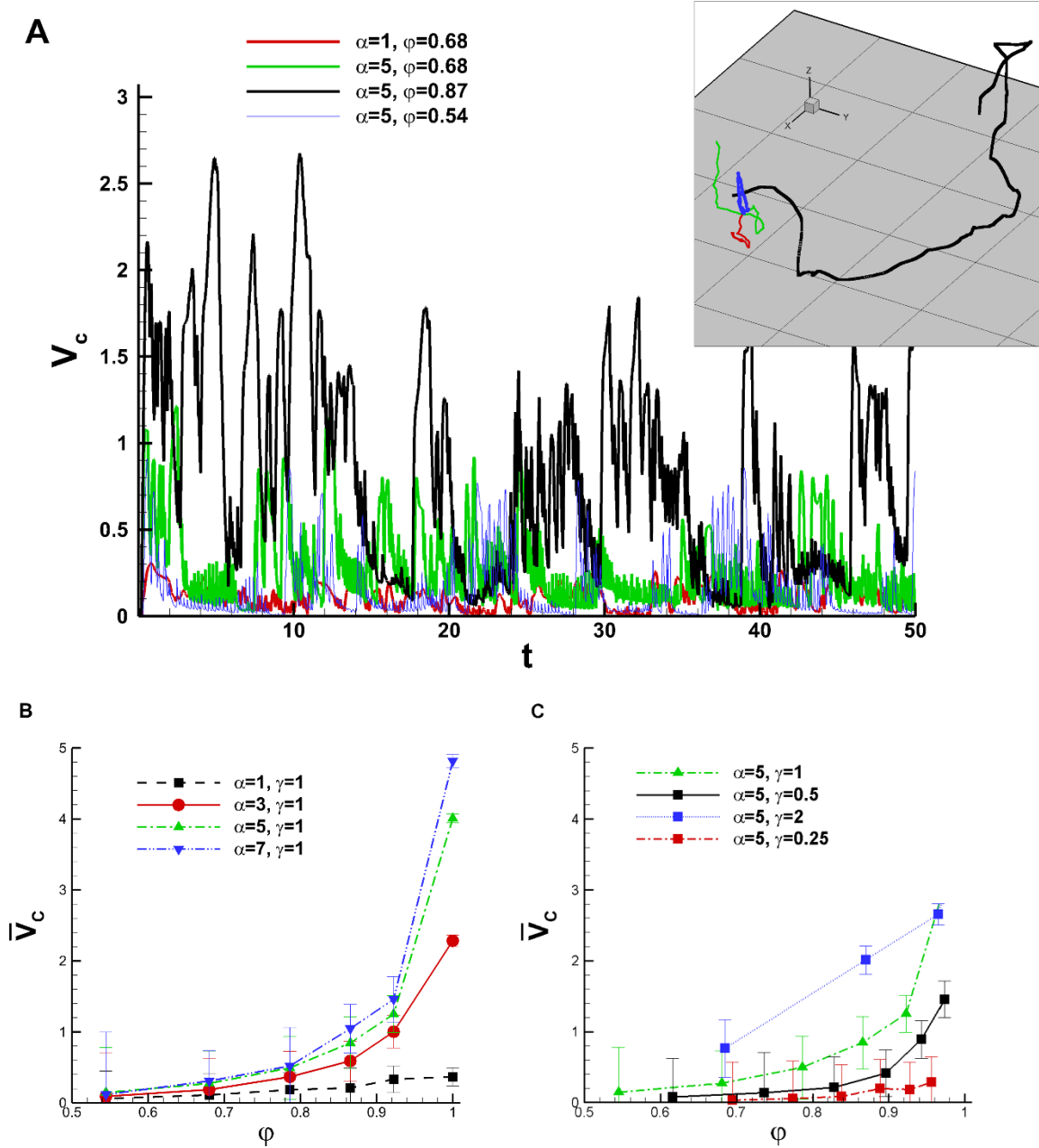
Figure 4.12: **(A)** Influence of matrix porosity and cell deformability on instantaneous cell velocity, and cell trajectory (inset). **(B)** Time-averaged migration speed as a function of matrix porosity for different cell deformabilities. **(C)** Time-averaged migration speed as a function of matrix porosity for different obstacle size. Error bars represent RMS velocity fluctuation. $\phi = 1.00$ represents the cell migration in the unbounded case. Reproduced from [103] with permission of the Royal Society of Chemistry.

Figure 4.12B displays the time-averaged cell migration speed as a function of matrix porosity across the spectrum of membrane deformability. In each case, the migration speed is seen to increase with increasing porosity. Additionally, migration speed is observed to be larger with increasing membrane deformability. An explanation is as follows. A larger matrix porosity indicates less obstacles which might interfere with the cell's trajectory, thus allowing the cell to achieve its maximum potential speed. When lower matrix porosities are involved, however, the cell is frequently disrupted by obstacles, and therefore has a slower migration speed as it moves through the ECM. In the case of cell deformability, softer cells (more deformable) have less difficulty penetrating the narrow gaps, and therefore can achieve a larger speed. Error bars in Figure 4.12B and C are found by scaling the root-mean-squared value by the average velocity. Fluctuations are seen to increase as matrix porosity decreases, since average velocity is smaller, and more frequent cell directional changes due to obstacles increases the fluctuations in velocity. Fluctuations can also be influenced by pseudopod dynamics, which show small maxima and minima in Figure 4.12A, or general cell behavior, which appears as larger-scale maxima and minima. In Figure 4.12C, the time-averaged velocity is plotted against the matrix porosity across the spectrum of obstacle sizes γ while membrane deformability is kept constant. Under constant porosity and deformability, migration speeds are shown to increase as the obstacle size increases. This is a result of the relative distance between two obstacles. For larger obstacle sizes, the same porosity can be obtained with fewer obstacles, thus resulting in larger void space between obstacles. Cells can then achieve larger speeds as they are less likely to be interrupted by obstacle-induced interactions. Conversely, small obstacle sizes

require many obstacles to keep porosity constant, resulting in a tightly-packed matrix with slower speeds due to greater migration inhibition.

Average migration speeds are seen to be comparable to experimental measurements. In [50], leukocyte migration speeds were found to be $\sim 4 \, \mu m \, min^{-1}$, while speeds greater than $10 \, \mu m \, min^{-1}$ were seen in [36] for dendritic and immune cells. Amoeboid cancer cells were reported to have speeds of $4 \, \mu m \, min^{-1}$ in [147], while a range of $0.1 - 20.0 \, \mu m \, min^{-1}$ was predicted in [28]. A peak migration speed as high as $25 \, \mu m \, min^{-1}$ was predicted in [53]. We note here that data providing amoeboid cell migration speeds through three-dimensional mediums is difficult to come by, and the uncertainty in speeds most likely depends on the properties of the cell and matrix involved, as well as the imaging technique performed. A cell radius of $10 \, \mu m$ and a diffusivity of $1 \, \mu m \, min^{-1}$ is used to convert our data into dimensional values. Therefore, a dimensionless velocity of $0.5 - 1.0$ seen in Figure 4.12B for moderate values of membrane deformability, matrix porosity, and obstacle size yields a speed of $3 - 6 \, \mu m \, min^{-1}$, which agrees well with experimental data from the literature.

Figure 4.12 illustrates how cell migration is inhibited as membrane deformability, matrix porosity, and obstacle size are decreased. Figure 4.13 displays these "motility limits" which capture the parameters below where migration is not possible. For a given matrix porosity and obstacle size, migration is only possible if deformability is large enough. Similarly, for a constant deformability, migration can only occur if the matrix porosity is void enough for penetration. Finally, because smaller obstacles are packed closer together, they can also cause cell arrest. These results are validated by experimental observations, in which highly-deformable neutrophils can squeeze through tight gaps

within the tissue, while stiffer fibroblasts are unable to [59], and must migrate using other means such as matrix remodeling [28].
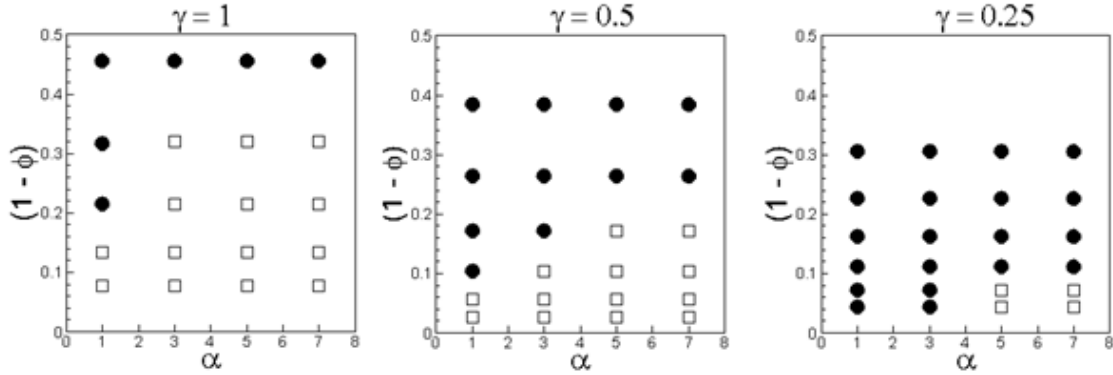
Figure 4.13: Motility limits as obtained from current simulations. Phase diagrams are shown in terms of confinement $(1 - \phi)$ and cell deformability for three different obstacle sizes γ. Open squares represent cases for which cells are able to migrate through the matrix. Filled circles represent cases when cell movement is prevented. Reproduced from [103] with permission of the Royal Society of Chemistry.

4.2.5   Pseudopod Dynamics

It has been shown that amoeboid motility depends on pseudopod dynamics, which in turn depend on membrane deformability, matrix porosity, and obstacle size. Quantification of the average lifetime of pseudopods is plotted in Figure 4.14A and B. The average lifetime of a pseudopod is seen to increase with increasing matrix porosity. This is entirely due to interactions of the cell with an obstacle, since fewer obstacles will cause less pseudopod terminations, resulting in larger lifetimes. Lifetimes are also seen to decrease with increasing matrix deformability. Similar trends were seen for an unbounded cell in Chapter 3 [148]. In this case, increased deformability leads to a greater instability in the reaction-diffusion system, which generates more frequent activator patches and bifurcations as a result. The average lifetime can also be seen as less dependent on porosity

at higher deformabilities. This is because the pseudopods of cells with larger α are able to weave through obstacles, and therefore show less dependence on interactions. The pseudopods of cells with lower α, however, are blunt, causing more frequent collisions with obstacles as porosity decreases. The influence of obstacle size for one case of deformability and porosity is shown in Figure 4.14B. Lifetime is seen to decrease with obstacle size due to a larger number of collisions from more closely-spaced obstacles.
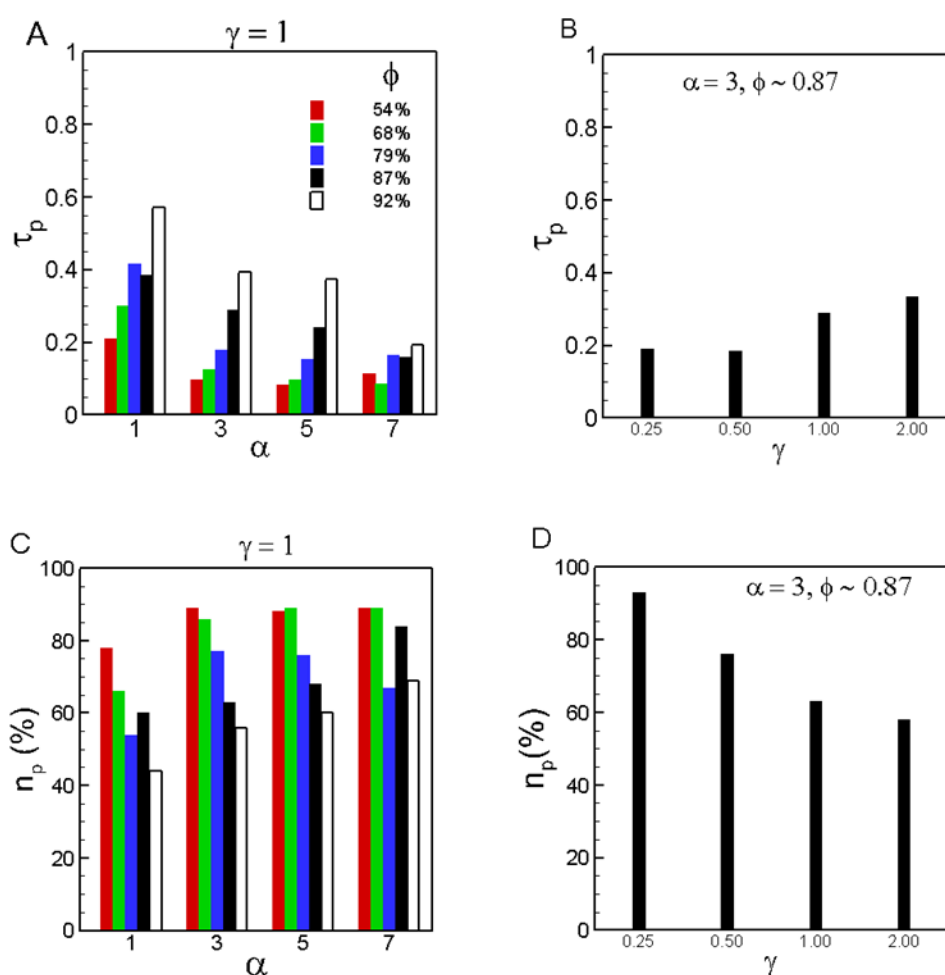
Figure 4.14: Pseudopod lifetime τ_P (scaled by R^2/D_1) **(A)** as a function of α for different value of matrix porosity **(B)** as a function of obstacle size γ. **(C)** Fraction of *de novo* pseudopods to total pseudopods as a function of α for different value of matrix porosity **(D)** as a function of obstacle size γ. Reproduced from [103] with permission of the Royal Society of Chemistry.

Another important characteristic of pseudopod dynamics is the *de novo* frequency (Figure 4.14C and D), or the ratio of *de novo* pseudopods to total number of pseudopods generated within the simulation. As the cell progresses through the ECM, it can either generate pseudopods from bifurcations, or from an independently generated pseudopod known as a *de novo* pseudopod. In Figure 4.14C, proportions of *de novo* pseudopods are shown as a function of membrane deformability and matrix porosity. The fraction of *de novo* pseudopods is seen to increase with decreasing porosity, since a greater number of obstacles results in more pseudopod terminations. New pseudopods are then generated in order to move the cell forward. For a constant porosity, the proportion of *de novo* pseudopods is also seen to increase with increasing deformability. Additionally, *de novo* proportions are seen to increase with decreasing obstacle size as seen by Figure 4.14D. Arguments for these two statements are similar to those given previously for pseudopod lifetime.

4.2.6 Confined *versus* Unconfined Medium

While *de novo* pseudopods are observed to be frequently generated for an amoeboid cell within the ECM geometry, none are generated in the case of cell migration through an unbounded medium [148]. Therefore, *de novo* pseudopod generation can be described as a distinct dynamic seen within obstacle geometries. In the absence of obstacles, the cell will purely produce pseudopods through bifurcation, or "tip-splitting" as it has sometimes been called in the literature [9]. As such, pseudopod lifetimes tend to be much larger when compared to those in a confined medium, approximately $2 - 6$ times greater. In addition, the average number of pseudopods in unconfined medium is approximately 2, while the number is reduced to the range $1.25 - 1.75$ due to the effect from single *de novo*

pseudopods which lower the average. Furthermore, the maximum number of pseudopods seen in unconfined medium is as high as 3 or 4, while that number is only 2 or 3 when obstacles are present. Each of these quantities is seen to decrease as either membrane deformability, matrix porosity, or obstacle size are decreased.

Further differences between cell behavior in confined and unconfined medium can be elucidated by looking at the cell persistence. Figure 4.15A shows two cell centroid trajectories for the case of an unbounded cell and a cell immersed in a high porosity matrix. At moderate deformability ($\alpha = 3$), the unbounded cell is observed to maintain a nearly persistent unidirectional motion for a large distance. Using the same cell parameters but adjusting the matrix porosity to $\phi = 0.92$ shows a drastic difference, however. The cell trajectory is characterized by short, frequent turns which are seen to have little persistence due to obstacles forcing cells to slow down and change direction. Turning events are not exclusive to cells interacting with obstacles however, as was seen in the case of migration in unbounded medium in Chapter 3 [148]. Instead, turns are slower and caused by pseudopod meandering. For a confined medium, though, turns are much more common as well as more severe as obstacle force pseudopods to strongly detour, or as *de novo* pseudopods form on another area of the cell. As seen in Figure 4.15A, even a small change in the matrix porosity ($\phi = 0.92$) was able to eliminate persistent motion. As a more quantitative measure for gauging persistence, Equation 4.1 was used.

$$\overline{\Delta\theta} = \frac{1}{L}\int_L \theta_i \, dL \tag{4.1}$$
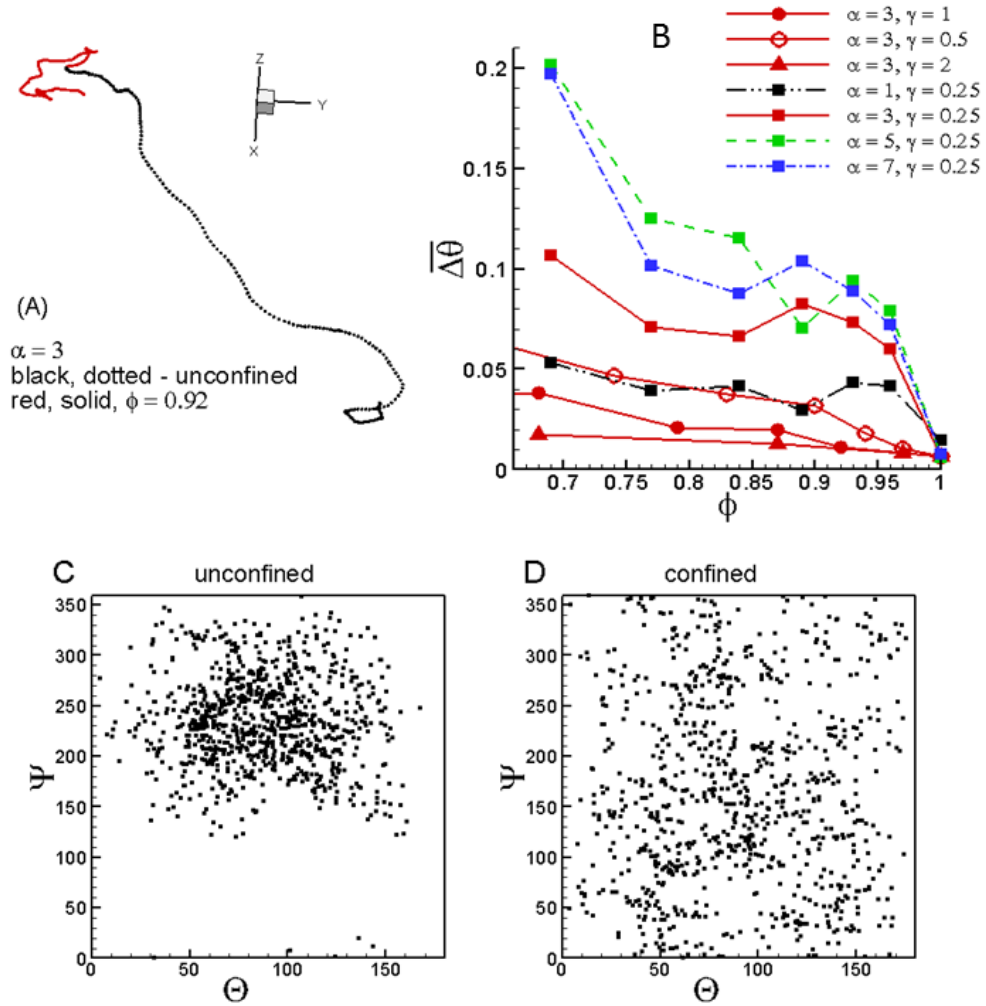
Figure 4.15: Cell motility in confined ($\phi < 1$) versus unconfined ($\phi = 1$) medium. **(A)** 3D cell trajectories in unconfined medium (black, dotted curve) and confined medium ($\phi = 0.92$; red, solid curve). **(B)** Total directional change $\overline{\Delta\theta}$ in cell trajectory as a function of matrix porosity for different α and γ. **(C-D)** Pseudopod directionality is quantified by the angular position of pseudopod tips using the spherical coordinates Ψ (0 to 2π) and Θ (0 to π) for the unconfined and confined ($\phi = 0.87$) domains, respectively, with $\alpha = 5$ and $\gamma = 1$. Reproduced from [103] with permission of the Royal Society of Chemistry.

In Equation 4.1, the total directional change over the cell centroid trajectory was found by integration, where L is the trajectory length, and θ_i is the incremental directional change between subsequent positions. Then for a purely persistent cell, $\overline{\Delta\theta} = 0$. Results are plotted in Figure 4.15B against the matrix porosity for several values of deformability and obstacle

size. For an unconfined medium ($\phi = 1$), $\overline{\Delta\theta}$ is noted to be very small as the unbounded trajectory in Figure 4.15A indicates. $\overline{\Delta\theta}$ is also seen to increase with decreasing matrix porosity, implying a loss of cell persistence as more obstacles are introduced into the domain. Decreasing obstacle size also results in higher values of $\overline{\Delta\theta}$. Finally, $\overline{\Delta\theta}$ is seen to increase with increasing cell deformability, due to shorter pseudopod lifetimes and larger cell speeds.

In Chapter 3 and our previous study [148], cells with a larger diffusivity ratio β were shown to generate pseudopods only near the cell anterior in unconfined medium. Even in the absence of an external cue or chemotactic signal, subsequent bifurcations continued to occur in the same region on the cell, resulting in a polarized, persistent motion. In the case of a confined matrix geometry, however, *de novo* pseudopods are prevalent, and are seen to increase in proportion as confinement is increased. *de novo* pseudopods are prone to appear in any area on the cell and without any preference due to a reset noise and activator-inhibitor system. To quantify the pseudopod directionality, the angular position of pseudopod tip normals is calculated using the spherical coordinates Ψ and Θ as seen in Figure 4.15 C and D. They are absolute coordinates tied to the Eulerian cartesian system as a reference frame, where Ψ is the angle of the pseudopod normal projected onto the xy plane relative to the x-axis, while Θ is the angle relative to the positive z-axis. And since protrusive force is generated by the pseudopod, the cell will move in the resultant direction. Each point represents a specific pseudopod and time step. For the cell in an unconfined environment (Figure 4.15C), a tight grouping of points is seen, indicating the pseudopods are focused and generated in a similar direction over the entire solution time. The mechanism for pseudopod focusing was outlined in Chapter 3 and our earlier work [148],

and is caused by the initially polarized cell pseudopods converging and bifurcating before they can sufficiently meander to another point on the cell, thus maintaining the angular bias seen in Figure 4.15C. The case of migration with obstacles present is shown in Figure 4.15D, in which a uniformly scattered distribution of points is seen across the plot. This indicates pseudopods are scattered in all directions over the cell, again due to the activator-inhibitor being frequently reset due to obstacle collisions, and the appearance of *de novo* pseudopods which change cell direction. As evident by Figure 4.15A and D, even a small decrease in porosity is enough to break the cell polarity, and as a result, the persistence of the cell through the matrix.

4.2.7   Flow Field

The instantaneous fluid motion of the migrating cell is now considered. Due to dynamic pseudopod behavior and cell deformation as well as the presence of obstacles, complex and transient fluid flow develops both inside and outside the cell. In general, the flow patterns seen in a confined medium are similar to those of a migrating cell in unbounded medium as seen in Chapter 3 [148]. A pseudopod will cause a streaming flow inside the cell from the main body into the growing appendage. The surrounding fluid is also entrained by the pseudopod, and pushed in the direction of motion. The reverse effect is seen during pseudopod contraction, where streaming flow will exit the pseudopod and move into the main cell body. During pseudopod protrusion and retraction, complex vortical patterns are observed. Within the literature on microswimmers exists characterizations of the pusher- and puller-type mode depending on the mechanism used to achieve motility. Pushers repel fluid away from the cell along the axis of movement and attract flow towards the cell along its sides. Pushers are rarely seen, and if so, only during

the initial transient when opposing pseudopods form. Puller motion is the opposite of pusher motion. Fluid is pulled in along the direction of migration and repelled along the side. Pullers are seen more often in simulations, but true characterizations are difficult to make due to highly deformed shapes and pseudopod dynamics.
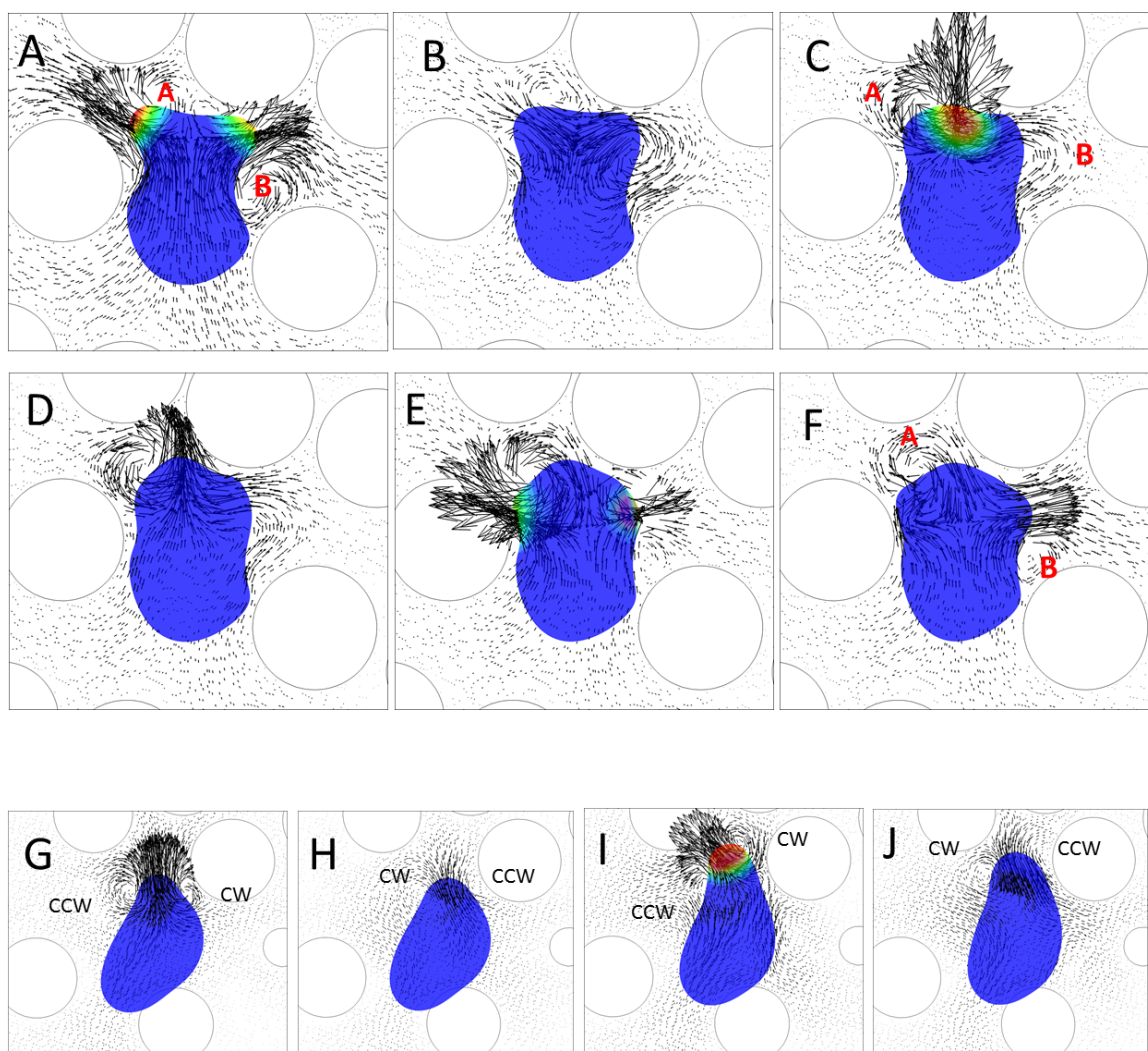
Figure 4.16: Flow patterns for a cell migrating through a matrix. **(A-F)** Shows a sequence of flow patterns for $\alpha = 3$, $\phi = 0.54$, and $\gamma = 1$. Vortical patterns can be seen at locations **(A-B)** marked in red. Velocity vectors are drawn in the plane passing through the cell center. Dimensionless times are 0.80, 1.05, 1.15, 1.20, 1.35, and 1.40. **(G-J)** Shows another sequence with a probing event for $\alpha = 5$, $\phi = 0.68$, and $\gamma = 1$. Clockwise and counterclockwise vortices are marked by "CW" and "CCW," respectively. Dimensionless times are 6.80, 6.95, 7.65, and 7.90. Reproduced from [103] with permission of the Royal Society of Chemistry.

Additional flow features which are not seen in unbounded flow have been observed for a cell migrating in a confined environment. Vortices which alter direction are seen during pseudopod growth and retraction. Figure 4.16A through F illustrates these events, where the matrix porosity is $\phi = 0.54$. In (A), two clockwise vortices (marked by A and B) form during the growth and bifurcation of a pseudopod. In (B), the pseudopods are terminated due to obstacle closeness, resulting in both vortices changing to a counter-clockwise direction. As new pseudopods form in (E) and (F), the vortex directions change once again to clockwise. These dynamics are cause by cycles of obstacle-induced pseudopod termination and subsequent *de novo* pseudopod formation, and are therefore absent in the case of unbounded flow. Another example which shows alternating vortices during a probing event is shown in Figure 4.16G through J. As the pseudopod cyclically protrudes and retracts, the clockwise and counter-clockwise vortices continuously change direction.

4.2.8 Additional Considerations

(A) Viscoelastic Membrane

In previous works, an accurate model for a viscoelastic cell membrane was developed [95]. Viscoelastic behavior was resolved using a Kelvin-Voigt model, which was mentioned in Chapter 2 but is repeated below for convenience. The total membrane stress is thus the sum of the elastic and viscous stresses as seen in Equation 2.15.

$$\tau = \tau^e + \tau^v \tag{2.15}$$

Elastic stresses were given by Equations 2.3 and 2.4, while the viscous stress is expressed as follows, where μ_m is the membrane shear viscosity, $\boldsymbol{D}$ is the strain rate tensor, and $\boldsymbol{I_S}$ is the surface projection tensor.

$$\tau^v = 2\mu_m \left[\mathbf{D} - \frac{1}{2}tr(\mathbf{D})\mathbf{I}_S \right] \qquad (2.16)$$

Numerical implementation is then performed to find the stress in terms of strain history using a time-convolution integral. We have performed simulations using a dimensionless membrane viscosity of $\mu_m/\mu_0 R = 0$, 1, and 10, where zero is the case of an elastic membrane. Figure 4.17 shows the dimensionless average cell speed against the dimensionless membrane viscosity, showing a small increase with viscosity, while the RMS fluctuation decreases slightly. The cell persistence, found as $\overline{\Delta\theta} = 0.026, 0.021$, and 0.020 in order of increasing viscosity showed similar trends. General motility behavior was seen as similar, while obstacle-mediated dynamics such as freezing and probing were still observed.
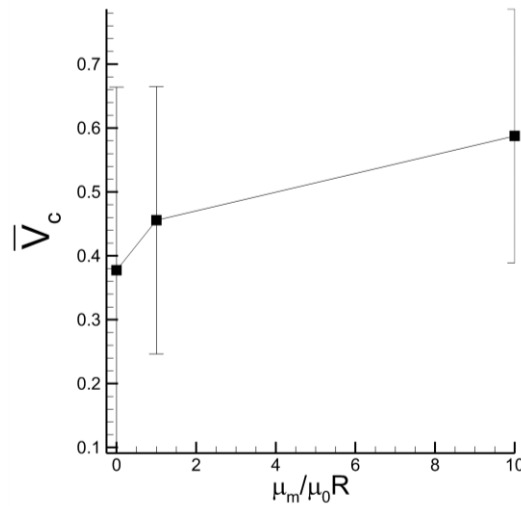
Figure 4.17: Influence of membrane viscosity on average cell speed. Variables are defined in main article. Error bars are RMS quantities. Reproduced from [103] with permission of the Royal Society of Chemistry.
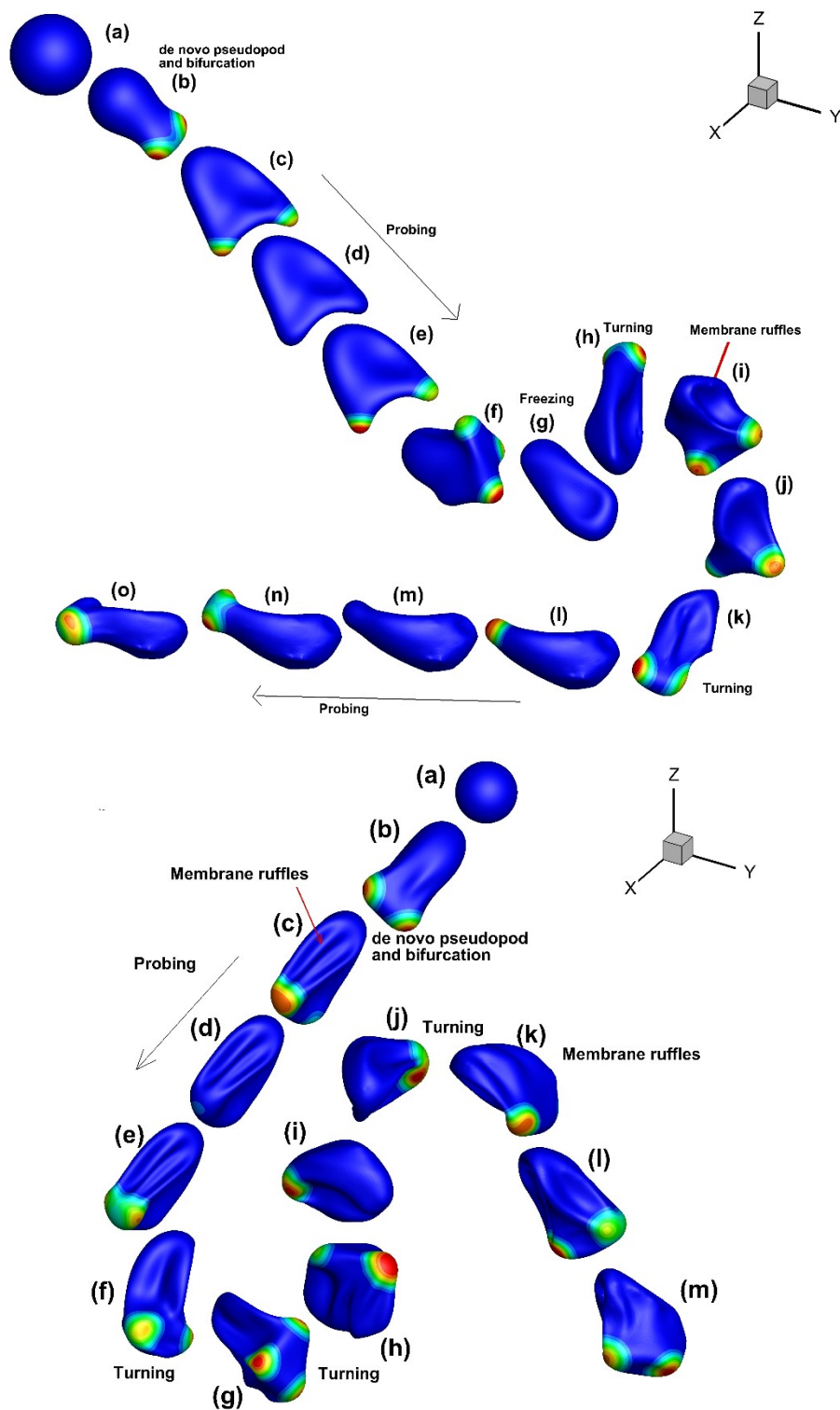
Figure 4.18: Sequences showing the effect of a viscoelastic membrane on cell motility. $\mu_m/R\mu_0 = 1$ **(top)** and 10 **(bottom)**. Similar motile dynamics are observed as for elastic membrane. Reproduced from [103] with permission of the Royal Society of Chemistry.

Viscosity is seen to stiffen the cell membrane, causing ruffles which are artifacts of former pseudopods or deformed membranes. Sequence plots are shown in Figure 4.18 for two cases of membrane viscosity. Because these ruffles also exhibit high curvature, they are also instigators of more frequent bifurcations as previously described. As a result, a larger number of pseudopods is generated, leading to a slightly higher cell speed. Note that the membrane deformation time scale is $R\mu_0/G_s \sim \mu_m/G_s \sim 10^{-3} - 10^{-2}$, while the activator-inhibitor diffusive time scale is R^2/D_3 or $R^2/D_1 \sim 1$. This means the membrane quickly responds to the evolving Turing patterns even when viscosity is large, so the cell behavior widely depends on activator-inhibitor dynamics.

(B)   Variation of Bending Rigidity
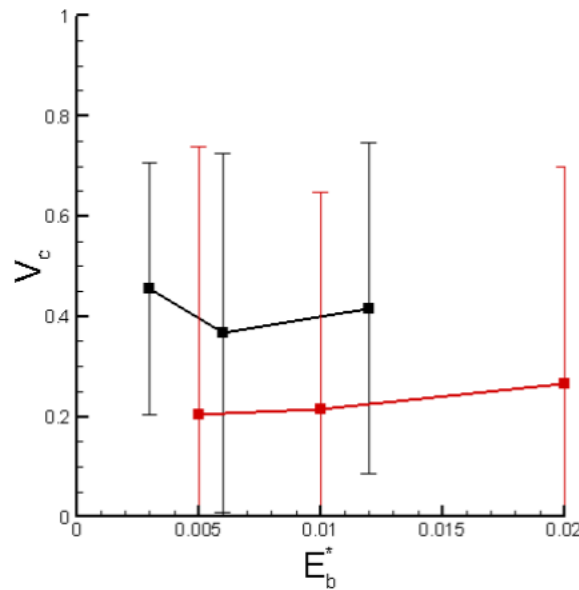
Figure 4.19: Average cell speed (**black**, $\gamma = 1$; **red**, $\gamma = 0.5$) as a function of dimensionless bending rigidity E_b^*. Error bars represent RMS velocity fluctuations over time. Reproduced from [103] with permission of the Royal Society of Chemistry.

The nonlinear constitutive model (Equation 2.1) which considers membrane deformation is prone to buckling [95], while pseudopod dynamics caused by protrusive forces can generate ruffles or kinks of high curvature. To protect against this, membrane bending is added. Dimensionless bending stiffness is scaled as $E_B^* = E_B/R^2 G_s$, where the bending stiffness $E_B \sim 1 - 9 \times 10^{-19}$ J [90,93]. E_B^* was varied in simulations from $0.003 - 0.020$, where the average speed was found and plotted in Figure 4.19. Both cell velocities and persistence were not seen to deviate significantly. Cell behavior was observed to be similar, while obstacle-mediated dynamics like probing and freezing were still observed.

(C)   Cutoff Distance for Cell-Obstacle Interaction

As noted in section 4.2.2, when an active pseudopod gets nearer than two Eulerian mesh points to an obstacle surface, the activator-inhibitor system is reset, and a repulsive force is generated to prevent the cell from collapsing onto the obstacle and becoming stuck. The two-point cutoff is not arbitrary, however. It is also used to distribute membrane forces over a finite width using the Dirac delta function outlined in Equation 2.50. For the immersed-boundary method used here, the delta function is modeled as a cosine function which spreads over two grid points on each side of the membrane. This is the fundamental reason why the two-point cutoff is used. Other cases were still examined, though. Cutoff distances of 1, 1.5, 2.5, and 3 grid points were simulated. No major differences were seen except for the case using 1 grid points, where the cell surface mesh collapses due to a larger lubrication force proportional to the inverse distance apart cubed.

(D)   Cylindrical Obstacles

Although arrays of spheres were the only extracellular matrix geometry modeled in this chapter, the robustness of our model allows for any form of complex geometry. One such variant is an array of cylinders, briefly discussed here, but further expanded upon in Chapter 5. A limited number of simulations has been performed as seen by Figure 4.20, which shows several frames of a migrating cell through the aligned field of obstacles in addition to a dimensionless speed plot as a function of matrix porosity. Data from sphere-based simulations is also included in the plot for comparative reasons. Cell behavior and pseudopod dynamics are all qualitatively similar to the case of spherical obstacles. Average cell speeds also show no significant difference. It is noted that the cylinder velocities show unsmooth variations, which is purely due to the limited number of runs performed. More cylindrical obstacle-based migration analysis will be shown in Chapter 5.
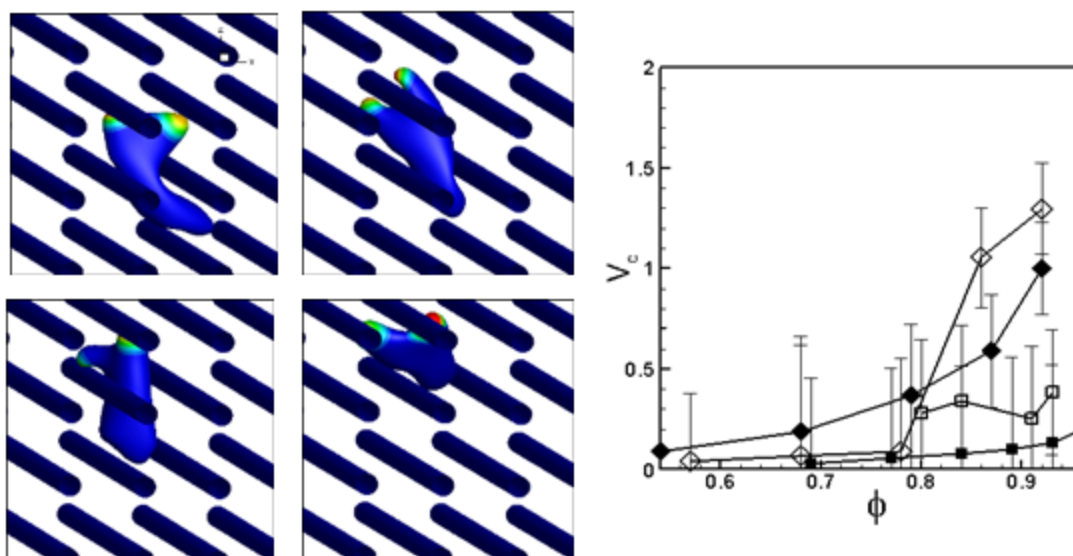
Figure 4.20: Influence of cylindrical obstacles. Snapshots show a sequence of motility. The average cell speed is compared for cylinders (open symbols) and spheres (filled symbols) for $\gamma = 1$ (diamonds), and 0.25 (squares). Reproduced from [103] with permission of the Royal Society of Chemistry.

4.3 Summary

A three-dimensional multiscale and multiphysics computational model coupling fluid mechanics, solid mechanics, and a dynamic pseudopod-generating pattern formation model was presented to simulate amoeboid migration through a porous extracellular space in the absence of adhesive interactions. Predicted cell shapes were found to be similar to those observed by experiment. Extreme deformation was seen as cells squeeze through, and weave around narrow spaces between obstacles. Migration speeds were seen to align with experimentally determined speeds in multiple works. The effect of cell deformability, matrix porosity, and obstacle size were studied, with each property strongly influencing cell behavior and dynamics. Cell migration was completely hindered as these parameters dropped below certain limiting magnitudes, to which phase diagrams were constructed. This conclusion is supported by experiments, where soft immune cells can move over an order of magnitude faster through tissue than stiffer fibroblasts. Interesting cell dynamics are predicted, such as freezing, probing, tug-of-war, and doubling-back, which have all been observed within the literature. These dynamics are not seen in unbounded flow, and are seen to appear in greater amounts as confinement is increased. Since no chemical signaling mechanisms are used in our model, this suggests that mechanical stimulation could also produce these dynamics. Persistent unidirectional motion seen in migrating cells in unbounded flow is prevented in the presence of obstacles, where cells must adopt a zig-zag type of migration, a major change in cell dynamics. Because active pseudopods too near an obstacle cause an activator-inhibitor reset, *de novo* pseudopods are seen to become more common, also increasing in frequency with higher confinement. While pseudopod lifetimes are seen to decrease with increasing confinement, new pseudopods help the cell

find a new direction to migrate in. On average, less pseudopods are seen as matrix porosity decreases. Fluid interaction was also studied by investigating complex patterns and dynamics seen in fluid velocity vector fields. Vortices generated by membrane extensions and retractions are seen to change directions. These attributes were not seen in unbounded flow, and can be predicted to drastically alter the distribution of chemicals and proteins within a confined geometry. To summarize, a strong coupling between membrane deformability, matrix porosity, and obstacle size was observed. New insights for amoeboid migration through confined matrix geometry were made, setting the stage for more complex cell modeling, and the results which will be unearthed.

Chapter 5

Pseudopod-Driven Migration of an Amoeboid Cell in Various Extracellular Matrix Geometries with Weak Adhesion

Amoeboid cell migration is accomplished through the use of pseudopods, or cylindrical membrane extensions which protrude, bifurcate, and retract dynamically. Cells exhibiting pseudopod-driven locomotion hold significant importance, particularly within the human body, as both immune cells and metastatic cancer cells use pseudopods, among others. The modeling of amoeboid locomotion is a complex and multiscale process, where large membrane deformations, cell surface biochemistry, and both cytosolic and extracellular fluid interactions must be considered. Furthermore, cells are often confined inside the extracellular matrix (ECM), a heterogenous, porous, fluid-filled medium. Adhesive properties of the cell and underlying substrate add another layer of complexity. In this work, we present a three-dimensional computational model of pseudopod-driven amoeboid migration with weak adhesion through various matrix geometries: aligned cylinders, three-dimensional lattice, and arrays of spheres. Adhesion is implemented using a modified Bell model. The effect of cell deformability, adhesive strength, and matrix geometry on amoeboid cell migration is studied. Cell shapes qualitatively similar to experimental images are observed, while several types of cell dynamics, including a gliding-type mode, are witnessed. Weak adhesion is shown to have little effect on average cell speed, while the degree of helpfulness that adhesion engenders is quantified. Finally, bond quantity is seen to vary across matrix geometry and membrane deformability, while the average bond

distribution reveals trends in bond formation. Results presented here show a strong effect between adhesive dynamics, cell deformability, and matrix geometry, providing valuable insight towards amoeboid migration within the body.

5.1 Introduction

In this work, pseudopod-driven amoeboid migration is simulated through three distinct extracellular matrix geometries, while discrete adhesive bond dynamics are considered between the cell and surrounding matrix. As has been discussed, amoeboid motility is a major migratory phenotype, especially within the human body, where an assortment of biologically-significant processes are carried out through pseudopod-generated activity. Biological details of pseudopod growth and retraction in addition to the cell motility cycle were discussed in previous chapters and are not reemphasized here.

Generally speaking, when not freely suspended in a fluid medium [2-3,113], cell interaction with a substrate is necessary in two- or three-dimensions. Transmembrane adhesive proteins, such as integrins, form connections with corresponding surface receptors, resulting in discrete bonds between the cell and its environment [150]. *in vivo* cell migration rarely occurs in two dimensions, however. Instead, motile cells often need to navigate through complex three-dimensional tissues of varying porosity, pore size, and fiber orientation [36,39,151]. This cellular scaffold is known as the Extracellular Matrix (ECM), which provides a structure in which cells can anchor to and function on. The composition of the ECM is highly diverse, but principally speaking, structural collagen fibers are embedded in a gel-like polysaccharide fluid. Additional fibers are incorporated into the ECM, such as elastin which gives tissue its resiliency, and fibronectin, which provides adhesive bonding sites between cells, matrix, and fluid. Cell behavior can be

heavily influenced by ECM properties, including alignment, stiffness, and elasticity [57]. Fibroblasts, for instance, can exhibit an adhesion-dependent polarized mode or an adhesion-independent, highly deformable configuration based on matrix properties [59]. These and other mesenchymal-type cells rely on strong adhesion via integrins clustered into focal adhesions, and an ability to degrade the matrix using proteases. Amoeboid properties, on the other hand, are significantly different. Amoeboid cells maintain a non-polarized morphology, taking advantage of high membrane deformability to squeeze through gaps in tissue. Amoeboid cells have also been observed to migrate with no adhesion [50], or weak adhesion using a diffuse amount of adhesive proteins spread out across the cell membrane [20]. The latter case is the subject of this chapter.

Considering the above discussion, the objective of this work is to present a fully three-dimensional computational modeling study of pseudopod-driven amoeboid migration with weak adhesion through several confined matrix geometries. Several prior works have explored cell locomotion through two- and three-dimensional geometries while modeling adhesion. Zaman *et al* developed a computational cell migration model in three-dimensional matrices using a force-based dynamics method [31]. Adhesive forces were implicitly set as being proportional to receptor and ligand concentrations, and the matrix modulus of elasticity. Schlüter *et al* used a force-based cell migration model in two-dimensional matrices of varying alignments, with adhesion force proportional to cell speed [34]. Ordered geometries were seen to allow for greater persistence. Copos *et al* studied two-dimensional cell spatiotemporal adhesion patterns using a force-balance approach and linear springs to model adhesion [33]. Amoeboid cells were shown to have extension and contraction events from nonuniformly spaced adhesions. Using the finite element method,

Sakamoto *et al* created a two-dimensional axisymmetric cell model to better understand transitions in cellular migration modes, modeling adhesion-complex density with an advection-reaction equation, and adhesive force proportional to surface velocity and adhesion-complex density [30]. Amoeboid cells were found to have weaker adhesion capabilities, and more frequent transitions between elongation and retraction stages. Cirit *et al* studied the interplay between adhesion and protrusion at the leading edge of a cell, modeling the densities of nascent and stable adhesions, and myosin using coupled ODEs [14]. Optimal leading-edge protrusion was seen at intermediate ECM densities. Shao *et al* developed a phase-field two-dimensional cell migration model with discrete adhesion sites characterized by gripping or slipping modes [32].

Zhu and Mogilner modeled two-dimensional cell migration through extracellular matrix using an elastic spring-node network, where protrusion and retraction of the cell membrane was modeled as expanding and shrinking networks [152]. Discrete adhesions were formed based on distance considerations, and eliminated by a constant detachment rate. An amoeboid mode was observed, which showed little dependence on adhesion detachment rate or leading-edge growth and posterior contractility, while ECM size had a slight effect. Finally, Moure and Gomez developed a three-dimensional amoeboid migration model using a diffuse-domain approach, considering actin and myosin dynamics within the cytosol, and activator dynamics on the cell membrane using a reaction-diffusion equation [10-11]. Adhesion was considered as a summation between drag and punctual spring-based adhesions which were randomly formed.

Since adhesion has the capacity to influence cell behavior as strongly as the extracellular matrix, a detailed three-dimensional study investigating the effect of adhesion

on amoeboid cells merits attention. A weak, diffuse model for adhesion dynamics is implemented into the existing amoeboid cell framework. Adhesive strength is varied in order to investigate the reliance of adhesion on the amoeboid morphology.

5.2 Results

5.2.1 General Motility Behavior

Migration of an amoeboid cell was simulated through three independent geometries: arrays of spheres ($\phi = 0.68, \gamma = 1$), arrays of aligned cylinders ($\phi = 0.68, \gamma = 0.5$) and ($\phi = 0.82, \gamma = 0.5$), and a three-dimensional lattice ($\phi = 0.68, \gamma = 0.5$). The sperical geometry uses $\gamma = 1$ because, for an equivalent porosity at $\gamma = 0.5$, the gaps between obstacles would be roughly twenty percent of the cell radius, which would completely inhibit cell migration. Therefore larger radius spheres are used. Two cylindrical geometries are simulated due to the current state of results available. Our reasoning for choosing these distinctive geometries is as follows. Arrays of rigid spherical obstacles follows our earlier work [103], in which non-adhesive amoeboid migration was modeled. Spheres served as an arbitrary geometry where variations in porosity and obstacle size could be controlled. Furthermore, cell migration through circular geometries – a two-dimensional equivalent of spheres, has been modeled prior by Elliott *et al* [7] and Hecht *et al* [29]. In previous works, cylinders have been used to represent interstitial collagen filaments within the ECM [10-11,34]. In addition, aligned filaments can be found in several parts of the body, such as in collagen networks [19] or between muscle or nerve fibers [57]. Simulations utilizing cylinders of random orientation have not been suitably completed to generate results, and therefore are not presented in this work. Additionally, more complicated geometries and models for deformable matrices are to be considered in future works. The three-

dimensional lattice consists of arrays of aligned cylinders oriented in the three principal cartesian directions. This geometry therefore acts as a scaffold for cells, as witnessed by tissue-engineering studies [155] and other works [19,156]. We place high importance on the three-dimensional lattice, since physical properties such as filament diameter and porosity can affect cell survival and differentiation within artificial or bio-inspired scaffolds. Cell migration simulations can therefore help determine the optimal matrix properties suitable for cell differentiation and prosperity.
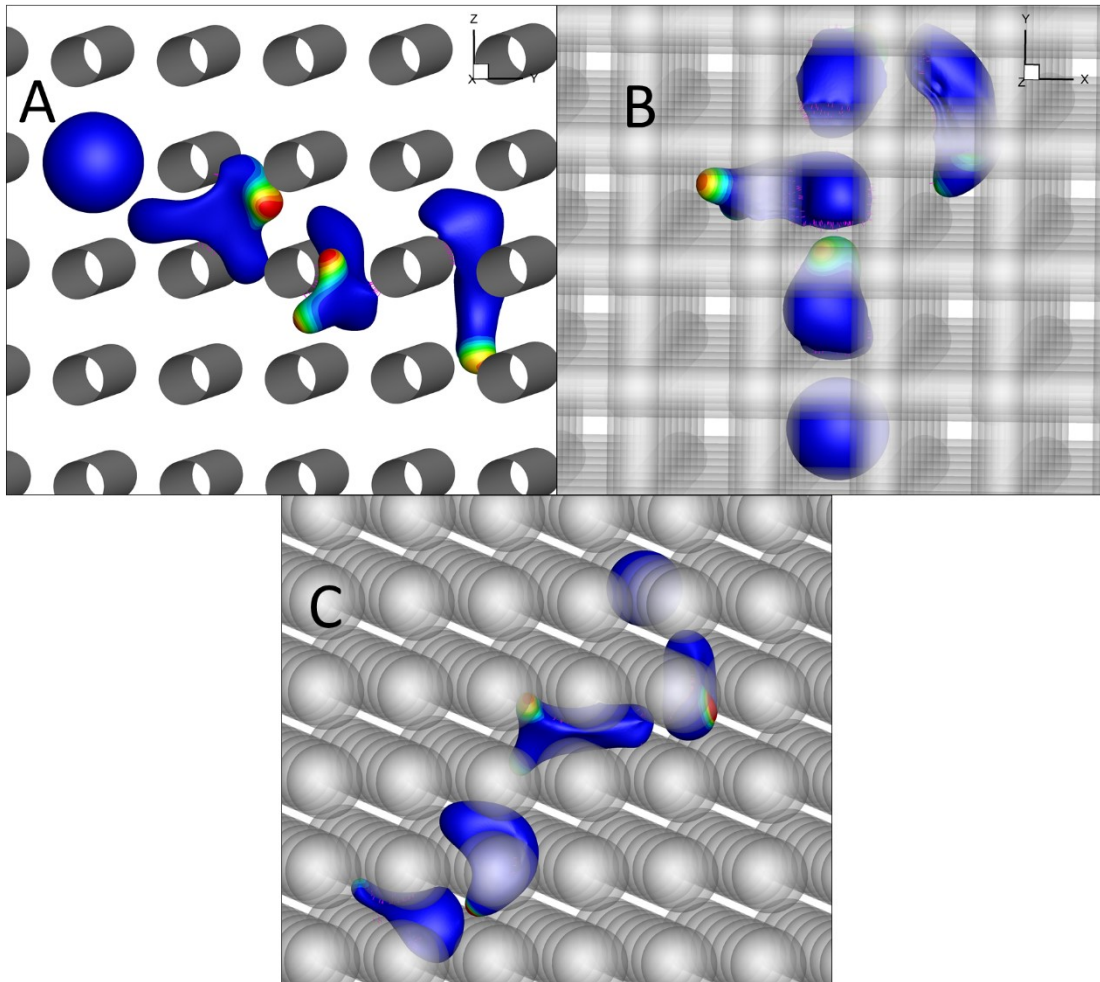
Figure 5.1: Sequences showing amoeboid migration through **(A)** Aligned cylinders for $\alpha = 7$, $\phi = 0.83$, $\gamma = 0.5$, and $\sigma = 2$. **(B)** Three-dimensional lattice for $\alpha = 4$, $\phi = 0.68$, $\gamma = 0.5$, and $\sigma = 1$. **(C)** Array of spheres for $\alpha = 7$, $\phi = 0.68$, $\gamma = 1$, and $\sigma = 1$. Bonds between the substrate and cell are shown as pink lines.

Figure 5.1 illustrates a sequence of an amoeboid cell migrating through each type of geometry in the presence of adhesion over time. Since adhesion can trigger gene regulation or changes in cell behavior, a thorough analysis is warranted [161]. Adhesive bonds are represented by individual pink lines connecting the cell to the adjacent substrate. The cell is first initialized as a sphere, while the activator-inhibitor system is set to unity across the cell. Through perturbations of the noise term ϵ, a Turing instability soon develops, causing a locally-induced protrusion in the region of the instability. This *de novo* pseudopod extends outward until the activator concentration of the underlying instability abates, or until the pseudopod bifurcates into two separate instabilities. A decay in activator concentration will lead to a pseudopod retraction event, while a splitting of the instability will result in the bifurcation of the parent pseudopod into two daughter pseudopods. Additionally, a pseudopod may also get too near an obstacle, forcing a reset of the activator-inhibitor system to unity, and the noise across the cell to zero. This step was determined to be necessary in order to prevent the cell from becoming stuck on a convex obstacle surface, and has been discussed thoroughly in Chapter 4 [103]. A *de novo* pseudopod will then form somewhere on the cell, which continues its migration. Large deformations are seen in Figure 5.1 for each type of geometry. For migration through aligned cylinders, the cell becomes highly polarized as it migrates, likely because of the amount of confinement imposed on the cell. For three-dimensional lattice (Figure 5.1B), membrane ruffling is seen, due to adhesive pulling and the cell migrating through a square-shaped hole of smaller equivalent diameter. Finally, in the sphere geometry (Figure 5.1C), large deformations are imposed on the cell from multiple spheres as it migrates through narrow gaps. In addition to seeing dynamics such as freezing, probing, doubling-back, and

tug-of-war, several new dynamics are seen. Two new modes are described as gliding and posterior retraction relative to the cell body.
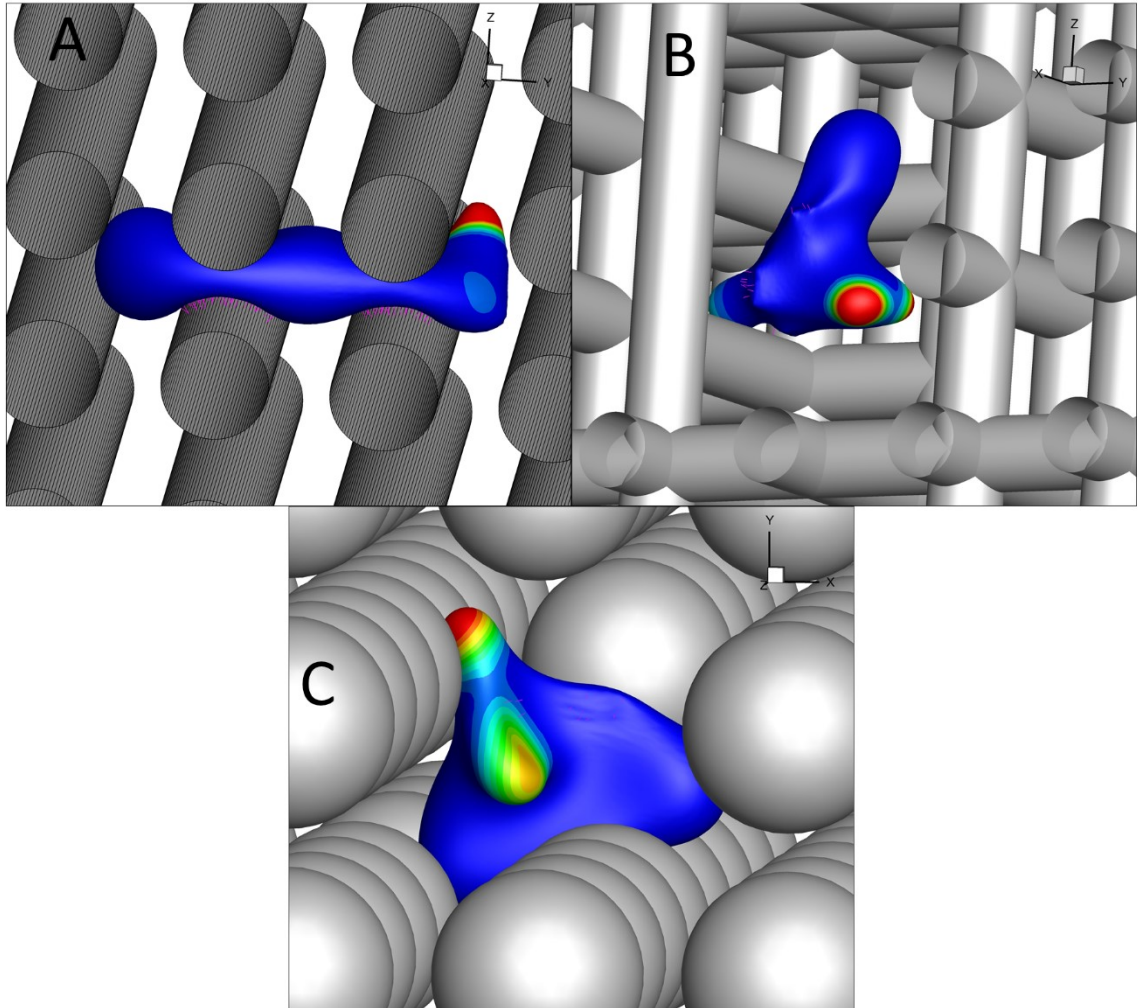
Figure 5.2: Examples of highly complex cell shapes predicted in various matrix geometries. Some matrix obstacles have been removed for clarity. **(A)** Shows a highly polarized cell stretched between several cylindrical obstacles for $\alpha = 7$, $\phi = 0.68$, $\gamma = 0.5$, and $\sigma = 1$. **(B)** Shows a cell migrating through the three-dimensional lattice for $\alpha = 7$, $\phi = 0.68$, $\gamma = 0.5$, and $\sigma = 2$. The cell membrane is seen to bulge slighly where adhesive bonds have formed, indicating the presence of a traction force. **(C)** Shows a cell attempting to squeeze through a narrow gap between spheres for $\alpha = 7$, $\phi = 0.68$, $\gamma = 1$, and $\sigma = 1$.

A survey of cell shapes encountered is presented in Figure 5.2 for each geometry. In the aligned cylinders matrix (Figure 5.2A), the cell can be seen as highly slender and

polarized when cell deformability is high. Adhesive connections on four distinct cylinders are the reason why a normally rounded and non-polarized cell appears as such. The adhesive bonds act like weak anchor points, which hold the cell membrane fixed at that location until they are broken by the force from a protruding front. Cell shapes for three-dimensional lattice and the spherical array (Figure 5.2B and C) are subjected to different forms of confinement, and therefore are shorter and less polarized. Furthermore, each cell is shown to conform to the shape of the void space of the matrix. In the three-dimensional lattice, for instance, the cell may be forced into a square-like configuration, while pseudopod extensions are thinner than otherwise seen in the array of spheres in order to penetrate the narrow gaps between obstacles. Additionally, membrane pulling can be seen in the lattice geometry, imparted by adhesive bonds with a spring constant of $\sigma = 2$.

Interesting cell dynamics have been observed as each cell migrates through its corresponding matrix. In summary, we label these behaviors as tug-of-war, doubling-back, freezing, probing, gliding, and rear cell retraction. Because the first four listed dynamics have been extensively mentioned in Chapter 4, they are only discussed briefly here. The reason for each dynamic, with the exception of tug-of-war, is due to a reset of the activator-inhibitor system when an active pseudopod gets too near an obstacle. Different dynamics are seen depending on how the activator-inhibitor system responds. In doubling-back, a *de novo* pseudopod will form on the cell posterior, forcing the cell to turn around. In freezing, no viable *de novo* pseudopods will form for a brief period of time, forcing the cell to remain inactive. And in probing, the deactivated pseudopod will independently form on the same retracting extension continuously, helping the cell through a constriction with each cycle.

In tug-of-war, two pseudopods wrap around an obstacle, which becomes stuck until one of the competing pseudopods decays.
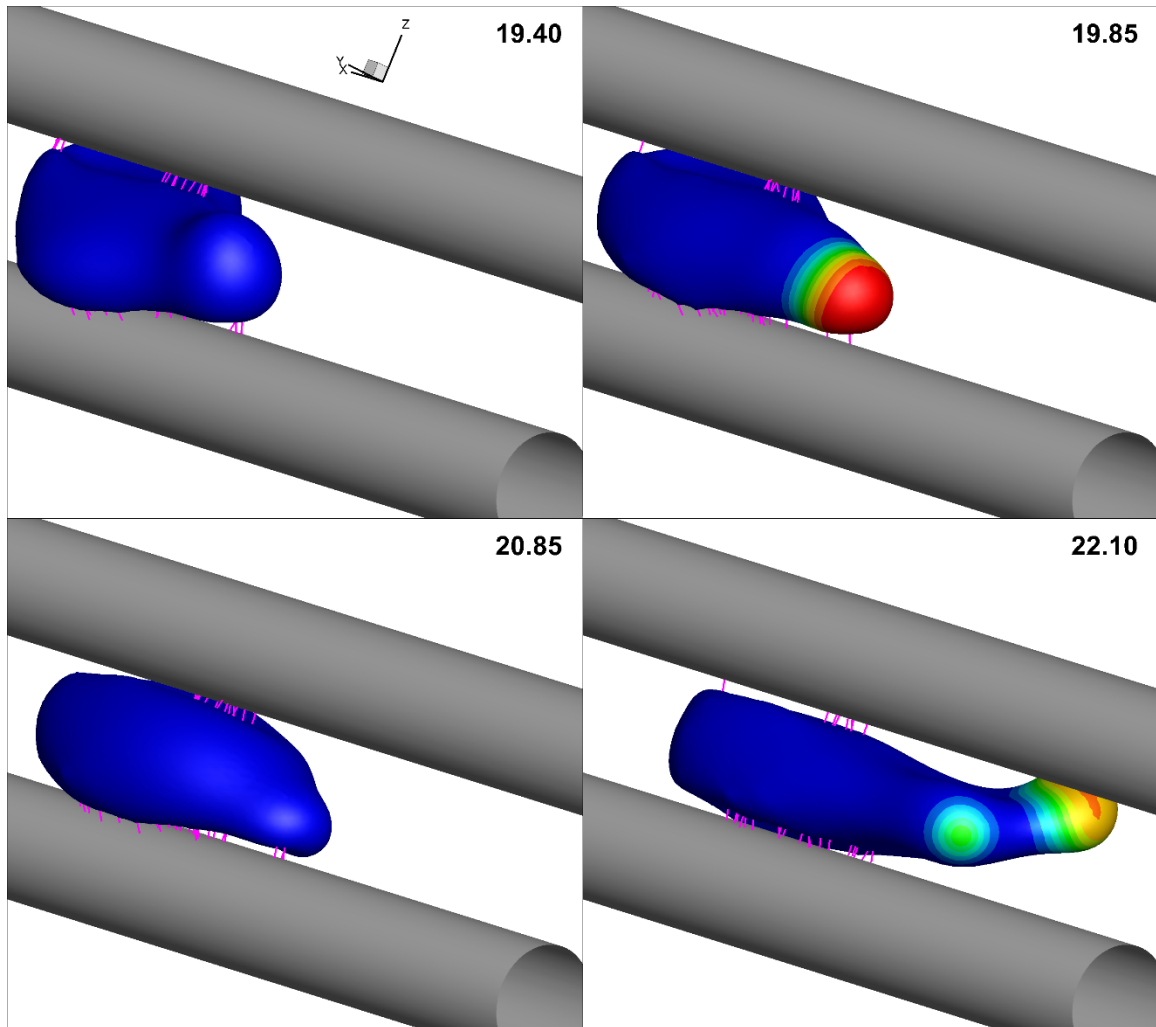
Figure 5.3: An amoeboid cell exhibiting gliding type behavior in the aligned cylinder geometry for $\alpha = 5$, $\phi = 0.83$, $\gamma = 0.5$, and $\sigma = 1$. All but the necessary cylinders needed to illustrate the gliding dynamic have been removed for clarity. Discrete bonds are shown as pink line segments. Dimensionless times for each frame are displayed.

We have also observed a type of behavior identified as gliding or skipping in the literature [28,160]. As seen in Figure 5.3, adhesive bonds are established between the cell membrane and the adjacent matrix surfaces. Because the cell is in the process of migrating,

bonds are likely to form near any area of close contact, while existing bonds in the rear of the cell are likely to be broken as the cell pulls away. A natural result of these processes is a cycle of bonds forming in the front and breaking in the rear. We call this behavior gliding, since adhesion does not appear to inhibit cell progress. Instead, the same area on the cell continuously forms bonds, which are then broken as the cell moves forward, after which the aforementioned area on the cell forms new bonds. As in the case of Figure 5.3, probing is seen as the cell moves forward. Gliding has only been seen in the aligned cylinder geometry, most likely because of the uninterrupted paths available, as well as a lack of curvature in the longitudinal direction, which would otherwise pull the cell towards the curving geometry. However, it is possible for gliding to occur in the three-dimensional lattice geometry, although at reduced intervals because of higher confinement. Reference [28] described lymphocytes and neutrophils as having a fast gliding type of motion defined by short-lived and weak interactions with substrates, which agrees well with our description. Additionally, Bastounis *et al* described a similar "skipping" mode in which a cell forms numerous, diffuse and weak traction adhesions along the cell length [160]. Adhesion did not appear to aid or inhibit cell migration during the gliding mode, but instead may have kept the cell aligned as in the case of contact guidance [151].

Another interesting dynamic is seen when the cell posterior retracts relative to the main cell body as illustrated in Figure 5.4. As the cell approaches a narrow gap between two aligned cylinders, its leading edge adheres to both obstacles, helping to guide the cell. Further protrusion forces the front half of the cell through the constriction. A bifurcation occurs, where each pseudopod protrudes in opposite directions and adheres to its nearest matrix surface. Now shaped like an inverted "T", the cell begins to retract its rear as

sustained pseudopod protrusion forces the cell to advance. However, the cell front, center, and rear are seen to move at different speeds. As seen in Figure 5.5, the rear-cell speed briefly exceeds the center-cell speed, resulting in a net contraction of the cell rear relative to the rest of the cell. We note that while no explicit contractility model is present in this work, leading-edge protrusion is sufficient enough to induce a pulling force in the cell posterior [33]. Furthermore, cells lacking Myosin II were shown to exhibit comparable traction forces on a substrate, generating sufficient friction for movement [162]. These results indicate that contractility is a tool used by the cell to help migration, but is not absolutely required.
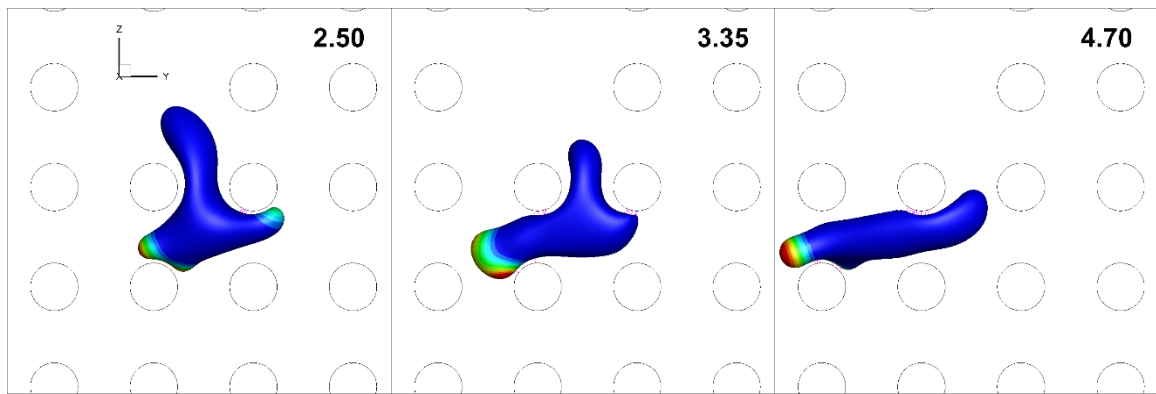
Figure 5.4: Example of the significant rear-cell retraction which occurs during migration in the presence of adhesion for $\alpha = 7$, $\phi = 0.83$, $\gamma = 0.5$, and $\sigma = 2$. Dimensionless times are displayed.
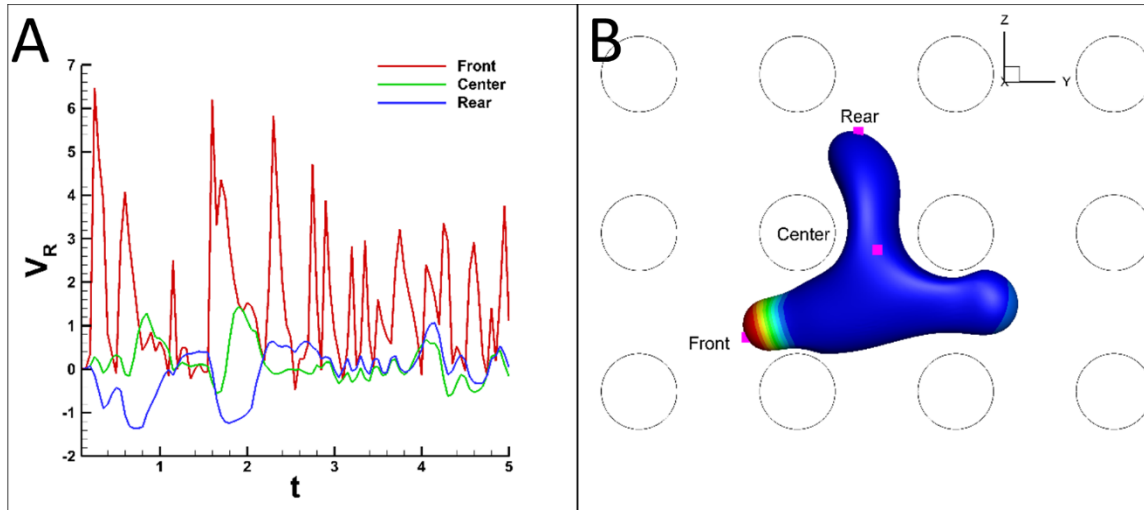
Figure 5.5: **(A)** Relative speeds of three points selected on the migrating cell relative to the average cell migration speed: front, center, and rear. The rear-cell speed is seen to exceed the center-cell speed briefly during the relative contraction. **(B)** The amoeboid cell marked by each point at a dimensionless time of 2.9.

5.2.2 Adhesion-Induced Effects

The effect adhesion has on amoeboid cell migration through various extracellular matrix geometries is now considered. One such quantity to be analyzed is the maximum distance the cell can penetrate in the given time interval, or P_{max}. A larger distance would indicate the cell can easily migrate through the matrix with little directional change, while a small distance indicates that the cell is either unable to move significantly, or has poor persistence and cannot escape from its relative position. The maximum cell penetration is plotted against adhesive strength for multiple membrane deformabilities and matrix geometries as seen in Figure 5.6. Similar trends are noted in each geometry. An increase in maximum penetration is seen with α, but a saturation appears to occur at higher deformabilities. This implies that once a cell becomes excessively deformable, it no longer

gains any advantage towards penetrating a matrix. This excessive deformability, in fact, may prevent the cell from migrating efficiently due to its highly active nature. Furthermore, a decreasing trend in the ability to penetrate the matrix is seen as adhesive strength is increased. This effect is more pronounced at larger deformabilities, and is caused by adhesion pulling a cell away from its trajectory, resulting in more turns and therefore less directed motion away from the initial location.
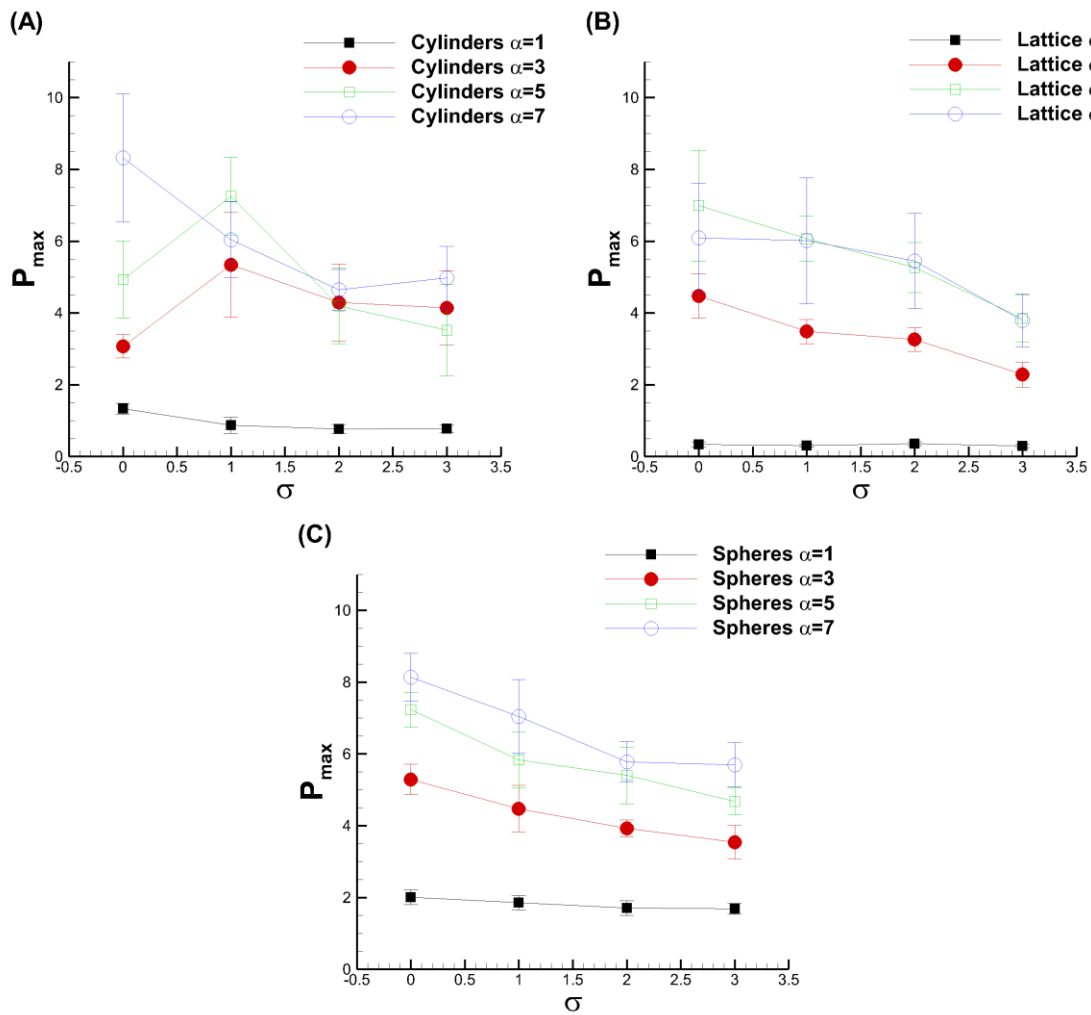
Figure 5.6: Maximum penetration P_{max} plotted against adhesive strength under varying membrane deformabilites. **(A)** Cylinders $\phi = 0.68$, $\gamma = 0.5$. **(B)** Lattice $\phi = 0.68$, $\gamma = 0.5$. **(C)** Spheres $\phi = 0.68$, $\gamma = 1$.
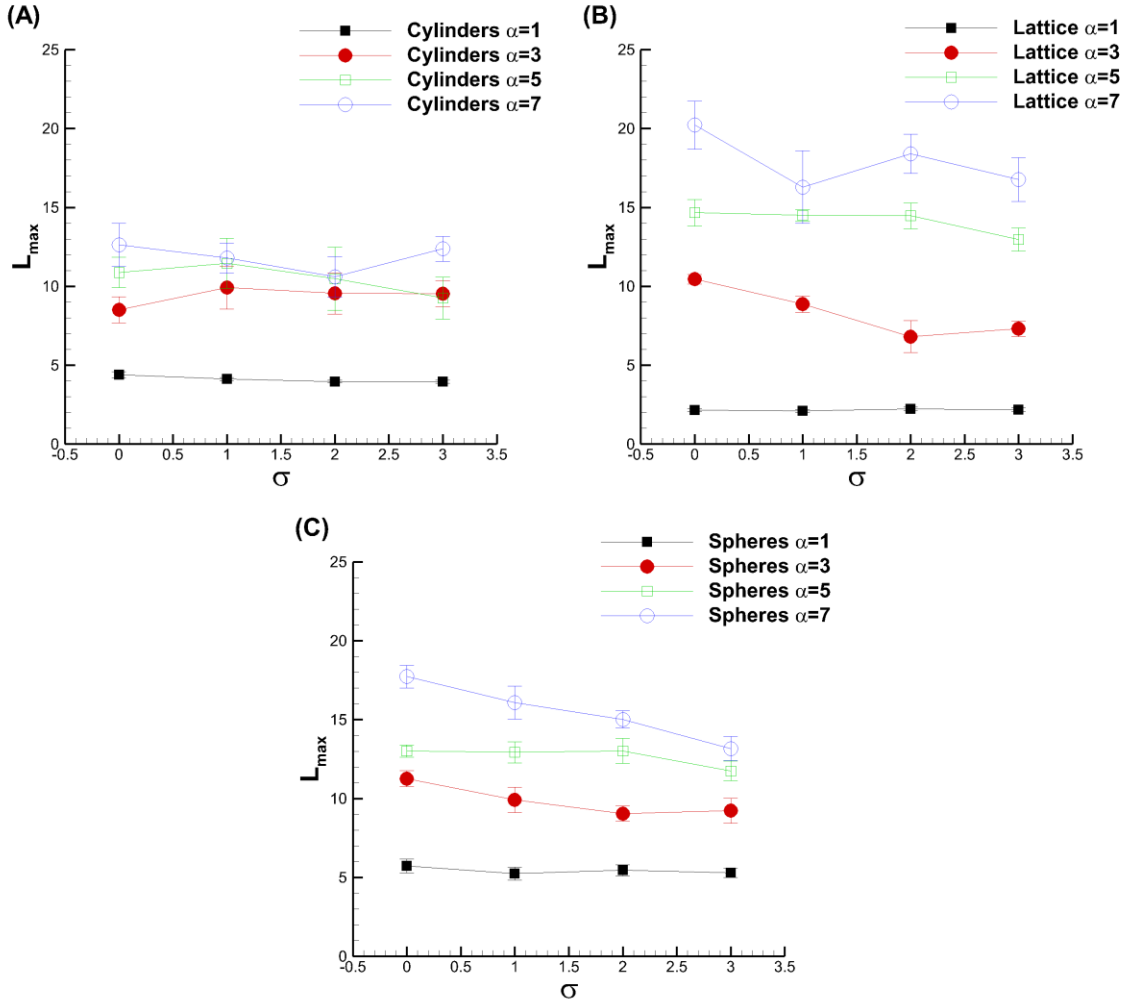
Figure 5.7: Accumulated distance traveled L_{max} by a cell. **(A)** Cylinders $\phi = 0.68, \gamma = 0.5$. **(B)** Lattice $\phi = 0.68, \gamma = 0.5$. **(C)** Spheres $\phi = 0.68, \gamma = 1$.

The accumulated distance traveled L_{max}, which tracks the entire distance traveled by the cell, is plotted in Figure 5.7 as a function of adhesive strength. Values are observed to remain fairly constant as the adhesive strength is increased, with a minor decreasing trend seen for higher deformability cases. A greater distance is traveled by the cell for larger membrane deformabilities, yet as predicted by Figure 5.6, the cell is not necessarily migrating through the matrix more efficiently. We also note that migration through aligned

cylinders (Figure 5.7A) has lower magnitudes than that for the lattice and sphere geometries. Because the minimum gap distance between cylinders is approximately 57% of the cell radius, while that for lattice and spheres are 135% and 35% of the cell radius, respectively, we attribute this to the adhesive dynamics which are discussed later. A saturation in total distance traveled is seen in the aligned cylinder geometry as well, meaning increased deformability has less of an effect in that geometry.
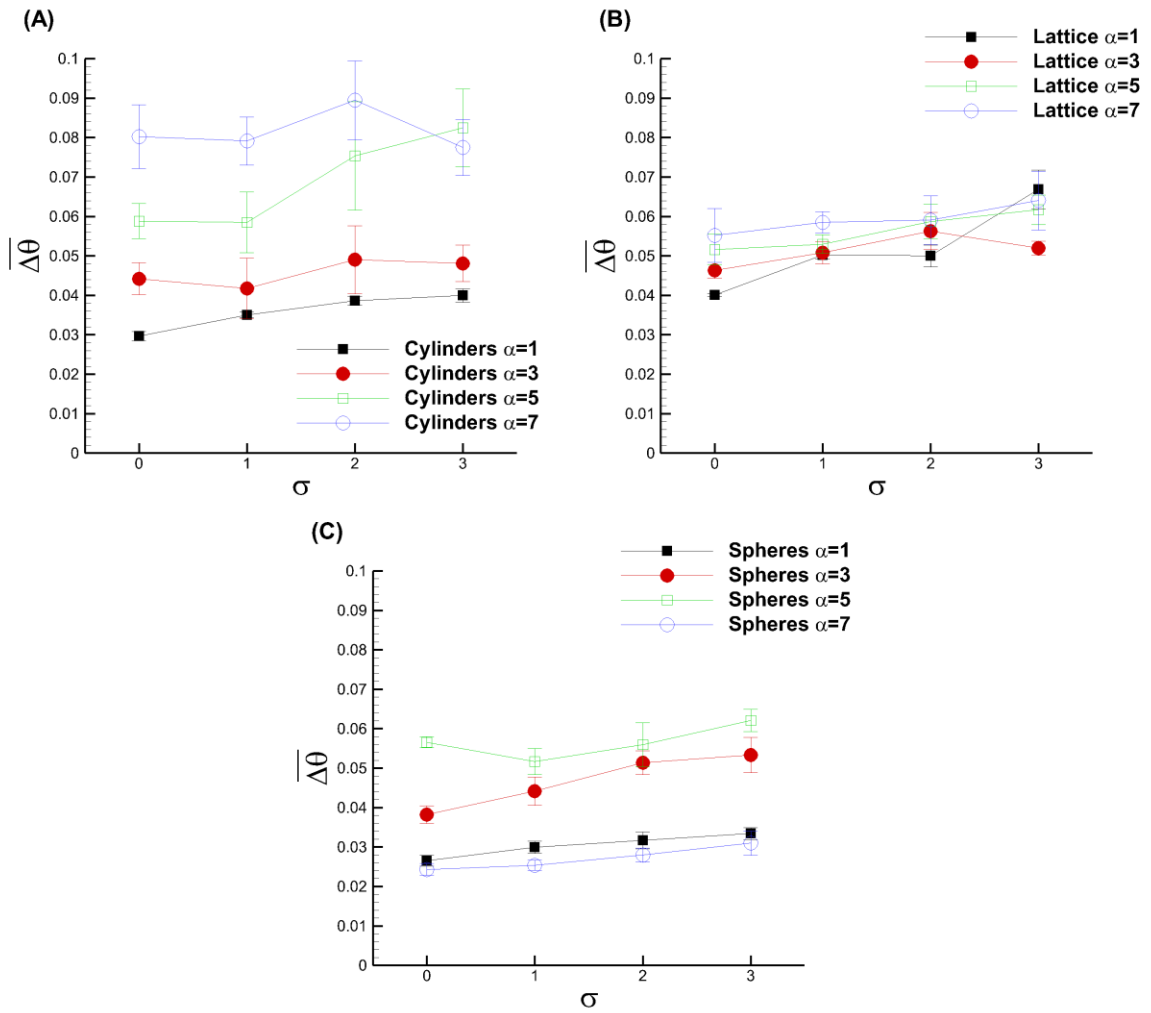
Figure 5.8: Persistence plots as a function of adhesive strength for various membrane deformabilities **(A)** Cylinders $\phi = 0.68$, $\gamma = 0.5$. **(B)** Lattice $\phi = 0.68$, $\gamma = 0.5$. **(C)** Spheres $\phi = 0.68$, $\gamma = 1$. Filled black squares $\alpha = 1$, Filled red circles $\alpha = 3$, Open green squares $\alpha = 5$, and Open blue circles $\alpha = 7$.

The influence of adhesion on cell persistence was also investigated. Persistence was calculated as the line integral of the change in angle along the trajectory, and then normalized by the total distance traveled (recall Equation 4.1). Plots of persistence are shown in Figure 5.8, where zero represents a perfectly persistent trajectory, and positive increasing numbers convey a reduction in directed cell migration. Each geometry reveals that persistence decreases as adhesive strength increases. This is a direct result of geometry and adhesion dynamics acting on the cell membrane. When a pseudopod comes into adhesion range with a matrix obstacle, our Monte-Carlo adhesion model decides whether bonds will form. If bonds form, they will pull the pseudopod away from its migration direction because of the convex geometry (spheres and cylinders) found in our matrices. Depending on adhesive strength and pseudopod dynamics, the cell's trajectory can effectively be altered, resulting in a weaker persistence. Amoeboid neutrophils have been observed to experience frequent directional changes, possibly due to obstructions in the tissue [163]. We note that the persistence is almost identical for different deformabilities in the lattice geometry (Figure 5.8B). This is likely due to having the largest gaps between obstacles available, and a direct line of site for the cell to migrate. Therefore, deformability is not much of a consideration for the lattice geometry when looking at persistence. For the cylinder and sphere geometry, however, the persistence is not identical. In the cylinder matrix (Figure 5.8A), persistence decreases with increasing deformability, since pseudopods are more frequent and active, creating the possibility of a cell detouring off course because of pseudopod dynamics. In the sphere geometry (Figure 5.8C), larger deformability is seen to have an increased persistence than smaller magnitude deformabilities. This is likely caused by the narrow gaps between obstacles, since cells

without sufficient deformability cannot penetrate the matrix and therefore change direction more often.

So far, increasing adhesion has been shown to decrease the extent of a cell's ability to penetrate the matrix geometry, slightly decrease the total distance traveled by the cell, and decrease the cell persistence. With this in mind, a question arises to the extent to which adhesion helps or hinders cell migration. Taking the dot product of the normalized adhesive traction vector and cell trajectory produces a scalar value between -1 and 1. Positive values show that the adhesive force is helping the cell migrate, while negative values are shown to hinder migration. Time-averaged quantities are labeled simply as "advantage," and are plotted in Figure 5.9 against the adhesive bond strength. First, it is noted that a cell with low deformability ($\alpha = 1$) has an advantage of nearly zero, indicating adhesion does not help or hurt its migration. In most cases, a deformability this low will not allow the cell to penetrate the matrix at all, and therefore adhesion has no effect. When deformability is higher, however, adhesion has a more pronounced effect. For each geometry, the advantage from adhesion is negative, indicating adhesive bonds are interfering with the amoeboid cell's migration. As adhesive strength is increased, however, there appears to be a positive, upward trend in the advantage. This trend is most noticeable for the lattice geometry in Figure 5.9B. It can also be observed, though a somewhat smaller in effect, in the cylinder and spheres geometries. The effect is most prominent for the case of intermediate deformability ($\alpha = 3$). Although the advantage still remains negative, the data appears to show that a cell with intermediate deformability can utilize adhesion better than cells with large deformabilities. Furthermore, because each instance with a deformability above $\alpha =$

1 in Figure 5.9 is negative, the data also implies amoeboid motility is better off without utilizing adhesion.
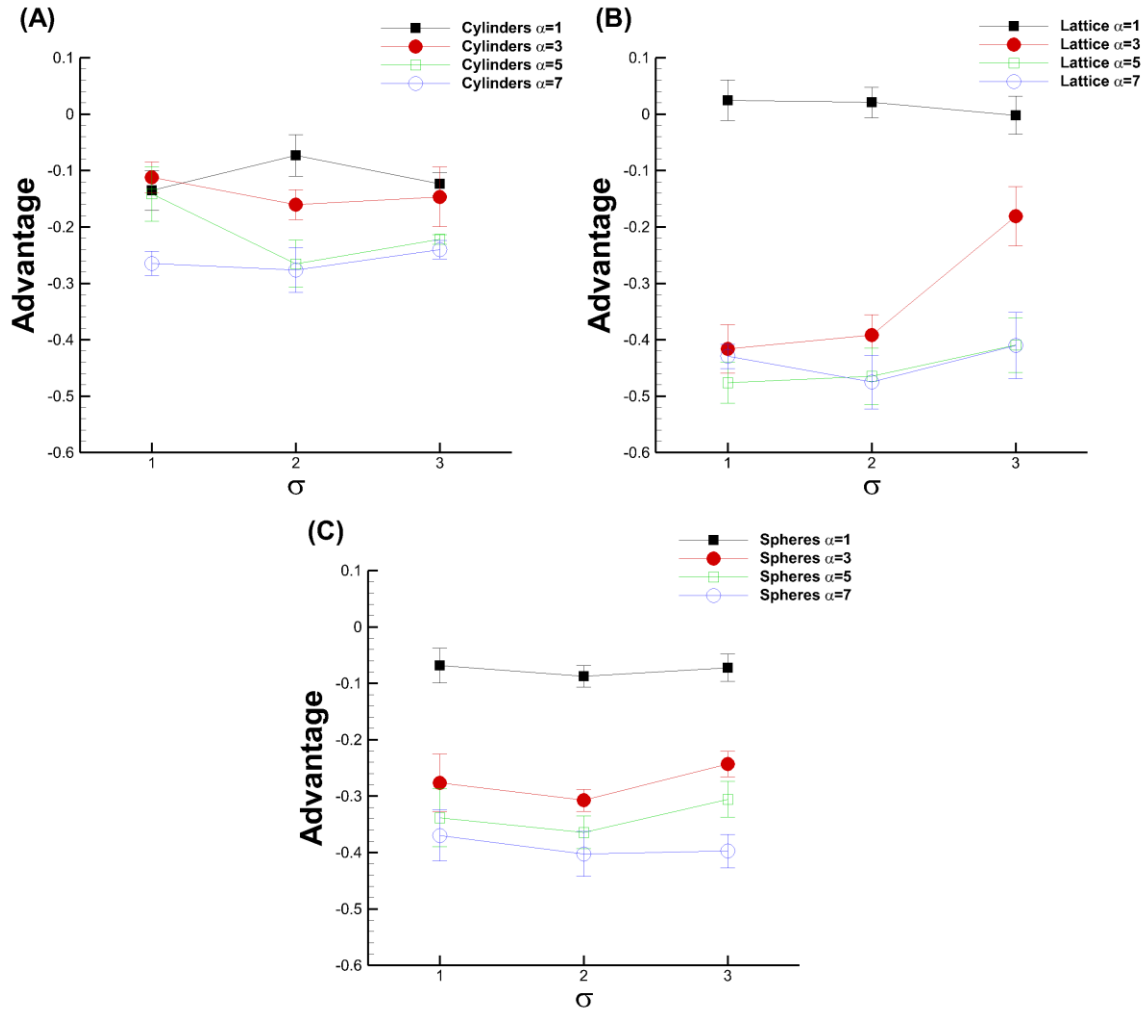
Figure 5.9: Average adhesion helpfulness as a function of adhesive strength for various membrane deformabilities. **(A)** Cylinders $\phi = 0.68$, $\gamma = 0.5$. **(B)** Lattice $\phi = 0.68$, $\gamma = 0.5$. **(C)** Spheres $\phi = 0.68$, $\gamma = 1$. Filled black squares $\alpha = 1$, Filled red circles $\alpha = 3$, Open green squares $\alpha = 5$, and Open blue circles $\alpha = 7$.

While the results of Figure 5.9 paint adhesion as either an absolute helper or absolute hinderer, as the cell migrates through the extracellular matrix geometry over time, adhesion can change the advantage seen by the cell. Figure 5.10 presents the time-dependent

advantage for each geometry. We note that the cylinder plot (Figure 5.10A) is for the more

porous $\phi = 0.83$ geometry. The advantage is ocassionally seen near a value of 1 and -1,

indicating the benefit from adhesion depends on how the cell is positioned near an obstace.

If the cell is moving away from an obstacle, the advantage is likely to be negative as bonds

still linked to the cell provide resistance. Conversely, if the cell front is moving past an

obstacle, bonds which are likely to form will help pull the cell in the direction of migration.
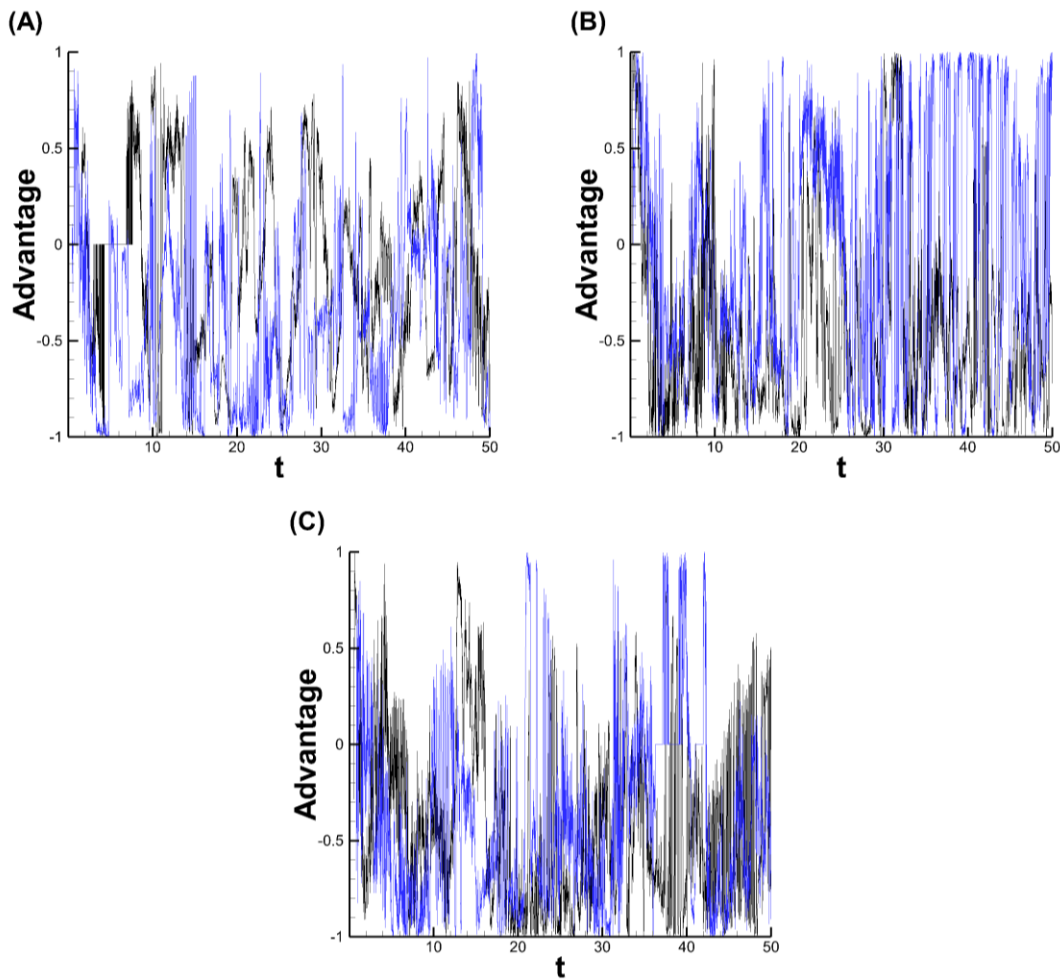
Figure 5.10: The dot product between the cell's trajectory and the net adhesive force vector is plotted over time. Positive magnitudes indicate adhesion helps pull the cell forward, while negative magnitudes imply adhesion pulls against the direction of migration. **(A)** Cylinders $\phi = 0.83$, $\gamma = 0.5$. Black line: $\alpha = 1$ and $\sigma = 1$. Blue line: $\alpha = 7$ and $\sigma = 3$. **(B)** Lattice $\phi = 0.68$, $\gamma = 0.5$. Black line: $\alpha = 3$ and $\sigma = 1$. Blue line: $\alpha = 3$ and $\sigma = 3$. **(C)** Spheres $\phi = 0.68$, $\gamma = 1$. Black line: $\alpha = 5$ and $\sigma = 1$. Blue line: $\alpha = 5$ and $\sigma = 2$.
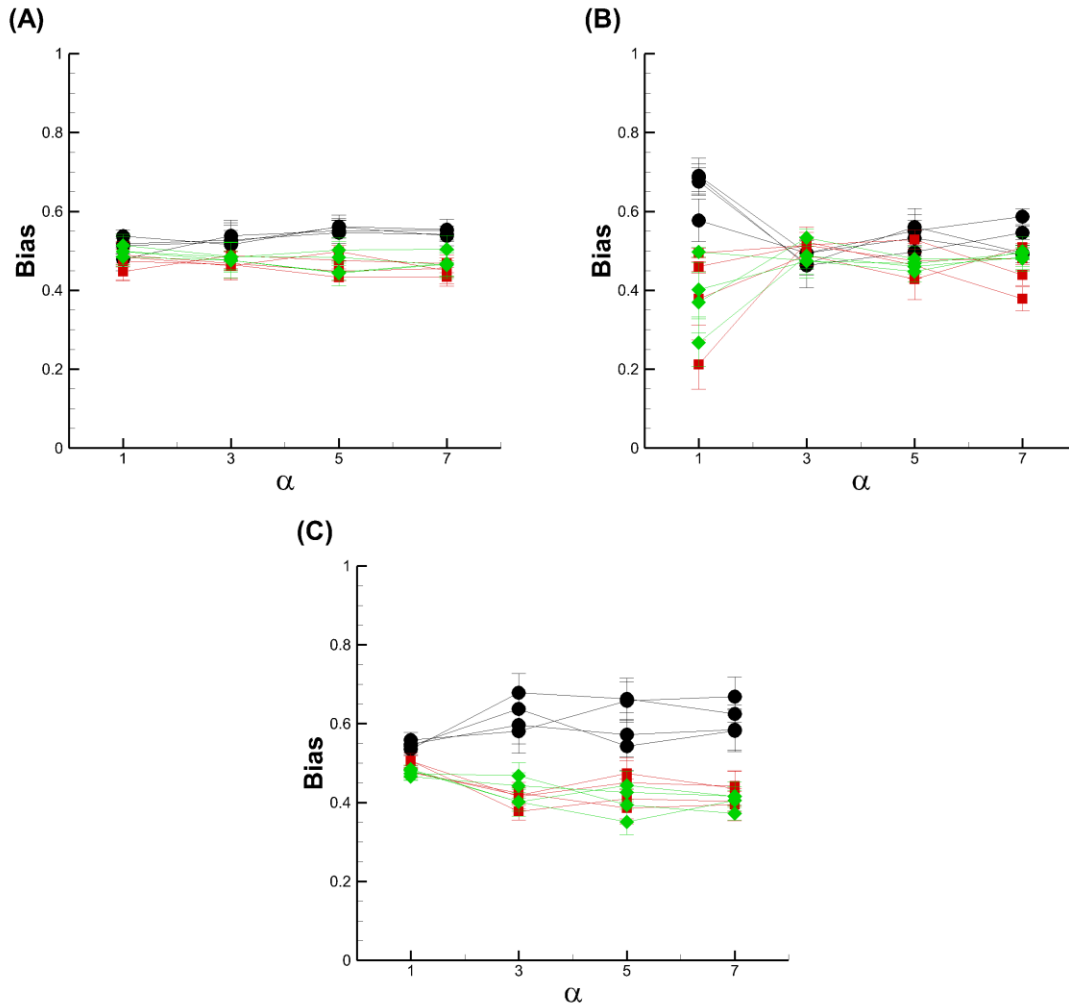
Figure 5.11: Cylinder bias for aligned cylinders as a function of membrane deformability **(A)** $\phi = 0.83$. **(B)** $\phi = 0.78$ **(C)** $\phi = 0.68$. Larger magnitudes reveal a preference in cell migration direction. Black lines and circles: x-bias, Red lines squares: y-bias, Green lines and diamonds: z-bias. $\gamma = 0.5$ for each instance.

In the aligned cylinder geometry, cylinders are oriented in the x-direction. This means a cell migrating through this type of matrix may have an easier experience moving through the matrix if it were to choose the x-direction over the y- or z- directions. An analysis was performed to see if cells utilize this advantage more so on average than migrating in the alternate directions. A cylinder bias plot is shown in Figure 5.11, where the projection of the unit trajectory vector is taken onto the three principal cartesian directions and averaged

over time. Larger magnitudes indicate the cell has a stronger preference for migration in that direction, while the reverse is true for smaller magnitude values. For the first cylinder geometry with porosity $\phi = 0.83$ shown in Figure 5.11A, the bias is essentially neutral, with magnitudes near 0.5, indicating the lack of a preference or aversion for any direction. This is true across every adhesive strength in addition to simulations with no adhesion. For a denser array of aligned cylinders ($\phi = 0.78$) (Figure 5.11B), however, we note a bias occurs when $\alpha = 1$. This occurs because the cell's low deformability prevents it from migrating through the matrix in a transverse manner (y or z direction). Instead, the cell migrates along the longitudinal direction. A small spike in bias is also seen in higher deformabilities, suggesting a stronger impact on cell orientation. Finally, for a matrix porosity of $\phi = 0.68$ (Figure 5.11C), the bias is not seen for a deformability of $\alpha = 1$, but is seen for larger deformabilities. We note that once a cell enters the highly confined matrix (see Figure 5.2A), it is difficult to reorient due to its polarized nature.

5.2.3 Pseudopod Dynamics

Pseudopod dynamics were quantified while varying membrane deformability and adhesive strength. Average pseudopod lifetime, the average number of pseudopods present, and the proportion of *de novo* pseudopods to total pseudopods were analyzed. Figure 5.12 below shows the average pseudopod lifetime as a function of adhesive strength for each matrix geometry. We note that the aligned cylinders geometry uses a porosity $\phi = 0.83$. A decreasing trend in lifetime is seen as α is increased, due to an increasing number of pseudopod collisions. Similar effects were seen without adhesion present in Chapter 4 [103]. Furthermore, adhesive strength does not appear to have much effect on average lifetimes, since lifetimes for equivalent cell parameters are similar among each geometry.

One explanation is that adhesion merely directs the pseudopod, so that its dynamics remain similar for the most part. We also observe that pseudopod lifetime is more similar at higher deformabilities since pseudopod dynamics are random for stiffer cells, but tend to focus for softer cells [103,148]. One final note concerns the pseudopod lifetimes for $\alpha = 1$, which can be two to three times as high as lifetimes for the other deformabilities. At this deformability, the membrane lacks the softness required to penetrate the matrix, and is therefore less likely to force a reset of the activator-inhibitor system, resulting in longer life.
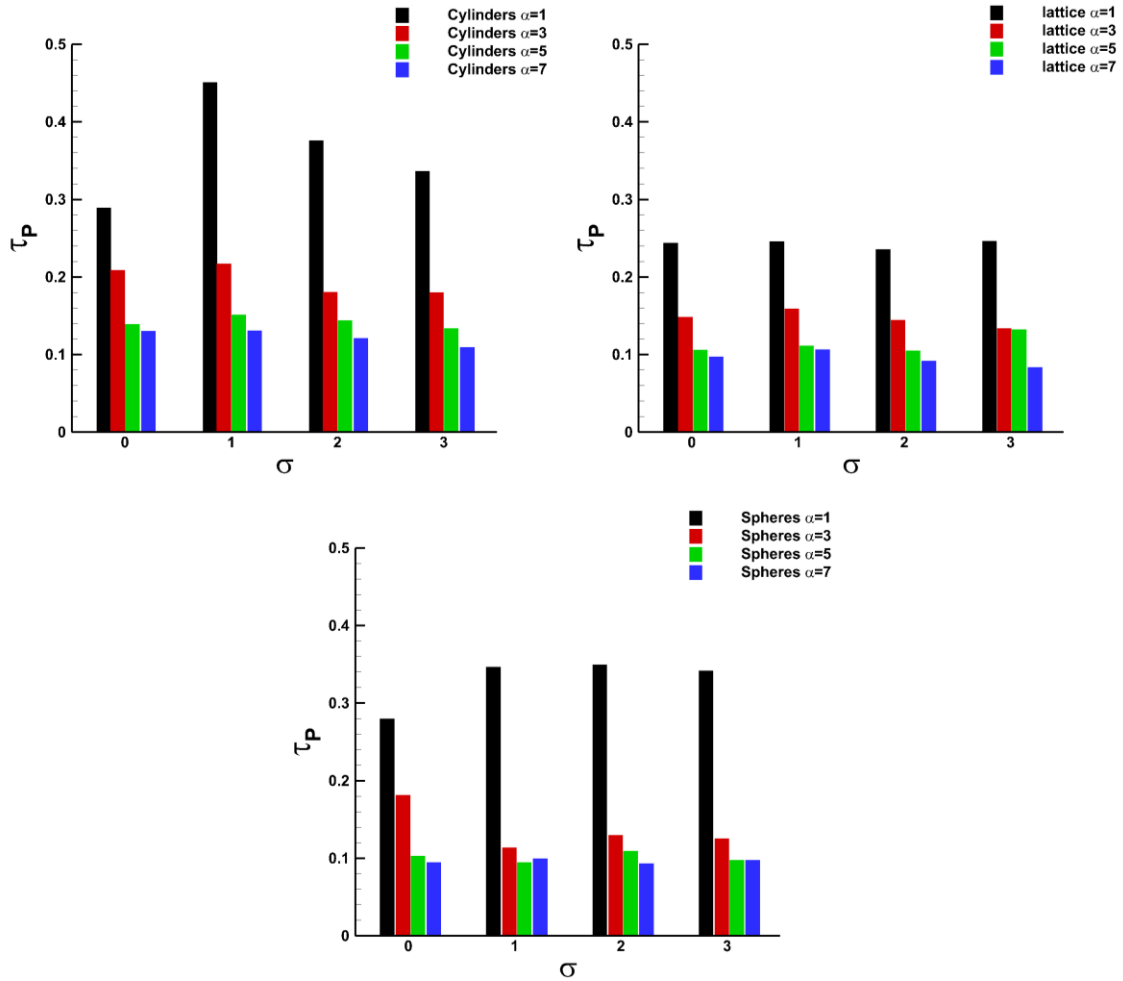
Figure 5.12: Average pseudopod lifetimes as a function of adhesive strength. **(A)** Cylinders $\phi = 0.83, \gamma = 0.5$. **(B)** Lattice $\phi = 0.68, \gamma = 0.5$. **(C)** Spheres $\phi = 0.68, \gamma = 1$.

The average number of pseudopods present over time is also plotted below in Figure 5.13 against the adhesive bond strength. Only small differences in the can be seen across all parameter ranges. Slight increases can be observed to occur for aligned cylinders and three-dimensional lattice geometries as membrane deformability is increased, as was seen in Chapter 4 [103]. Conversely, a slight decrease in the average number of pseudopods is seen for the spherical array geometry. We consider this observation a uniqueness of the geometry, as the deformable cell has more room to extend pseudopods in as compared to a stiff cell.
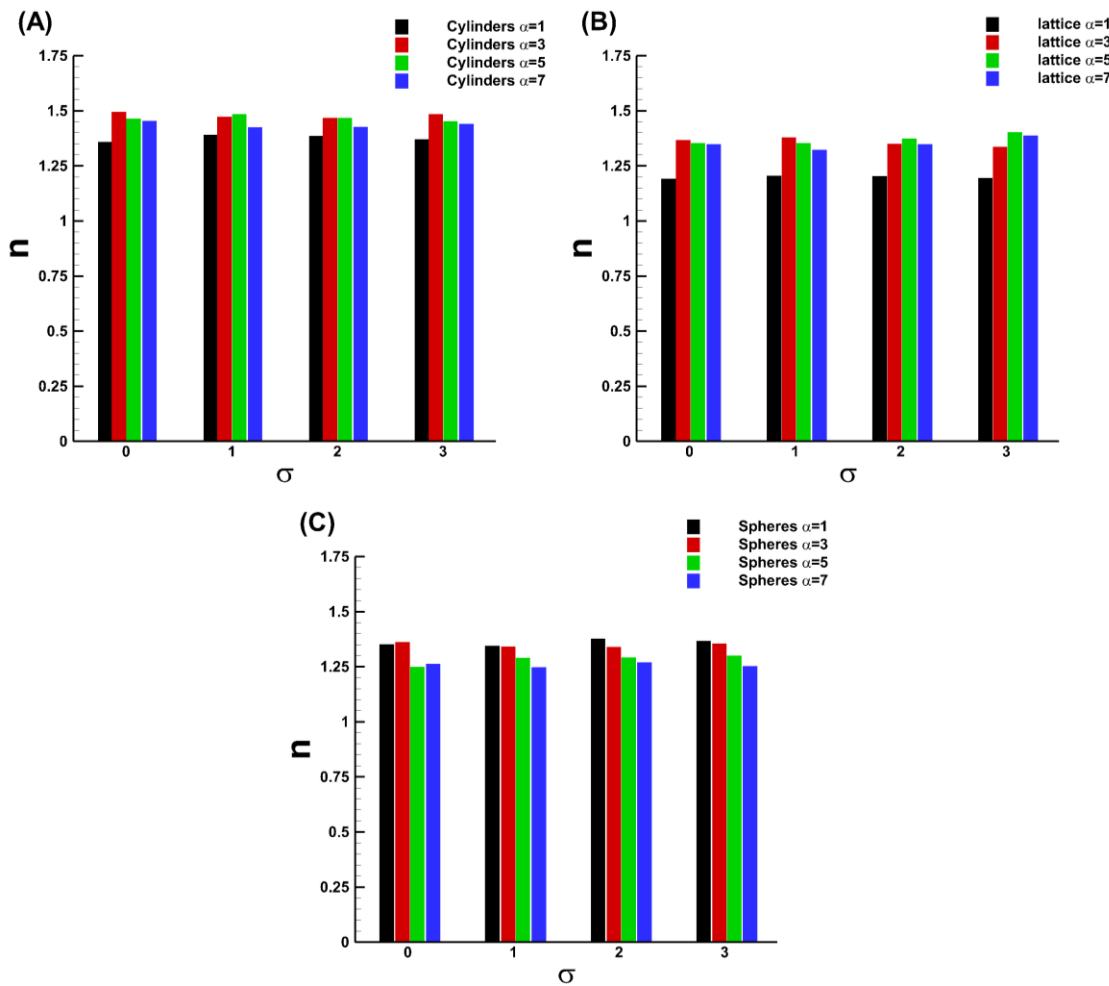
Figure 5.13: Average number of pseudopods existing vs adhesive strength. **(A)** Cylinders $\phi = 0.83, \gamma = 0.5$. **(B)** Lattice $\phi = 0.68, \gamma = 0.5$. **(C)** Spheres $\phi = 0.68, \gamma = 1$.

Finally, *de novo* pseudopod ratios are plotted below against the adhesive bond strength for each membrane deformability in Figure 5.14. *de novo* ratios appear to increase with increasing membrane deformability as was seen in Chapter 4 [103], due to more frequent resets of the activator-inhibitor system. Additionally, the *de novo* pseudopod proportions look as if they are unaffected by adhesive strength. We reason that confinement has a much larger influence on pseudopod dynamics than adhesion.
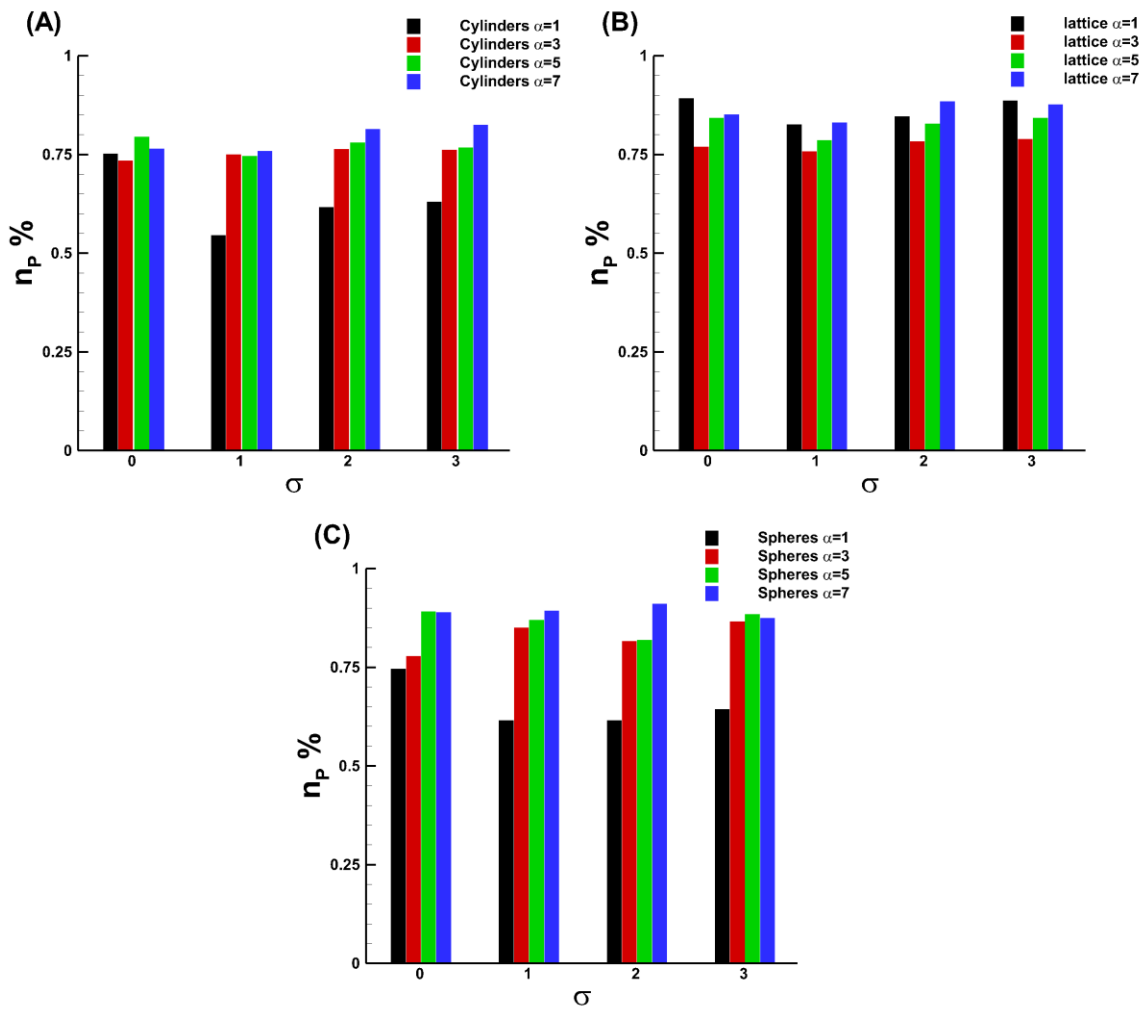
Figure 5.14: Percentage of *de novo* pseudopods existing against adhesive strength. **(A)** Cylinders $\phi = 0.83$, $\gamma = 0.5$. **(B)** Lattice $\phi = 0.68$, $\gamma = 0.5$. **(C)** Spheres $\phi = 0.68$, $\gamma = 1$.

5.2.4   Migration Speed

The average speed of an amoeboid cell migrating through aligned cylinders, three-dimensional lattice, and arrays of spheres is plotted below in Figure 5.15. Average cell speed is observed to increase with membrane deformability. An increase in cell speed with increasing deformability was also noted in our earlier papers [103,148], as the coupled reaction-diffusion system produced focused instabilities leading to a higher cell speed. In confined medium, larger deformability also leads to cells capable of migrating through narrow gaps in the matrix, resulting in a larger displacement and speed. Average speed is seen to remain almost constant as the adhesive strength is increased, though. A slight downward trend is seen for larger values of cell deformability. This indicates that adhesion has little effect on cell speed except at large values of α. Similar trends were seen in the maximum penetration and total distance traveled by the cell in Figures 5.6 and 5.7, respectively. The average migration speed for the cylinder geometry (Figure 5.15A) is seen to be comparable for low and intermediate levels of deformability ($\alpha = 1$ and 3), but reduced for high levels of deformability ($\alpha = 5$ and 7). This is due to the large confinement experienced by the cell, making matrix penetration exceedingly slow.

Dimensionless average cell speed was approximately in the range of $0.05 - 0.4$, which scales to $0.3 - 2.4$ $\mu m/min$. Reported speeds of amoeboid cells migrating in three-dimensional matrices vary in the literature based on cell type and ECM properties, though we have found speeds of 0.07-0.6 $\mu m/min$ [1], 2-25 $\mu m/min$ [151], 4 $\mu m/min$ [59] , 5-8 $\mu m/min$ [37], 0.1-20 $\mu m/min$ [28], and 1-5.5 $\mu m/min$ [50], which mostly agrees well with our result. We note that each experiment investigated cell migration likely using

different cells and tissues which explains the large ranges. For a suitably confined matrix, our results are indeed agreeable.
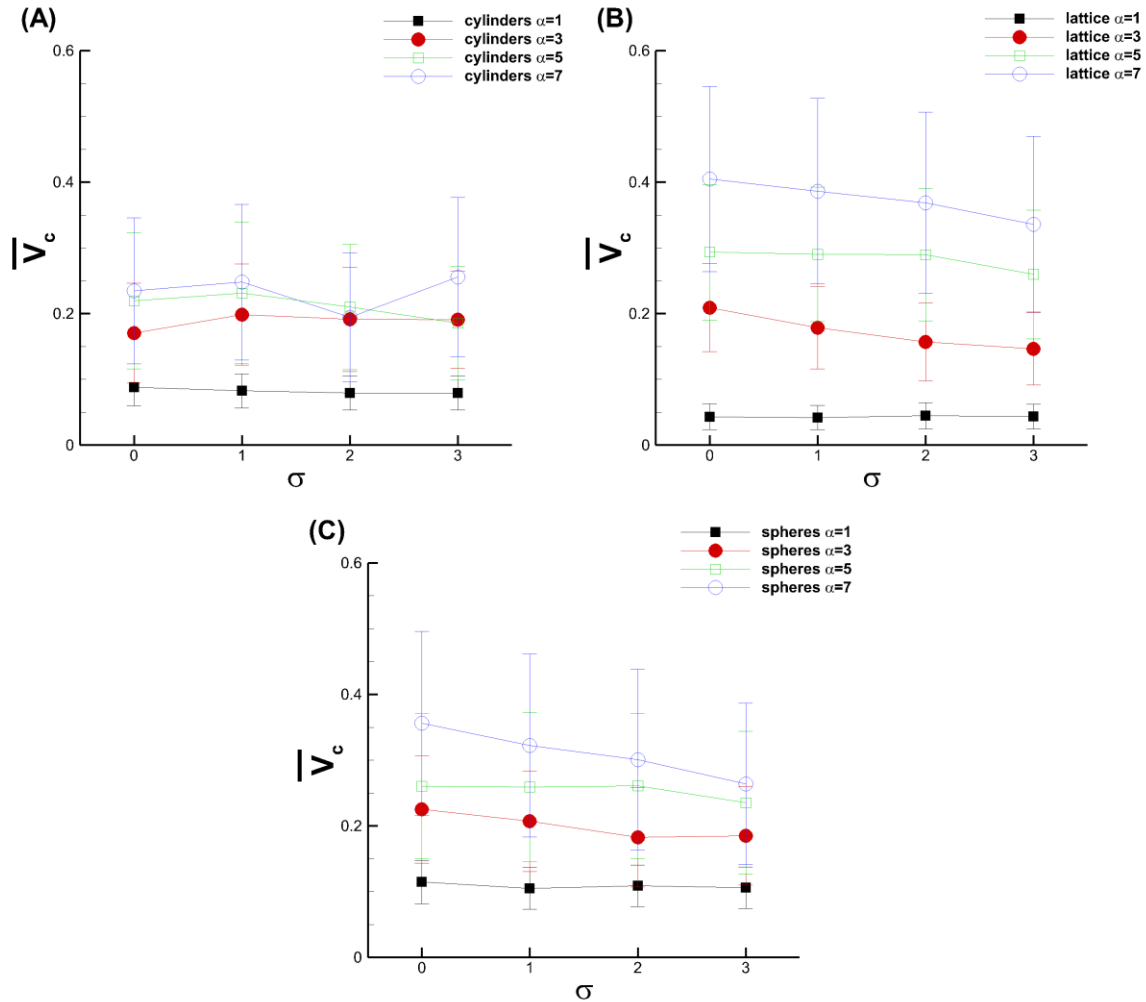

Figure 5.15: Average cell speed as a function of adhesive bond strength. **(A)** Cylinders $\phi = 0.68$, $\gamma = 0.5$. **(B)** Lattice $\phi = 0.68$, $\gamma = 0.5$. **(C)** Spheres $\phi = 0.68$, $\gamma = 1$.

5.2.5   Bond Dynamics

Finally, bond dynamics are considered. Both the position of bonds along the cell and the number of bonds existing between a cell and matrix are quantified. Bond position can indicate where the majority of bonds form over time as the cell migrates through the matrix,

revealing certain trends or irregularities. As such, bond positions have been plotted below in Figure 5.16, where the abscissa characterizes the location on the cell. Zero represents the location of the cell centriod, while 1 and -1 are the cell front and rear, respectively. Each geometry shares the same distinct trend, showing a peak slightly forward of the cell centroid, representing the location of maximum bond density. Bond density quickly diminishes moving from the centroid to the cell front. Density also decreases moving towards the rear of the cell from the centroid, with a secondary maxima located slightly behind the centroid. This universal trend is seen across all adhesion strengths and membrane deformabilities, with exception to low defomabilities in the aligned cylinder geometry and three-dimensional lattice geometry. In those two cases, another trend in bond density emerges. Maximums in bond density appear near the cell-rear and cell-front regardless of the adhesive bonds strength, suggesting that the cell shape itself is the reason for this secondary trend. The rear bonds indicate a defect in cell migration capacity since they pull the cell against its direction of movement, indicating a lack of bond rupture. This connects to several studies, which have noted that integrins can impede invasion, as seen in types of melanoma, breast, and colon cancers [28]. There are also cases of mutant cells with a reduced ability to form [164] or break adhesions [165], thereby affecting cell behavior and migration. The front-distributed bonds indicate a more active leading-edge. Because the bond density distribution is nearly level for this trend, we conclude that bond distribution is almost uniform on the entire cell, consistent with a cell unable to penetrate the matrix.
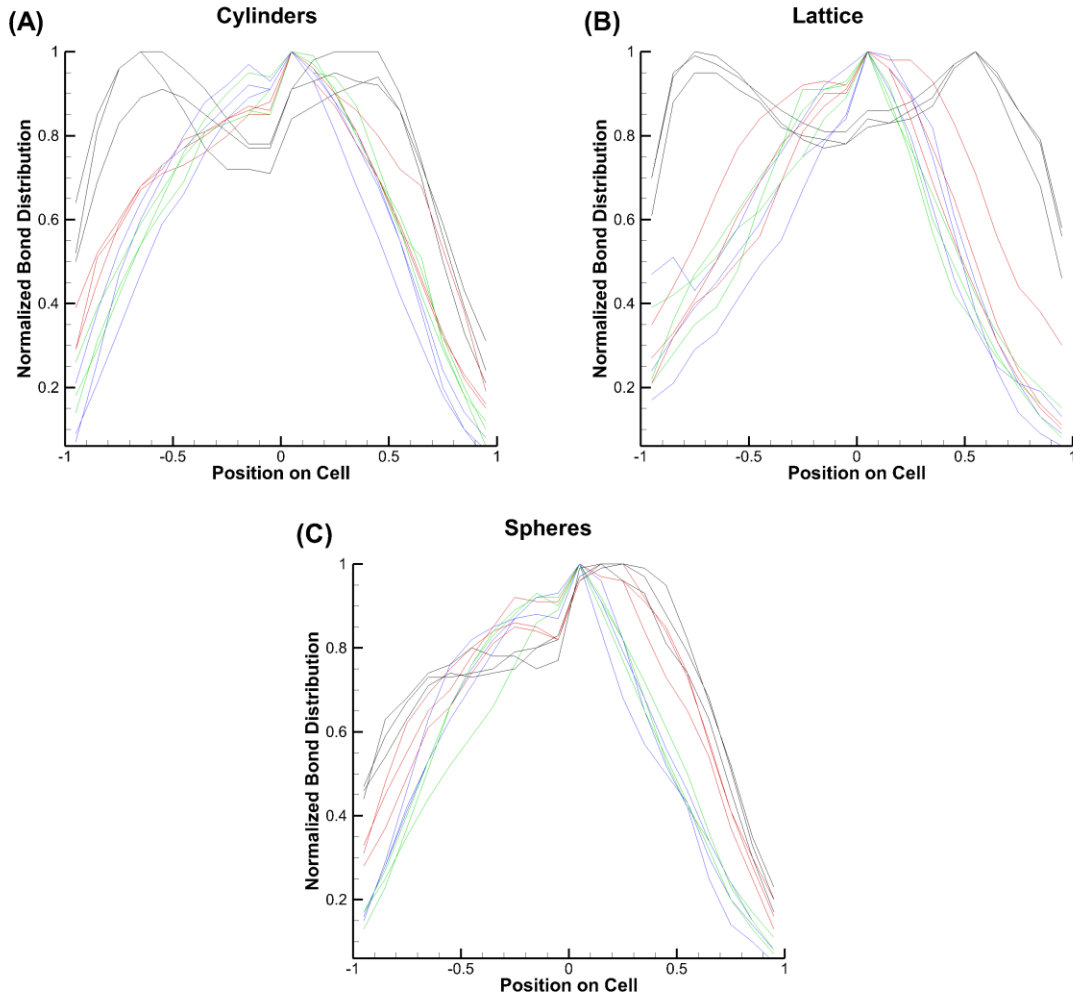
Figure 5.16: Average bond position relative to cell. On the abscissa, 0 represents the location of the cell centroid while 1 and -1 represent the front and rear of the cell, respectively. Each plot is normalized to a maximum value of one. **(A)** Cylinders $\phi = 0.68$, $\gamma = 0.5$. **(B)** Lattice $\phi = 0.68$, $\gamma = 0.5$. **(C)** Spheres $\phi = 0.68$, $\gamma = 1$. Black lines: $\alpha = 1$. Red lines: $\alpha = 3$. Green lines: $\alpha = 5$. Blue lines: $\alpha = 7$.

The average number of bonds active on a cell in each geometry was also calculated in Figure 5.17. It was observed that matrix geometry played a large role on the number of bonds formed on the cell, as well as the trend in bond quantity as deformability and adhesive strength were varied. Bond count is observed to increase with increasing deformability for aligned cylinders and spheres, but decrease in the lattice geometry. In the

former case, the bound count approximately doubles between $\alpha = 1$ and 7, while in the latter case, the bound count is approximately halved between the same deformabilities. As all cell parameters are identical, the geometry must be the reason for the effect on number of bonds. The proportion of surface area available for bonding is likely a key factor, since the cell imparts differently on aligned cylinders, lattice (cylinders in each cartesian direction), and spheres in a unique way. Therefore, geometry is a principal factor influencing the number of bonds which will form, and as a result, the type of cell behavior which will arise.
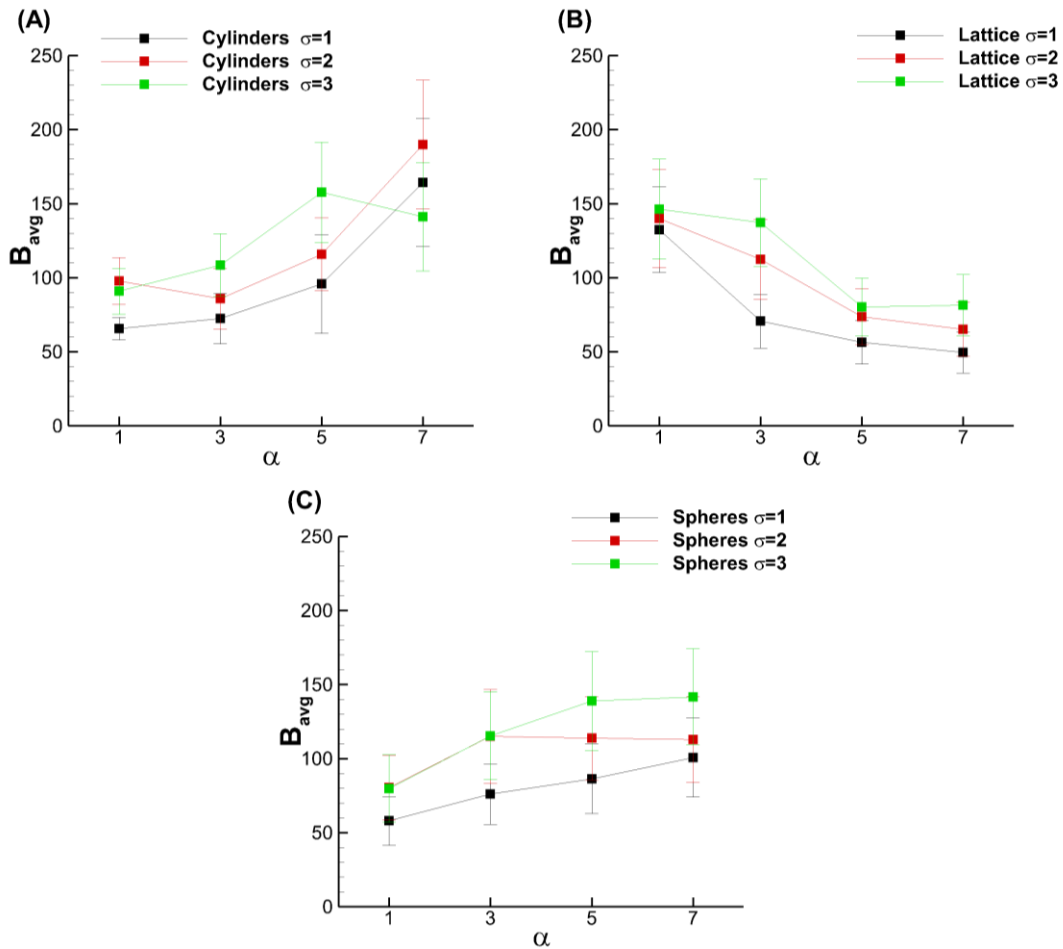
Figure 5.17: Average number of bonds B_{avg} as a function of membrane deformability for various adhesive bond strengths **(A)** Cylinders $\phi = 0.68$, $\gamma = 0.5$. **(B)** Lattice $\phi = 0.68$, $\gamma = 0.5$. **(C)** Spheres $\phi = 0.68$, $\gamma = 1$.

In general, the number of bonds is seen to increase with adhesive strength. We attribute this to a positive-feedback system. When a bond is established between the cell membrane and matrix surface, a tensile force is applied to simulate adhesion. The bond location on the cell membrane combined along with adjacent bond sites are then forced to remain close to the matrix surface, thereby increasing the probability that new bonds will form.

5.3 Summary

In summary, a three-dimensional computational model was developed for an amoeboid cell immersed in various extracellular matrix geometries, where cell behavior and pseudopod dynamics were analyzed. A weak variant of adhesion commonly associated with amoeboid migration was modeled, while the effect of adhesive strength on cell migration was calculated. Large scale deformations were predicted as each cell migrated through the confining geometry, consistent with experimental results. In addition to dynamics previously seen including freezing, probing, doubling-back, and tug-of-war, two new dynamics involving adhesion were observed. A gliding-type motion was discovered, where the cell formed transient adhesions as it sidled between two obstacles. Rear cell retraction relative to the main cell body was also witnessed during migration through narrow gaps in the matrix. Maximum penetration and total distance traveled by the cell were calculated, showing slight decreases in magnitude as the adhesive strength increased. Adhesion was shown to decrease persistence, as adhesive bonding often detoured cells away from their previous trajectory. The advantage of adhesion on amoeboid cell migration was found, where in general, amoeboid migration was inhibited. Higher deformabilities were shown to perform worse than cells with an intermediate deformability. Over time, however, cells did experience some benefit from adhesion. Bias in the migration direction

in the aligned cylinder geometries was calculated, showing cells in higher confinement have a slight preference towards traveling in the longitudinal direction of matrix fibers. Pseudopod dynamics were quantified, showing little effect from adhesion. Average cell migration speed was found, showing slight decreases in speed as adhesive strength was increased. Finally, bond dynamics were described, showing the distribution of bond density on the cell for each geometry and parameter range. A universal bond distribution was seen, while a secondary trend was noted for two geometries. The average number of bonds was also calculated, showing the coupling between cell geometry and the cell. To summarize, adhesion was seen to have some influence in determining the behavior of a migrating amoeboid cell, though confinement and deformability are the principal instigators of cell behavior and pseudopod dynamics.

Chapter 6

Conclusions of Dissertation and Directions for Future Work

6.1 Conclusions

In conclusion, we have developed a three-dimensional, multiscale, multiphysics model of amoeboid cell motility which couples fluid-mechanics, solid-mechanics, and a dynamic pattern formation model to simulate pseudopod-driven locomotion through a porous extracellular medium. The extracellular space is composed of a viscous fluid surrounding various forms of rigid, non-moving geometries: aligned cylinders, three-dimensional lattice, and spherical arrays. An unbounded fluid medium is also considered. An immersed-boundary method is used to couple the cell to the fluid, and fluid to the matrix, allowing for a seamless integration of both deformable and nondeformable interfaces. Reaction-diffusion of activator-inhibitors, extreme cell deformation, pseudopod dynamics, cytoplasmic and extracellular fluid motion, and a fully resolved extracellular environment are all modeled. Cell deformation is solved for through the use of a finite-element method, while fluid interaction is modeled using Stoke's equation and solved by finite volume and spectral methods. Activator-inhibitor dynamics, which are modeled by coupled nonlinear equations, are solved using an evolving surface finite-element method. Solution yields dynamic patterns termed Turing instabilities, which are taken to be cell membrane proteins linked to the protrusive capacity of the cell. Adhesion is considered using a modified Bell

model to determine the discrete dynamics of bond formation on the cell. No external cue or chemical bias is implemented.

The model expertly creates activator patches which generate pseudopod extensions of the cell membrane, dynamically extending, meandering, bifurcating, and retracting over the cell surface. Predicted cell shapes are similar to images captured in experimental works. In Chapter 3, a strong coupling is found between cell membrane deformability, surface protein diffusivity, and fluid viscosity. As such, cell dynamics are seen to transform, in certain parameter ranges, from a slow, non-persistent cell to a fast, persistent cell by adjustment of pseudopod dynamics. Amoeboid swimming is made possible by pseudopods acting as paddles, which act as a non-reciprocal motion necessary for net displacement on the microscale. Average swimming speeds are quantified, where the effect of deformability, diffusivity, and fluid viscosity is found. Speeds are seen to have nonlinear trends as each parameter is adjusted. Pseudopod dynamics are calculated, showing the changes in average lifetime in addition to the average and maximum number of pseudopods generated by the cell. Fluid field vectors are analyzed, revealing the presence of two generalized modes of swimming: pushers and pullers. Both modes are observed to occur, though unclassified patterns are more common due to the deformable nature of the cell and pseudopod dynamics.

In Chapter 4, the amoeboid cell is subjected to confined extracellular matrix geometries characterized by arrays of rigid, non-moving spheres of various matrix porosity and obstacle size. An investigation of the influence of curvature, deformability, and obstacles on Turing patterns is performed. Curvature and deformation are shown to destabilize activator patterns, making the cell more active as a result. Extreme deformation is observed

due to rigid obstacles impressing upon the deformable cell. Major changes in cell behavior and pseudopod dynamics are seen. The persistent, unidirectional cell migration seen in unbounded flow is lost, as obstacles prevent direct motion. The introduction of *de novo* pseudopods, however, helps the cell navigate through the complex medium. Interesting dynamics which are not seen in unbounded flow are observed, including doubling-back, tug-of-war, freezing, and probing. These dynamics elucidate a new coupling between the cell and matrix. Average migration speeds are calculated over each parameter range, revealing an asymptotic decrease in speed as confinement increases. Pseudopod dynamics are investigated, showing large-scale changes as compared to unbounded flow. Lifetimes are seen to decrease with increasing confinement, while the *de novo* pseudopod becomes a major player in directing cell migration. The physical limits on cell motility are determined for all parameter ranges, showing cell migration is hindered as deformability, porosity, and obstacle size decrease. Persistence is calculated, revealing a more random, undirected motion within the matrix for the same cell properties which produced persistent motion in unbounded flow. Finally, complex flow fields are seen as the cell and pseudopods interact with obstacles.

Lastly, in Chapter 5, amoeboid cell migration is introduced to several new geometries in addition to the presence of adhesion between the cell and matrix. Cell shapes are found to be highly deformed as confinement takes its effect on the highly deformable cell. In addition to freezing, probing, doubling-back, and tug-of-war, several new dynamics are seen, including a gliding-type motion and rear cell retraction, where both adhesion and confinement cause a contraction relative to the main cell body. The distance traveled and penetrated by the cell is found, revealing a slight dependence on adhesion. Cell persistence

is then calculated, showing adhesion decreases a cell's ability to direct its motion. This is due to adhesive bonds re-directing pseudopods, and cell trajectories as a result. The adhesive advantage is then generated, showing that while adhesion occasionally aids cell migration, on average it acts to inhibit motion, demonstrating that the amoeboid mode is better off without adhesion. Biases in migration direction for various porosities of aligned cylinders showed that increasing confinement also increases the propensity to travel along an aligned path. Pseudopod dynamics were shown to be similar to those in Chapter 4, while adhesion was seen to have little influence. Cell migration speeds were also seen to have a slight decreasing effect due to adhesion. Finally, bond density over the cell was calculated, showing the existence of one universal trend in where bonds form. The average number of bonds was then found, showing the importance that extracellular matrix geometry has on cell behavior.

To our knowledge, no other three-dimensional pseudopod-driven computational model has revealed as much information about amoeboid motility as our model has. Our cell is capable of extreme deformation, while able to generate dynamic and copious amounts of pseudopods which allow the cell to achieve dynamics observed within the literature. Furthermore, cell-fluid-matrix coupling shows our model to be well-resolved and free of *ad hoc* corrections needed to patch inconsistencies. With future work aimed at improving the cell model, while greatly enhancing the extracellular matrix, we foresee many more insights as studies of the largely important pseudopod-driven amoeboid migration are continued.

6.2 Directions for Future Work

In the case of the ever-growing field of amoeboid cell migration, and cell migration in general, a rich amount of opportunities exists for future academic contributions. The following sections are intended to serve as a guide for future endeavors, and therefore are constructed with as much detail as possible. Some topics can be easily adapted into the current computational model while others would require larger scale additions or modifications. The next generation of cell migration models will most likely adopt modeling improvements across multiple avenues.

6.2.1   Viscoelastic Fluid Model

Within the interior of a cell exists the cytoplasm, a viscoelastic combination of a gel-like cytosol and actin filaments, among other compounds. Additionally, within bodily tissues, the extracellular fluid is composed of viscoelastic glycosaminoglycan chains with heterogeneous properties due to variability in synthesis. One of the more common GAGs is hyaluronan which has a highly dependent shear viscosity [109]. Additionally, hyaluronan is known to inhibit the diffusion of molecules, heal and protect from infection, and provide lubrication [110]. As a result, cell dynamics may be markedly different as compared to migration through Newtonian fluids. Furthermore, in cells motivated by chemotaxis or chemical signals, the interruption of molecular diffusion throughout the extracellular medium may also provide interesting behavior not otherwise seen in simulations. Zhu *et al* investigated puller- and pusher-type migration of a spherical swimmer using tangential surface deformations inside a viscoelastic fluid, and found differences in swimming speed and hydrodynamic efficiency compared to the Newtonian case [111]. Additionally, Li *et al* investigated flagellar swimming in viscoelastic medium using experimentally-derived

kinematics, also showing differences exist compared to the Newtonian case [112]. Simulation of highly deformable amoeboid cells through viscoelastic fluids may similarly produce interesting results.

6.2.2 Chemotaxis

One possible contribution is the implementation of a chemotactic model into the existing framework. Chemotaxis is the biased cell migration towards a particular source due to a chemical gradient [27]. When chemoattracts bind to complementary receptors on the plasma membrane, internal signaling mechanisms then amplify the chemical bias, causing pseudopods to form in the relative direction of the attractant [47]. Over time, and with sufficient generations of pseudopods, the cell will reach the source of the chemoattractant. Chemotaxis is a highly important strategy used by cells within the body, with some prime examples being immune cells dispatched to destroy foreign organisms [37], to embryonic cells depending on chemical signals for proper positioning and development [23].

Chemotactic models for amoeboid cell migration have been considered in various works [67], some of which are described here. Elliott *et al* [7] modeled two-dimensional amoeboid cell chemotaxis, where like our model, a noise bias was added to an activator-inhibitor system modeled by reaction-diffusion equations. Activator growth is then amplified in the direction of the attractant source. Neilson *et al* [8] took a similar approach using an activator-inhibitor system, but instead based the bias response on the degree of chemotactic receptor occupancy, which modulated pseudopod generation rates. Hecht *et al* [9] utilized a compass model which biased membrane patches, and subsequently, membrane extensions in the direction of an external source. Finally, Moure and Gomez

[10-11] created a three-dimensional amoeboid cell whose membrane receptors react with diffusive ligands present in the extracellular medium. Based on the distribution of bonded ligands, a bias direction is chosen, which is then used to modify the probability functions controlling activator peak and duration to produce chemotactic motion.

The adoption of a chemotactic model should consider a chemical species, actively secreted by tissue or cells within the domain, which can freely diffuse through the extracellular fluid. A model cell should have receptor distributions on its membrane, which through bonding rates, would produce a bias in pseudopod extension direction. Chemotactic migration would present as an interesting problem in the extracellular geometries we have considered, possibly affecting migration speed, persistence, and even the degree to which confinement traps a cell.

6.2.3   Peristaltic Migration

A recent study by Franz *et al* [12] described an interesting mode of swimming behavior termed peristaltic migration. Fat body cells of the pupal Drosophila fly, a non-human equivalent of adipocytes, were shown to migrate towards wounds purely through actomyosin driven contractile waves. This was accomplished without any adhesion mechanism present. These waves begin as a band in the cortex near the cell center, and migrate towards the rear, effectively propelling the cell forward. Waves were constantly generated under normal circumstances, but only became highly focused once the organism became wounded. Except for a contractile band model, the existing cell framework should be suitable without any modification. One possible avenue to model the contractile band is through pattern generation via Turing instabilities. The same reaction-diffusion equations we have used to generate dynamic circular patterns can be run with alternate parameters to

produce a variety of patterns. The large number of parameters, however, would require an exhaustive study to find the proper pattern. Spherical harmonic equations, which were used in [108] to model both protrusive and contractile forces, offer a periodic means to model a moving contractile band. Active stresses, which are discussed below are also another option to simulate this peristaltic behavior. A secondary but related project which might assist in the development of a contractile band model is the process of cytokinesis, or cell division. When mitosis is nearly completed, a thin ring of actin and myosin appears below the plasma membrane at the cell center. Continuous contraction of the ring results in the total separation of the cell [45].

6.2.4   Membrane Contractility

Similar to the previous section on peristaltic migration, and consistent with the standard model of cell migration is the ability of a cell to contract its membrane when needed. Myosin II present in the cell posterior pulls actin filaments towards one another, thereby creating a tensile force which advances the rear of the cell forward. While not exclusively required for cell migration in three-dimensional environments [58,63], cells with contractile capability assist in forcing motility through matrices which would otherwise preclude penetration [72-74]. Therefore, while not a shortcoming of any kind, it would be a sensible strategy to include a contractility mechanism in future works.

The computational modeling literature is split between works which do not model cell contractility [31,34,35], and those which consider contractility in some form or variation [9-11,13,29-30,32-33,61,64-65]. Sakamoto *et al* [30] conceived of myosin as being either free in suspension or bound to actin, thereby providing stiffness to the actin network through a shear modulus proportional to bound myosin. Among the three-dimensional

models is the work by Moure and Gomez [10-11], who made myosin a diffusible species within the cell and dependent on actin filament location. Activator-inhibitor systems may be useful to model high concentration regions of myosin, which could then be coupled to the governing equations of the cell by a contractile force. Active stresses could serve as another means to simulate contractility through fluid interactions. Finally, internal myosin dynamics, which are discussed below, can serve to generate more physiologically realistic models.

6.2.5   Blebbing Cell Model

As discussed above, cellular locomotion can be achieved purely through a contractile mechanism alone. Blebbing occurs when myosin induced contractions create a rupture between the actin cortex and the plasma membrane, generating an influx of cytosol driven by hydrostatic pressure and creating a bubble-like bleb which fills with fluid [26]. The cortex is then reconstructed directly under the membrane of the new bleb, which in time will retract. This process occurs repeatedly over time as different areas between the cortex and plasma membrane rupture, thus allowing the cell to migrate. Several works have attempted to model blebbing, including Lim *et al* [13], who considered a two-dimensional elastic actin cortex surrounded by an elastic cell membrane adhered together with Hookean springs. Membrane-cortex rupture preceded bleb growth, after which the cortex connections were reconstituted, and cortical tension caused bleb retraction.

The creation of a three-dimensional blebbing amoeboid cell model would be a great advancement in terms of current literature works. In our computational framework, both the cell plasma membrane and cortex can be modeled as nested vesicles, though a contractility mechanism would need to be implemented as discussed. Adhesion dynamics

between the membrane and cortex would also need to be considered, as ruptures are the flash point for bleb generation. Stochastic methods or perhaps activator-inhibitor systems may be helpful to control these adhesive fluctuations. Cytosolic fluid needs to flow from the inside of the cell to the gap between the membrane and cortex, so the inner vesicle must be either be permeable to fluid or modeled as an open surface where individual elements can be removed during bleb growth, and later added as the cell "repairs" its cortex. Additionally, the cell cortex could be modeled as an aggregate of individual actin filaments, though the complexity of achieving this is a work in itself.

6.2.6   Improved Adhesion Model

In our current adhesion model, only ten percent of cell nodes are available for adhesion bonding with the extracellular matrix geometries. The number of available bonds is further reduced by the Monte Carlo stochastic methods used to determine if bonds will form, and of course by distance considerations. This was done in part to mimic the amoeboid description of adhesion, which is described as having a diffuse integrin distribution on the cell membrane [28]. The probability of bond formation is set to be constant with the assumption of a suitable nearness between the cell and substrate, while the probability of bond deletion depends on a decaying exponential function of bond length. The latter statement agrees well with experiments, since higher forces due to stretching results in bonds rupturing.

Many works modeling cell migration have completely ignored adhesion [7,13,64-65], only considered ad hoc approximations proportional to cell speed [9-10,29-30,34] or the number of receptors present [30-31], among other methods [35,61]. Cirit *et al* [14] treated nascent and stable adhesions as ordinary differential equations. Similar to our work, Moure

and Gomez [11] and others [32-33] treated adhesion as combinations of drag and spring forces from discrete adhesion sites. Additionally, the maximum number of adhesions was capped, with new adhesions preferring sites with high actin concentration. Finally, adhesion maturation was included by linearly increasing the magnitude of the spring constant with time. Maturation reflects focal complex development, where integrins cluster in specific areas on the cell and connect to the cytoskeleton for stronger force transmission, and is therefore not needed for amoeboid modeling. Drag is fully resolved in our model, meaning improvements should be looked at in the discrete adhesion model itself. At this point in time, however, improvements to computational modeling may need to wait for experimental results to illuminate the integrin force-deformation relationship as well as the total number and distributions of integrins on amoeboid cells.

6.2.7   Mesenchymal Migration

While a more detailed study of amoeboid migration is certainly valid, there is also the possibility to model mesenchymal cell migration within the existing computational framework. Multiple cell types achieve locomotion using this method, from fibroblasts [59] to cancer cells [1]. In particular, cancer cells require a mesenchymal-like behavior when penetrating through basement membrane and other dense tissues, where migration could not otherwise occur under an amoeboid morphology [40]. Mesenchymal migration is characterized by a spindle-like shape coupled with highly adhesive clustered regions on the cell. Additionally, the cell is path-generating, or capable of degrading extracellular matrix components using proteolytic enzymes [28].

In order to model this form of locomotion, several modifications would be necessary. Focal adhesions can be modeled by associating integrin clusters with patterns generated

through activator-inhibitor systems. Cell membrane parameters will most likely need to be rescaled from the amoeboid mode, as mesenchymal cells are not as deformable and must withstand higher forces due to adhesive connections to the cytoskeleton. Finally, a proteolytic model must be implemented into the computational framework. Proteases concentrate near cell-ECM connections and cleave macromolecules such as collagen and fibronectin, allowing the cell to penetrate the matrix [28]. Proteolytic enzyme concentration can similarly be coupled to an activator-inhibitor system, possibly the same system controlling focal adhesions but with a delayed effect. Lastly, the extracellular matrix model would need to be altered to consider matrix degradation. A filament-based model could essentially 'erase' certain areas, thereby simulating decay, although additional programming would be necessary.

6.2.8 Phagocytosis

When pathogens or foreign material enter the body through a wound, white blood cells are dispatched to neutralize any threat they may pose. This is primarily accomplished through phagocytosis, or the engulfment of a particle by the cell membrane. Receptor-ligand interactions between the cell and bacterium causes the generation of a pseudopod, which envelops the bacterium and fuses to form a vesicle. The vesicle is then internalized and combined with lysosomes which digest its contents [45]. In our computational model, when amoeboid cells interacted with spherical obstacles, there appeared to be a natural tendency for the cell to impose itself onto the obstacle. This was caused by the activator-inhibitor system producing pseudopods in the deformed concave region between the cell and the convex obstacle, thus preventing the cell from migrating elsewhere. It is possible that this behavior could be exploited to model an amoeboid cell internalizing a deformable

particle. Herant *et al* [15] simulated phagocytosis of a rigid particle in two dimensions, suggesting myosin contractility may be necessary to anchor the cell membrane to the obstacle. A three-dimensional phagocytosis model would prove an interesting work if pursued. Both chemotactic and contractile mechanisms (per Herant) would need to be added. Most importantly, however, the cell membrane would need to be modified so it can separate and recombine elements due to vesicle generation. Development of a cytokinesis model would aid in programing efforts. Depending on the model complexity, internalized vesicles could also fuse with lysosomes, and later become part of the plasma membrane. Studies on the effect of deformability and adhesive strength on phagocytosis would prove interesting.

6.2.9   Extravasation

Because our group models problems both in amoeboid cell migration and blood flow within the microvasculature, it is well-posed to combine the models and simulate the extravasation of a neutrophil from a blood vessel into the connective tissue. When foreign bacteria enter the body, endotoxins are released which cause vascular endothelial cells near the infection to express adhesion molecules which help immune cells within the circulation attach to and migrate out of the vessel [56].

Leukocyte rolling adhesion along the epithelium has previously been modeled in our group by Pappu and Bagchi [16] among others [5,66]. The blood vessel model would require additional modules, however, since it can no longer be considered as a zero-thickness surface. In addition to the endothelium, vessel walls are also composed of a pericyte sheath and basement membrane, beyond which is the connective tissue of the extracellular matrix [69]. Experiments have shown that neutrophil engagement with

pericytes causes cytoskeletal relaxation which opens gaps along the sheath and allows the cell to exit the blood vessel [68]. This geometry could be modeled as fixed deformable vesicles immersed inside dense extracellular matrix tissue. Further complexities can be added by introducing pathogens which trigger the extravasation cascade by emitting specific chemical signatures.

6.2.10 Active Stresses

One alternative to pseudopod generation driven by an activator-inhibitor system is a concept known as active stress. Introduced by Kruse *et al* [17], active stresses result in the flow of cytoplasmic gels within a cell. Protrusive active stresses in the gel result in expansion, effectively mimicking protrusion due to actin polymerization, while contractile active stress mimic actomyosin contraction [18]. Active stresses are therefore a means to generate motility independent of the physical mechanisms which may have caused it. Pseudopods or membrane extensions could be generated by introducing protrusive stresses near the membrane. Similarly, cell retraction could be accomplished using contractile stresses which pull the membrane forward.

6.2.11 Migration with Interstitial Flow

This dissertation has demonstrated the modeling of amoeboid swimming and locomotion through various extracellular mediums. In each case, however, the cell was immersed in a quiescent flow with no fluid disturbance except that which was self-generated. Yet within the human body, cells often encounter an interstitial flow generated from fluid exchange between the blood vessels and lymph nodes [60]. Flow speeds of 0.1 through 1 micrometers per second are not uncommon, with those rates increasing in tissues

where inflammation is present [19]. Non-zero fluid velocities within the extracellular matrix may have a substantial effect on chemical signaling phenomenon and subsequent reactions from chemotactic cells. Additionally, when coupled with a deformable extracellular matrix geometry, adhesion dynamics are posed to be affected. Integrin tethering forces are inclined to vary based on imposed drag forces from the interstitial flow on the cell and corresponding tissue. Finally, as observed in this work, matrix geometry will most likely affect interstitial flow patterns, and therefore cell dynamics. Our computational model is fully capable of generating such flow conditions, and a study of how amoeboid cell dynamics vary when subjected to interstitial flow in various matrix geometries and under varying cell parameters is warranted.

6.2.12 Internal Actin-Myosin Dynamics

As described in the introduction, actin and myosin are proteins situated inside the cell. Pseudopod membrane extension is achieved through polymerization of actin filaments, which crosslink underneath the plasma membrane. Myosin interacts with actin filaments to generate contractility in the membrane. In our computational model, the actomyosin complex is modeled using a coarse-grain method on the cell membrane itself, where Turing instabilities are associated with concentrations of actin, and capping and severing proteins. No explicit contractile mechanism is modeled or included. Moure and Gomez [10-11] devised a model for an amoeboid cell which explicitly models the dynamics of myosin, F-actin, and G-actin within the cell. The total amount of actin is conserved, while myosin will advect towards regions of low actin density, consistent with experimental observations [27]. Phase transitions between G-actin and F-actin are also considered. Any future amoeboid cell model should consider having actomyosin dynamics modeled inside the cell.

Various forms of transport equations are one possible method to model actomyosin dynamics within the cell as described. Volumetric reaction-diffusion equations are another possibility.

6.2.13 Artificial Cell Modeling

While numerous models for biological cell migration exist within the literature, there is another field emerging which involves artificially constructed cells. And while many aspects of living cells such as structure and biochemical pathways are fairly well understood, a great deal of information still remains elusive to researchers [70]. Attempts to bridge this knowledge gap are being made by the construction of synthetic cells, or minimalistic models designed for specific purposes. The reasoning for this is that a cell can never be fully understood until science can build one from scratch, so a barebones model is a step towards full understanding. One such example is an artificially constructed amoeba consisting of a simple membrane vesicle containing nanoparticles which stimulate the growth of actin filaments, thereby providing propulsion [71]. Because the design of a synthetic cell is rather simplistic, simulation can be used to both support experiments and predict results which have not yet been observed.

6.2.14 Realistic Extracellular Matrix Geometries

Lastly, we propose the expansion of our computational model for extracellular matrix geometries on two fronts. The first recommendation is to simulate more realistic geometries. In this work, arrays of rigid and unmoving spheres and cylinders have been used to study amoeboid cell migration. Cylindrical arrays bear similarity to aligned tissues within the body, while three-dimensional lattice is often used in tissue-engineering studies.

Yet cells often encounter networks of crosslinked fibers with sizes ranging on the order of nanometer to micrometer thickness and with varying degrees of randomness. Cylinders remain a good approximation to collagen filaments within the body, but their dimensional nature limits the tissues where it can be modeled. CAD software may be utilized to model filaments using lofts or sweeps, allowing filaments to bend or turn as they do naturally *in vivo*. The combination of dozens, or even hundreds of filaments such as these would greatly improve the modeling capacity of extracellular matrix geometries.

The second recommendation, which should be considered along with the first, is to institute deformation models for the extracellular matrix geometries. Connective tissue is inherently deformable, and because cell behavior has been linked to matrix stiffness [36,39,61-62], this challenge must be addressed. Furthermore, tissue properties are known to vary across the body. Connective tissue, for instance, is porous and soft, while the properties of bone are considerably different [40]. We propose a new model which uses the finite element method to track the elastic deformations of each collagen filament as the cell exerts a traction force upon it. Each collagen filament can be composed of any standard generic solid finite element, such as the hexahedral variant, and mapped to its specific location inside the computational domain. Filaments can then be linked together assuming the presence of fibronectin linkers, thereby addressing further biological questions. After resolving traction and drag forces upon each filament, the standard finite element method can be solved for their respective deformations.

Alternatively, realistic deformable matrices can be implemented into the existing model by other means. Future work within our group, which will most likely be performed concurrently with future amoeboid works, involves the modeling of blood vessels capable

of deformation. This idea can be adapted and repurposed to construct deformable filaments, which can be placed throughout the computational domain to serve as an extracellular matrix equivalent. Along the same line of thought, because the current model can simulate more than one cell in a fluid domain, the extra cells themselves can be reshaped into deformable obstacles.

Many works in the literature either model geometry as rigid [7,29,13,33], or in some cases as deformable but greatly oversimplified [30,34]. Moure and Gomez [10-11] modeled periodic arrays of thin, fixed and non-deforming cylindrical elements. To our knowledge, no models which consider both realistic and deformable extracellular matrix geometries exist. Therefore, future models would benefit greatly from extracellular matrix geometry which is both physiologically realistic and deformable in nature

References

[1] K. Wolf, I. Mazo, H. Leung, K. Engelke, U. H. von Andrian, E. I. Deryugina, A. Y. Strongin, E. B. Bröcker, and P. Friedl. Compensation mechanism in tumor cell migration: mesenchymal-amoeboid transition after blocking of pericellular proteolysis. *Journal of Cell Biology*, **160**:2, 2003.

[2] N. P. Barry and M. S. Bretscher. Dictyostelium amoebae and neutrophils can swim. *Proceedings of the National Academy of Sciences U.S.A.*, **107**:25, 2010.

[3] A. J. Bae and E. Bodenschatz. On the swimming of Dictyostelium amoebae. *Proceedings of the National Academy of Sciences U.S.A.*, **107**:44, 2010.

[4] G. I. Bell, M. Dembo, and P. Bongrand. Competition between nonspecific repulsion and specific bonding. *Biophysical Journal*, **45**:6, 1984.

[5] D. A. Hammer and S. M. Apte. Simulation of cell rolling and adhesion on surfaces in shear flow: general results and analysis of selectin-mediated neutrophil adhesion. *Biophysical Journal*, **63**:1, 1992.

[6] E. M. Purcell. Life at low Reynolds number. *American Journal of Physics*, **45**:1, 1977.

[7] C. M. Elliott, B. Stinner, and C. Venkataraman. Modelling cell motility and chemotaxis with evolving surface finite elements. *Journal of the Royal Society Interface*, **9**:76, 2012.

[8] M. Neilson, J. A. Mackenzie, S. D. Webb, and R. H. Insall. Modelling cell movement and chemotaxis using pseudopod-based feedback. *Siam Journal on Scientific Computing*, **33**:3, 2011.

[9] I. Hecht, M. K. Skoge, P. G. Charest, E. Ben-Jacob, R. A. Firtel, W. F. Loomis, H. Levine, and W. J. Rappel. Activated membrane patches guide chemotactic cell motility. *PLoS Computational Biology*, **7**:6, 2011.

[10] A. Moure and H. Gomez. Phase-field model of cellular migration: Three-dimensional simulations in fibrous networks. *Computer Methods in Applied Mechanics and Engineering*, **320**, 2017.

[11] A. Moure and H. Gomez. Three-dimensional simulation of obstacle-mediated chemotaxis. *Biomechanics and Modeling in Mechanobiology*, **17**:5, 2018.

[12] A. Franz, W. Wood, and P. Martin. Fat body cells are motile and actively migrate to wounds to drive repair and prevent infection. *Developmental Cell*, **44**:4, 2018.

[13] F. Y. Lim, Y. L. Koon, and K. H. Chiam. A computational model of amoeboid cell migration. *Computer Methods in Biomechanics and Biomedical Engineering*. **16**:10, 2013.

[14] M. Cirit, M. Krajcovic, C. K. Choi, E. S. Welf, A. F. Horwitz, and J. M. Haugh. Stochastic model of integrin-mediated signaling and adhesion dynamics at the leading edges of migrating cells. *PLoS Computational Biology*. **6**:2, 2010.

[15] M. Herant, V. Heinrich, and M. Dembo. Mechanics of neutrophil phagocytosis: experiments and quantitative models. *Journal of Cell Science*, **119**:9, 2006.

[16] V. Pappu and P. Bagchi. 3D computational modeling and simulation of leukocyte rolling adhesion and deformation. *Computers in Biology and Medicine*, **38**:6, 2008.

[17] K. Kruse, J. F. Joanny, F. Jülicher, J. Prost, K. Sekimoto. Asters, Vortices, and Rotating Spirals in Active Gels of Polar Filaments. *Physical Review Letters*, **92**:7, 2004.

[18] A. E. Carlsson. Mechanisms of cell propulsion by active stresses. *New Journal of Physics*, **13**, 2011.

[19] J. A. Pedersen, S. Lichter, and M. A. Swartz. Cells in 3D matrices under interstitial flow: Effects of extracellular matrix alignment on cell shear stress and drag forces. *Journal of Biomechanics*, **43**:5, 2010.

[20] S. Morley, M. H. Hager, S. G. Pollan, B. Knudsen, D. Di Vizio, and M. R. Freeman. Trading in your spindles for blebs: the amoeboid tumor cell phenotype in prostate cancer. *Asian Journal of Andrology*, **16**:4, 2014.

[21] A. Wells, J. Grahovac, S. Wheeler, B. Ma, and D. Lauffenburger. Targeting tumor cell motility as a strategy against invasion and metastasis. *Trends in Pharmacological Sciences*, **34**:5, 2013.

[22] A. Gaylo, D. C. Schrock, N. R. J. Fernandes, and D. J. Fowell. T cell interstitial migration: Motility cues from the inflamed tissue for micro- and macro-positioning. *Frontiers in Immunology*, **7**, 2016.

[23] E. Raz and H. Mahabaleshwar. Chemokine signaling in embryonic cell migration: a fisheye view. *Development*, **136**:8, 2009.

[24]   M. Scianna. An extended cellular potts model analyzing a wound healing assay. *Computers in Biology and Medicine*, **62**, 2015.

[25]   G. S. Klindt and B. M. Friedrich. Flagellar swimmers oscillate between pusher- and puller-type swimming. *Physical Review E*, **92**, 2015.

[26]   P. T. Caswell and T. Zech. Actin-based cell protrusion in a 3D matrix. *Trends in Cell Biology*, **28**:10, 2018.

[27]   H. Levine and W. J. Rappel. The physics of eukaryotic chemotaxis. *Physics Today*, **66**:2, 2013.

[28]   P. Friedl and K. Wolf. Tumor-cell invasion and migration: diversity and escape mechanisms. *Nature Reviews Cancer*, **3**:5, 2003.

[29]   I. Hecht, H. Levine, W. J. Rappel, and E. Ben-Jacob. "Self-Assisted" Amoeboid Navigation in Complex Environments. *PLoS ONE*, **6**:8, 2011.

[30]   Y. Sakamoto, S. Prudhomme, and M. H. Zaman. Modeling of adhesion, protrusion, and contraction coordination for cell migration simulations. *Journal of Mathematical Biology*, **68**:1, 2014.

[31]   M. H. Zaman, R. D. Kamm, P. Matsudaira, and D. A. Lauffenburger. Computational Model for Cell Migration in Three-Dimensional Matrices. *Biophysical Journal*, **89**:2, 2005.

[32]   D. Shao, H. Levine, and W. J. Rappel. Coupling actin flow, adhesion, and morphology in a computational cell motility model. *Proceedings of the National Academy of Sciences U.S.A.*, **109**:18, 2012.

[33]   C. A. Copos, S. Walcott, J. C. del Álamo, E. Bastounis, A. Mogilner, and R. D. Guy. Mechanosensitive Adhesion Explains Stepping Motility in Amoeboid Cells. *Biophysical Journal*, **112**:12, 2017.

[34]   D. K. Schlüter, I. Ramis-Conde, and M. A. J. Chaplain. Computational Modeling of Single-Cell Migration: The Leading Role of Extracellular Matrix Fibers. *Biophysical Journal*, **103**:6, 2012.

[35]   M. Herant and M. Dembo. Form and Function in Cell Motility: From Fibroblasts to Keratocytes. *Biophysical Journal*, **98**:8, 2010.

[36]   G. Charras and E. Sahai. Physical influences of the extracellular environment on cell migration. *Nature Reviews Molecular Cell Biology*, **15**, 2014.

[37] M. Sarris, J. B. Masson, D. Maurin, L. M. Van der Aa, P. Boudinot, H. Lortat-Jacob, and P. Herbomel. Inflammatory Chemokines Direct and Restrict Leukocyte Migration within Live Tissues as Glycan-Bound Gradient. *Current Biology*, **22**:24, 2012.

[38] E. Bianconi, A. Piovesan, F. Facchin, A. Beraudi, R. Casadei, F. Frabetti, L. Vitale, M. C. Pelleri, S. Tassani, F. Piva, S. Perez-Amodio, P. Strippoli, and S. Canaider. An estimation of the number of cells in the human body. *Annals of Human Biology*, **40**:6, 2013.

[39] M. M. Stevens and J. H. George. Exploring and Engineering the Cell Surface Interface. *Science*, **310**:5751, 2005.

[40] K. Wolf and P. Friedl. Extracellular matrix determinants of proteolytic and non-proteolytic cell migration. *Trends in Cell Biology*, **21**:12, 2011.

[41] K. Valachová, N. Volpi, R. Stern, and L. Šoltés. Hyaluronan in Medical Practice. *Current Medicinal Chemistry*, **23**:31, 2016.

[42] E. A. Balazs. Viscoelastic Properties of Hyaluronic Acid and Biological Lubrication. *University of Michigan Medical Center Journal*, 1968.

[43] V. Hascall and J. D. *Esko. Essentials of Glycobiology: Chapter 15 Hyaluronan*. Cold Spring Harbor Laboratory Press, 2009.

[44] J. Monslow, P. Govindaraju, and E. Puré. Hyaluronan – a functional and structural sweet spot in the tissue microenvironment. *Frontiers in Immunology*, **6**, 2015.

[45] G. M. Cooper. *The Cell: A Molecular Approach*. Sinauer Associates, 2000.

[46] D. Jiang, J. Liang, and P. W. Noble. Hyaluronan in Tissue Injury and Repair. *Annual Review of Cell and Developmental Biology*, **23**, 2007.

[47] T. D. Pollard, W. C. Earnshaw, J. Lippincott-Schwartz, and G. Johnson. *Cell Biology*. Elsevier, 2017.

[48] N. N. Schommer, J. Muto, V. Nizet, and R. L. Gallo. Hyaluronan Breakdown Contributes to Immune Defense against Group A Streptococcus. *The Journal of Biological Chemistry*, **289**:39, 2014.

[49] A. D. Theocharis, S. S. Skandalis, C. Gialeli, and N. K. Karamanos. Extracellular matrix structure. *Advanced Drug Delivery Reviews*, **97**, 2016.

[50] T Lämmermann, B. L. Bader, S. J. Monkley, T. Worbs, R. Wedlich-Söldner, K. Hirsch, M. Keller, R. Förster, D. R. Critchley, R. Fässler, and M. Sixt. Rapid leukocyte migration by integrin-independent flowing and squeezing. *Nature*, **453**:7191, 2008.

[51] M. Sixt and T. Lämmermann. In Vitro Analysis of Chemotactic Leukocyte Migration in 3D Environments. *Methods in Molecular Biology*, **769**, 2011.

[52] J. T. H. Mandeville, M. A. Lawson, and F. R. Maxfield. Dynamic imaging of neutrophil migration in three-dimensions: mechanical interactions between cells and matrix. *Journal of Leukocyte Biology*, **61**:2, 1997.

[53] P. Friedl, S. Borgmann, and E. B. Bröcker. Amoeboid leukocyte crawling through extracellular matrix: lessons from the Dictyostelium paradigm of cell movement. *Journal of Leukocyte Biology*, **70**:4, 2001.

[54] T. D. Pollard and J. A. Cooper. Actin, a Central Player in Cell Shape and Movement. *Science*, **326**:5957, 2009.

[55] E. Sahai. Mechanisms of cancer cell invasion. *Current Opinion in Genetics & Development*, **15**:1, 2005.

[56] J. D. Pardee. *The Actin Cytoskeleton in Cell Motility, Cancer, and Infection*. Morgan and Claypool Publishers, 2009.

[57] C. D. Paul, P. Mistriotis, and K. Konstantopoulos. Cancer cell motility: lessons from migration in confined spaces. *Nature Reviews Cancer*, **17**:2, 2017.

[58] Y. J. Liu, M. Le Berre, F. Lautenschlaeger, P. Maiuri, A. Callan-Jones, M. Heuzé, T. Takaki, R. Voituriez, and M. Piel. Confinement and Low Adhesion Induce Fast Amoeboid Migration of Slow Mesenchymal Cells. *Cell*, **160**:4, 2015.

[59] R. J. Petrie and K. Yamada. Fibroblasts Lead the Way: A Unified View of 3D Cell Motility. *Trends in Cell Biology*, **25**:11, 2015.

[60] M. S. Pepper and M. Skobe. Lymphatic endothelium: morphological, molecular and functional properties. *The Journal of Cell Biology*, **163**:2, 2003.

[61] T. Lai and K. H. Chiam. Mechanochemical model of cell migration on substrates of varying stiffness. *Physical Review E*, **84**, 2011.

[62] M. H. Zaman, L. M. Trapani, A. L. Sieminski, D. MacKellar, H. Gong, R. D. Kamm, A. Wells, D. A. Lauffenburger, and P. Matsudaira. Migration of tumor cells in 3D matrices is governed by matrix stiffness along with cell-matrix adhesion and proteolysis. *Proceedings of the National Academy of Sciences U.S.A.*, **103**:29, 2006.

[63] T. Lämmermann and M. Sixt. Mechanical modes of 'amoeboid' cell migration. *Current Opinion in Cell Biology*, **21**:5, 2009.

[64] H. Wu, A. Farutin, W. F. Hu, M. Thiébaud, S. Rafaï, P. Peyla, M. C. Lai, and C. Misbah. Amoeboid swimming in a channel. *Soft Matter*, **12**:36, 2016.

[65] L. Yang, J. C. Effler, B. L. Kutscher, S. E. Sullivan, D. N. Robinson, and P. A. Iglesias. Modeling cellular deformations using the level set formalism. *BMC Systems Biology*, **2**:1, 2008.

[66] S. Jadhav, C. D. Eggleton, and K. Konstantopoulos. A 3-D Computational Model Predicts that Cell Deformation Affects Selectin-Mediated Leukocyte Rolling. *Biophysical Journal*, **88**:1, 2005.

[67] P. A. Iglesias and P. N. Devreotes. Navigating through models of chemotaxis. *Current Opinion in Cell Biology*, **20**:1, 2008.

[68] S. Wang, C. Cao, Z. Chen, V. Bankaitis, E. Tzima, N. Sheibani, and K. Burridge. Pericytes Regulate Vascular Basement Membrane Remodeling and Govern Neutrophil Extravasation during Inflammation. *PLoS ONE*, **7**:9, 2012.

[69] S. Nourshargh, P. L. Hordijk, and M. Sixt. Breaching multiple barriers: leukovyte motility through venular walls and the interstitium. *Nature Reviews Molecular Cell Biology*, **11**:5, 2010.

[70] B. C. Buddingh and J. C. M. van Hest. Artificial Cells: Synthetic Compartments with Life-like Functionality and Adaptivity. *Accounts of Chemical Research*, **50**:4, 2017.

[71] J. Yi, J. Schmidt, A. Chien, and C. D. Montemagno. Engineering an artificial amoeba propelled by nanoparticle-triggered actin polymerization. *Nanotechnology*, **20**:8, 2009.

[72] H.-R. Thiam, P. Vargas, N. Carpi, C. L. Crespo, M. Raab, E. Terriac, M. C. King, J. Jacobelli, A. S. Alberts, T. Stradal, A.-M. Lennon-Dumenil, and M. Piel. Perinuclear Arp2/3-driven actin polymerization enables nuclear deformation to facilitate cell migration through complex environments. *Nature Communications*, **7**, 2016.

[73] K. Wolf, M. te Lindert, M. Krause, S. Alexander, J. te Riet, A. L. Willis, R. M. Hoffman, C. G. Figdor, S. J. Weiss, and P. Friedl. Physical limits of cell migration: Control by ECM space and nuclear deformation and tuning by proteolysis and traction force. *Journal of Cell Biology*, **201**:7, 2013.

[74] R. Poincloux, O. Collin, F. Lizárraga, M. Romao, M. Debray, M. Piel, and P. Chavrier. Contractility of the cell rear drives invasion of breast tumor cells in 3D Matrigel. *Proceedings of the National Academy of Sciences U.S.A.*, **108**:5, 2011.

[75] B.-C. Chen, W. R. Legant, K. Wang, L. Shao, D. E. Milkie, M. W. Davidson *et al*. Lattice light-sheet microscopy: Imaging embryos to molecules at high spatial resolution. *Science*, **346**:6208, 2014.

[76] T. D. Pollard, L. Blanchoin, and R. D. Mullins. Molecular Mechanisms Controlling Actin Filament Dynamics in Nonmuscle Cells. *Annual Review of Biophysics and Biomolecular Structure*, **29**, 2000.

[77] C. Ploetz, E. I. Zcyband, and D. E. Birk. Collagen fibril assembly and deposition in the developing dermis: Segmental deposition in extracellular compartments. *Journal of Structural Biology*, **106**:1, 1991.

[78] A. M. Turing. The Chemical Basis of Morphogenesis. *Bulletin of Mathematical Biology*, **52**:1, 1990.

[79] J. D. Murray and M. R. Myerscough. Pigmentation Pattern Formation on Snakes. *Journal of Theoretical Biology*, **149**:3, 1991.

[80] J. D. Murray. A Pre-pattern Formation Mechanism for Animal Coat Markings. *Journal of Theoretical Biology*, **88**:1, 1981.

[81] I. Lengyel and I. R. Epstein. Modeling of Turing Structures in the Chlorite-Iodide-Malonic Acid-Starch Reaction System. *Science*, **251**:4994, 1991.

[82] P. Gray and S. K. Scott. Autocatalytic Reactions in the Isothermal, Continuous Stirred Tank Reactor. *Chemical Engineering Science*, **38**:1, 1983.

[83]   J. D. Murray and G. F. Oster. Generation of Biological Pattern and Form. *IMA Journal of Mathematics Applied in Medicine and Biology*, **1**:1, 1984.

[84]   H. Meinhardt. Orientation of chemotactic cells and growth cones: models and mechanisms. *Journal of Cell Science*, **112**:17, 1999.

[85]   G. Dziuk and C. M. Elliott. A Fully Discrete Evolving Surface Finite Element Method. *SIAM Journal of Numerical Analysis*, **50**:5, 2012.

[86]   R. Barreira, C. M. Elliott, and A. Madzvamuse. The surface finite element method for pattern formation on evolving biological surfaces. *Journal of Mathematical Biology*, **63**:6, 2011.

[87]   E. J. Fuselier and G. B. Wright. A High-Order Kernel Method for Diffusion and Reaction-Diffusion Equations on Surfaces. *Journal of Scientific Computing*, **56**:3, 2013.

[88]   A. Madzvamuse. Time-stepping schemes for moving grid finite elements applied to reaction-diffusion systems on fixed and growing domains. *Journal of Computational Physics*, **214**:1, 2006.

[89]   N. Tuncer, A. Madzvamuse, and A. J. Meir. Projected finite elements for reaction-diffusion systems on stationary closed surfaces. *Applied Numerical Mathematics*, **96**, 2015.

[90]   D. Boal. *Mechanics of the Cell*. Cambridge University Press, 2002.

[91]   J. Howard. *Mechanics of Motor Proteins and the Cytoskeleton*. Sinauer Associates, 2001.

[92]   R. Skalak, A. Tozeren, R. P. Zarda, and S. Chien. Strain energy function of red blood cell membranes. *Biophysical Journal*, **13**:3, 1973.

[93]   O.-Y. Zhong-can and W. Helfrich. Bending energy of vesicle membranes: General expressions for the first, second, and third variation of the shape energy and applications to spheres and cylinders. *Physical Review A*, **39**:10, 1989.

[94]   B. Rozycki and R. Lipowsky. Spontaneous curvature of bilayer membranes from molecular simulations: Asymmetric lipid densities and asymmetric adsorption. *Journal of Chemical Physics*, **142**:5, 2015.

[95]   A. Yazdani and P. Bagchi. Influence of membrane viscosity on capsule dynamics in shear flow. *Journal of Fluid Mechanics*, **718**, 2013.

[96] A. Yazdani and P. Bagchi. Three-dimensional numerical simulation of vesicle dynamics using a front-tracking method. *Physical Review E, Statistical, Nonlinear, and Soft Matter Physics*, **85**:5, 2012.

[97] D. Cordasco, A. Yazdani, and P. Bagchi. Comparison of erythrocyte dynamics in shear flow under different stress-free configurations. *Physics of Fluids*, **26**, 2014.

[98] D. Traynor and R. R. Kay. Possible roles of the endocytic cycle in cell motility. *Journal of Cell Science*, **120**:14, 2007.

[99] T. W. Michaels, N. R. Larrimer, E. N. Metz, and S. P. Balcerzak. Surface Morphology of human leukocytes. *Blood*, **37**:1, 1971.

[100] S. Petitjean. A survey of methods for recovering quadrics in triangle meshes. *ACM Computing Surveys*, **34**:2, 2002.

[101] M. Reuter, S. Biasotti, D. Giorgi, G. Patane, and M. Spagnuolo. Discrete Laplace–Beltrami operators for shape analysis and segmentation. *Computers & Graphics*, **33**:3, 2009.

[102] G. Xu. Convergence of discrete Laplace–Beltrami operators over surfaces. *Computers and Mathematics with Applications*, **48**:3, 2004.

[103] E. J. Campbell and P. Bagchi. A computational model of amoeboid cell motility in the presence of obstacles. *Soft Matter*, **14**:28, 2018.

[104] M. Dembo, D. C. Torney, K. Saxman, and D. Hammer. The reaction-limited kinetics of membrane-to-surface adhesion and detachment. *Proceedings of the Royal Society of London*, **234**:1274, 1988.

[105] C. S. Peskin. Immersed Boundary Method. *Acta Numerica*, **11**, 2002.

[106] S. O. Unverdi and G. Tryggvason. A front-tracking method for viscous, incompressible, multi-fluid flows. *Journal of Computational Physics*, **100**:25, 1992.

[107] P. Balogh and P. Bagchi. A computational approach to modeling cellular-scale blood flow in complex geometry. *Journal of Computational Physics*, **334**, 2017.

[108] A. Farutin, S. Rafaï, D. K. Dysthe, A. Duperray, P. Peyla, and C. Misbah. Amoeboid Swimming: A Generic Self-Propulsion of Cells in Fluids by Means of Membrane Deformations. *Physical Review Letters*, **111**:22, 2013.

[109] T. Laurent, U. B. Laurent, and J. R. E. Fraser. The structure and function of hyaluronan: An overview. *Immunology and Cell Biology*, **74**:2, 1996.

[110] K. Valachová, N. Volpi, R. Stern, and L. Šoltés. Hyaluronan in Medical Practice. *Current Medicinal Chemistry*, **23**:31, 2016.

[111] L. Zhu, E. Lauga, and L. Brandt. Self-propulsion in viscoelastic fluids: Pushers vs. pullers. *Physics of Fluids*, **24**:5, 2012.

[112] C. Li, B. Qin, A. Gopinath, P. E. Arratia, B. Thomases, and R. D. Guy. Flagellar swimming in viscoelastic fluids: role of fluid elastic stress revealed by simulations based on experimental data. *Journal of the Royal Society, Interface*, **14**:135, 2017.

[113] P. J. M. Van Haastert. Amoeboid cells use protrusions for walking, gliding, and swimming. *PLoS One*, **6**:11, 2011.

[114] W. Xu, R. Mezencev, B. Kim, L. Wang, J. McDonald, and T. Sulchek. Cell stiffness is a biomarker of the metastatic potential of ovarian cancer cells. *PLos One*, **7**:10, 2012.

[115] S. E. Cross, Y. Jin, J. Rao, and J. K. Gimzewski. Nanomechanical analysis of cells from cancer patients. *Nature Nanotechnology*, **2**:12, 2007.

[116] A. Fritsch, M. Hockel, T. Kiessling, K. D. Nnetu, F. Wetzel, M. Zink, and J. A. Kas. Are biomechanical changes necessary for tumour progression. *Nature Physics*, **6**:10, 2010.

[117] N. S. Gov and A. Gopinathan. Dynamics of membranes driven by actin polymerization. *Biophysical Journal*, **90**:2, 2006.

[118] M. P. Sheetz and J. Dai. Modulation of membrane dynamics and cell motility by membrane tension. *Trends in Cell Biology*, **6**:3, 1996.

[119] R. Niwayama, K. Shinohara, and A. Kimura. Hydrodynamic property of the cytoplasm is sufficient to mediate cytoplasmic streaming in the caenorhabiditis elegans embryo. *Proceedings of the National Academy of Sciences U.S.A.*, **108**:29, 2011.

[120] K. Keren, P. T. Yam, A. Kinkhabwala, A. Mogilnet, and J. Theriot. Intracellular fluid flow in rapidly moving cells. *Nature Cell Biology*, **11**:10, 2009.

[121] A. Mogilner and D. Odde. Modeling cellular processes in 3D. *Trends in Cell Biology*, **21**:12, 2011.

[122] M. Bindschadler, E. A. Osborn, C. F. Dewey Jr., and J. L. McGrath. A mechanistic model of the actin cycle. *Biophysical Journal*, **86**:5, 2004.

[123] J. A. Ditlev, N. M. Vacanti, I. L. Novak, L. M. Loew, and D. Richard. An open model of actin dendritic nucleation. *Biophysical Journal*, **96**:9, 2009.

[124] J. Young and S. Mitran. A numerical model of cellular blebbing: A volume conserving, fluid-structure interaction model of the entire cell. *Journal of Biomechanics*, **43**:2, 2010.

[125] Y. Xiong, C. Huang, P. A. Iglesias, and P. N. Devreotes. Cells navigate with a local-excitation, global-inhibition-biased excitable network. *Proceedings of the National Academy of Sciences U.S.A.*, **107**:40, 2010.

[126] H. Levine, D. A. Kessler, W. Rappel, and D. R. Nelson. Directional sensing in eukaryotic chemotaxis: A balanced inactivation model. *Proceedings of the National Academy of Sciences U.S.A.*, **103**:26, 2006.

[127] B. Rubinstein, K. Jacobson, and A. Mogilner. Multiscale two-dimensional modeling of a motile simple-shaped cell. *Multiscale Modeling & Simulation*, **3**:2, 2005.

[128] D. Y. Shao, W. J. Rappel, and H. Levine. Computational model for cell morphodynamics. *Physical Review Letters*, **105**:10, 2010.

[129] D. Kabaso, R. Shlomovitz, K. Schloen, T. Stradal, and N. S. Gov. Theoretical model for cellular shapes driven by protrusive and adhesive forces. *PLoS Computational Biology*, **7**:5, 2011.

[130] B. Vanderlei, J. J. Feng, and L. Edelstein-Keshet. A computational model of cell polarization and motility coupling mechanics and biochemistry. *Multiscale Modeling & Simulation*, **9**:4, 2011.

[131] D. C. Bottino and L. J. Fauci. A computational model of amoeboid deformation and locomotion. *European Biophysical Journal*, **27**:5, 1998.

[132] H. Wu, M. Thiebaud, W.-F. Hu, A. Farutin, S. Rafai, M.-C. Lai, P. Peyla, and C. Misbah. Amoeboid motion in confined geometry. *Physical Review E*, **92**, 2015.

[133] S. Najem and M. Grant. Phase-field approach to chemotactic driving of neutrophil morphodynamics. *Physical Review E*, **88**:3, 2013.

[134] L. Li, S. F. Norrelykke, and E. C. Cox. Persistent cell motion in the absence of external signals: A search strategy for eukaryotic cells. *PLoS One*, **3**:5, 2008.

[135] L. Bosgraaf and P. J. M. Van Haastert. The ordered extension of pseudopodia by amoeboid cells in the absence of external cues. *PLoS One*, **4**:4, 2009.

[136] G. K. Batchelor. The stress system in a suspension of force-free particles. *Journal of Fluid Mechanics*, **41**:3, 1970.

[137] E. Lauga and S. Michelin. Stresslets induced by active swimmers. *Physical Review Letters*, **117**, 2016.

[138] W. A. Muller. Mechanisms of transendothelial migration of leukocytes. *Circulation Research*, **105**:3, 2009.

[139] D. Bray. *Cell movements: from molecules to motility*. New York, 2000.

[140] H. Yamaguchi, J. Wyckoff, and J. Condeelis. Cell migration in tumors. *Current Opinion in Cell Biology*. **17**:5, 2005.

[141] K. Wolf, S. Alexander, V. Schacht, L. M. Coussens, U. H. von Andrian, J. van Rheenen, E. Deryugina, and P. Friedl. Collagen-based cell migration models *in vitro* and *in vivo*. *Seminars in Cell and Developmental Biology*. **20**:8, 2009.

[142] R. J. Huber and D. H. O'Day. Extracellular matrix dynamics and functions in the social amoeba Dictyostelium: A critical review. *Biochimica et Biophysica Acta*, **1861**:1, 2017.

[143] J. Guck, F. Lautenschläger, S. Paschke, and M. Beil. Critical review: cellular mechanobiology and amoeboid migration. *Integrative Biology*, **2**:11-12, 2010.

[144] E. K. Paluch, I. M. Aspalter, and M. Sixt. Focal adhesion-independent migration. *Annual Review of Cell Developmental Biology*, **32**, 2016.

[145] M. Sarris and M. Sixt. Navigating in tissue mazes: chemoattractant interpretation in complex environments. *Current Opinion in Cell Biology*, **36**, 2015.

[146] V. Ambravaneswaranm I. Y. Wong, A. J. Aranyosi, M. Toner, and D. Irimia. Directional decisions during neutrophil chemotaxis inside bifurcating channels. *Integrative Biology*, **2**:11-12, 2010.

[147] J. B. Wyckoff, J. G. Jones, J. S. Condeelis, and J. E. Segall. A critical step in metastasis: *in vivo* analysis of intravasation at the primary tumor. *Cancer Research*, **60**:9, 2000.

[148] E. J. Campbell and P. Bagchi. A computational model of amoeboid cell swimming. *Physics of Fluids*, **29**:101902, 2017.

[149] K. M. Hakkinen, J. S. Harunaga, A. D. Doyle, and K. M. Yamada. Direct Comparisons of the Morphology, Migration, Cell Adhesions, and Actin Cytoskeleton of Fibroblasts in Four Different Three-Dimensional Extracellular Matrices. *Tissue Engineering: Part A*, **17**:5-6, 2011.

[150] R. O. Hynes. Integrins: Versatility, modulation, and signaling in cell adhesion. *Cell*, **69**:1, 1992.

[151] J. Brábek, C. T. Mierke, D. Rösel, P. Veselý, and B. Fabry. The role of the tissue microenvironment in the regulation of cancer cell motility and invasion. *Cell Communication and Signaling: CCS*, **8**, 2010.

[152] J. Zhu and A. Mogilner. Comparison of cell migration mechanical strategies in three-dimensional matrices: a computational study. *Interface Focus*, **6**:5, 2016.

[153] N. Ogawa. Curvature-dependent diffusion flow on a surface with thickness. *Physical Review E*, **81**, 2010.

[154] J. Faraudo. Diffusion equation of curved surfaces: Theory and application to biological membranes. *Journal of Chemical Physics*, **116**:13, 2002.

[155] S. M. Giannitelli, D. Accoto, M. Trombetta, and A. Ranier. Current trends in the design of scaffolds for computer-aided tissue engineering. *Acta Biomaterialia*, **10**:2, 2014.

[156] S. Kim, F. Qui, S. Kim, A. Ghanbari, C. Moon, L. Zhang, B. J. Nelson, and H. Choi. Fabrication and characterization of magnetic microrobots for three-dimensional cell culture and targeted transportation. *Advanced Materials*, **25**:41, 2013.

[157] M. K. Driscoll, C. McCann, R. Kopace, R. Homan, J. T. Fourkas, C. Parent, and W. Losert. Cell shape dynamics: From waves to migration. *PLoS Computational Biology*, **8**:3, 2012.

[158] Y. T. Maeda, J. Inose, M. Y. Matsuo, S. Iwaya, and M. Sano. Ordered patterns of cell shape and orientational correlation during spontaneous cell migration. *PLoS One*, **3**:11, 2008.

[159] D. R. Soll, E. Voss, B. Varnum-Finney, and D. Wessels. Dynamic morphology system: A method for quantifying changes in shape, pseudopod formation, and motion in normal and mutant amoeboid of Dictyostelium discoideum. *Journal of Cell Biochemistry*, **37**:2, 1988.

[160] E. Bastounis, R. Meili, B. Alvarez-Gonzalez, J. Francois, J. C. Del Alamo, R. A. Firtel, and J. C. Lasheras. Both contractile axial and lateral traction force dynamics drive amoeboid cell motility. *Journal of Cell Biology*, **204**:6, 2014.

[161] D. R. Critchley. Focal adhesions – the cytoskeletal connection. *Current Opinion in Cell Biology*, **12**:1, 2000.

[162] B. Álvarez-González, R. Meili, E. Bastounis, R. A. Firtel, J. C. Lasheras, and J. C. del Álamo. Three-dimensional balance of cortical tension and axial contractility enables fast amoeboid migration. *Biophysical Journal*, **108**:2, 2015.

[163] S. J. Henry, J. C. Crocker, and D. A. Hammer. Ligand density elicits a phenotypic switch in human neutrophils. *Integrative Biology*, **6**:3, 2014.

[164] J. Niewöhner, I. Weber, M. Maniak, A. Müller-Taubenberger, and G. Gerisch. Talin-null cells of Dictyostelium are strongly defective in adhesion to particle and substrate surfaces and slightly impaired in cytokinesis. *Journal of Cell Biology*, **138**:2, 1997.

[165] J. Jacobelli, R. S. Friedman, M. A. Conti, A. M. Lennon-Dumenil, M. Piel, C. M. Sorensen, R. S. Adelstein, and M. F. Krummel. Confinement-optimized three-dimensional T cell amoeboid motility is modulated via myosin IIA-regulated adhesions. *Nature Immunology*, **11**:10, 2010.